2-1-2018

Efficient light trapping via nanostructures integration in thin film organic and inorganic solar cells

Sara Magdi Al-Menabawy

The American University in Cairo

School of Science and Engineering

Efficient light trapping via nanostructures integration in thin film organic and inorganic solar cells

A Thesis Submitted to

The Department of Nanotechnology

In Partial Fulfillment of the Requirements for

The Degree of Master of Science

By

Sara Magdi Ibrahim Al-Menabawy

September 2017

The American University in Cairo

School of Science and Engineering

Efficient light trapping via nanostructures integration in thin film organic and inorganic solar cells

By

Sara Magdi Al-Menabawy

Submitted to

The Department of Nanotechnology

In Partial Fulfillment of the requirements for

The Degree of Master of Science

Dr. Mohamed Swillam (Advisor) Associate Professor, Physics Department, AUC	Date
Dr. Amr Shaarawi (Internal examiner) Professor, Physics Department, AUC	Date
Dr. Khaled Kirah (External Examiner) Professor, Engineering Physics and Mathematics department, Ain Shams University	Date
Dr. Mohamed Al-Fiky (Moderator) Assisstant Professor, Physics Department, AUC	Date

Contents

List of Figures

Acknowledgments

First and foremost, I would like to thank my thesis advisor Dr. Mohamed Swillam. Dr. Swillam provided unconditional technical and moral support throughout my master's duration. He always encourages me, steers me in the right direction and extracts the best out of me. I always felt lucky and proud to be in his team.

I would also like to express the deepest appreciation to Dr. Joumana El-Rifai for her valuable feedback on a large portion of the work in this thesis. Our collaboration with her was a great addition to this thesis and I have learnt a lot from her. I also want to extend my gratefulness to Dr. Nageh Allam who taught me a lot during the courses I have taken with him.

A special gratitude goes to each and every one in the nanophotonics research laboratory (NRL) team for their unfailing assistance and encouragement. I would also like to thank the Youssef Jameel science and technology research center team (Eng. Ahmed Nour, Eng. Ahmed Beltagy and Saleh) for training me on the devices I needed and their continuous devotion in solving any problem I face. Another gratitude goes to the academy of scientific research and technology (ASRT) for providing the funding of the work.

I also would like to acknowledge my committee members, Dr. Amr Shaarawi and Dr. Khaled Kirah for spending the time reading the thesis. I am thankful to their valuable comments on this thesis. I would like to thank Dr. Mohamed Elfiky for serving as the moderator of my thesis examination committee.

I am grateful to my parents, Dr. Laila and Dr. Magdi, who have provided the best moral and emotional support throughout my life. I am also grateful to my sisters, Nihal and Mariam, who always encouraged me and supported me along the way. This accomplishment would not have been possible without them.

With a special mention to, Mohamed Youssef, my husband. In addition to his continuous moral support, he was my mentor in all the experimental work. He taught me every detail about the clean room, CVD, and SEM. Without his continuous guidance, I would have spent much longer time finishing my experimental work.

Thank you all for your great help!

Sara Magdi

Abstract

Solar cells provide a valuable mean to convert sunlight photons into useful electrical energy. Silicon is the most widely used material in solar cell's industry. Bulk crystalline silicon solar cells, the first solar cell generation, are currently the most widely spread type of solar cell. Although this type of solar cell provides high efficiencies, it requires high cost due to high material usage in addition to high cost of the complex fabrication techniques used.

Motivated by the urgent need to develop affordable solar cells in order to be able to compete with current conventional energy sources, thin film solar cells are gaining a huge interest. Thin film solar cells are not only interesting due to the less material usage and thus the lower cost, but also because it enables the use of low-cost materials with less quality such as amorphous silicon and conductive polymers. Amorphous silicon and conductive polymers are two examples of semiconductor materials that have good optical absorption properties and could be fabricated with low cost and simple fabrication techniques. However, they suffer from poor electronic properties due the randomness of their structure causing electrons to have low diffusion length and thus, recombine fast. Light trapping techniques are the most effective way to increase the optical absorption without increasing the physical thickness of the absorbing layer. Hence, it enables the use of materials with lower quality and bulk crystalline silicon with maintaining comparable efficiencies.

The use of plasmonics for light trapping in organic solar cells has been widely investigated and novel designs are still developing. However, all organic plasmonic solar cells reported are developed using metals. Here, we suggest, for the first time, the use of refractory plasmonics such as titanium nitride and zirconium nitride instead of metals in organic solar cells. Refractory plasmonics provide indispensable advantages such as their lower cost, C-MOS compatibility, higher thermal stability and wider resonance response. Several structures are numerically studied and compared. A thorough study for the scattering and absorption of these refractory plasmonics in a polymer environment is implemented.

Amorphous silicon is another material that suffer from low absorption. Its high refractive index causes a huge amount of light to be reflected from its surface. In addition, its small thickness causes further photons to be transmitted without getting absorbed. Thus, the developing of several 2D and 3D surface texturing is widely investigated in literature, Here, we develop a novel fabrication technique to fabricated nanocones and nanowires from an amorphous silicon thin film with one step techniques using excimer laser. The technique suggested here is fast, simple and easily scalable. In addition, we numerically developed a double light trapping scheme for amorphous silicon solar cells that not only decrease the reflection due to addition of surface texturing, but also decrease the light transmitted due to addition of metal gratings at the back electrode. This design provides an efficient light trapping scheme that sandwiches the a-Si layer between

two light trapping configurations resulting in huge enhancement in absorption.

Another factor increasing the cost of commercially available silicon solar cells is the complex fabrication of a p-n junction. Thus hybrid solar cells that combine silicon with a polymer provide an efficient mean to easily fabricate solar cell devices. Nanostructuring the inorganic material in hybrid solar cells plays an important role in increasing the efficiency of such devices because it provides a larger interfacial area between the organic and inorganic material resulting in the dissociation pf a larger number of excitons. Here, we propose a structure based on silicon tapered nanowires coated with a low bandgap polymer. The use of tapered silicon nanowires is chosen because of the high capabilities of this structure to trap and absorb light efficiently. In addition, the choice of the low band gap polymer is thoroughly studied and several polymers are compared. The choice of the polymer was made with the aim to increase the absorption range of both materials to absorb the largest number of incident photons. This structure provides an almost unity absorption throughout the whole visible and near infra-red range with only 5 μm length tapered silicon nanowires coated with 50 nm of the low band gap polymer, this design significantly reduce the amount of materials used to achieve this high absorption.

All these designs are thoroughly analyzed in this thesis along with recommended fabrication techniques for numerically proposed structures. All simulations developed in this thesis were implemented using a 3D finite difference time domain (FDTD) tool (i.e. Lumerical).

Chapter 1 : Introduction

1.1.Different solar cell's designs overview

The continuous growth in the world's production and sales is concurrent with a continuous growth in the world's energy demand. Oil, coal, natural gas and nuclear energy are currently the most widely used sources of energy. These non-renewable energy sources are subject to many drawbacks. For example, burning fossil fuels causes severe environmental problems. In addition, they are limited and their availability is sometimes subject to political conflicts. Thus, exploring new energy sources is a persistent task for governments, researchers and even some individuals.

Renewable energy is currently the most promising approach for meeting the world's increasing energy demand. It could be used as an assistant to conventional, limited resources such as fossil fuels. Solar energy, as an example of renewable energy, is believed to be able to overcome this challenge by converting the unlimited sunlight energy to useful electrical energy (i.e. photons to electrons conversion)[1]. With 10,000 more energy than the world consumption is coming from sunlight (i.e. $3x10^{24}$ J/year), the energy produced from solar power can easily satisfy the whole world energy needs. Besides, it does not consume any fuel, does not cause any pollution, and has high-power to weight generation.

The core of the photovoltaic system is the solar cell. Here we focus on developing new concepts that could upgrade the performance of this device. Solar cells' idea was driven by the photovoltaic effect discovered by the French physicist A.E. Becquerel in 1839 where electric current in a material is created upon exposure to light[2]. Then, this effect was explained by Albert Einstein in 1905 with the photoelectric effect theory. Since then, a great interest is directed to the design and fabrication of solar cells. Many solar cells configurations are designed afterwards, starting from the first silicon p-n junction solar cell developed at Bell laboratory with 6% efficiency[3], passing by the highly efficient silicon solar cells with 25% efficiency[4], and ending by using novel materials for solar cells such as perovskites[5,6].

Three generations of solar cells are developed during the last decades. These generations are summarized in Figure 1. The First generation contains the conventional bulk crystalline silicon solar cells. This type of solar cells requires high cost pure crystalline silicon and is fabricated with large

manufacturing costs. However, it is still the dominant type in the photovoltaic market. Motivated by the need to obtain low cost solar cells, thin film elemental (e.g. silicon) and compound (e.g. GaAs, and CIGS) solar cells are developed. This generation allows the use to other types of solar cells that does not require high purity in fabrication such as amorphous silicon. After the discovery of conductive polymers by Hideki Shirakawa, Alan Macdiarmid and Alan Heeger[7], a third generation solar cells based on organic materials is developed. This generation includes polymer based solar cells, dye-sensitized solar cells, and perovskites. The third generation of solar cells also contains new concepts targeting the enhancement of efficiencies beyond the Shockley-Queisser limit. These new concepts include the addition of nanostructures inside the solar cell or nanostructuring the absorbing layer itself. The development of these new concepts is the main focus of this thesis.

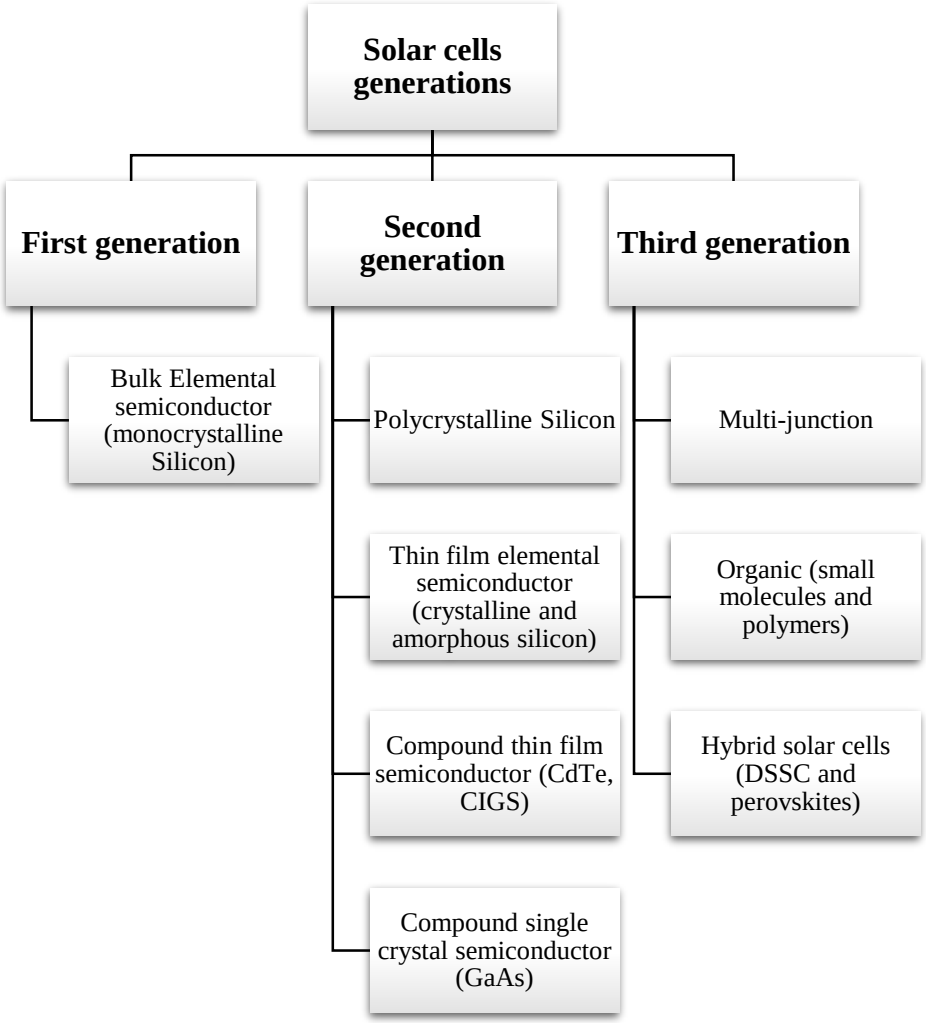

Figure 1: Solar cells' generations.

Although solar cells seem to be the most promising alternative to current limited energy sources, solar energy still faces some challenges that prevent it from being widely used. The main challenge is the relatively higher cost of solar cells compared to conventional energy sources. There is a great deal of research currently going on in different aspects in order to overcome this challenge. Materials research and cell design are the two main fields where researchers are working.

1.2.Fundamentals of solar cells

A solar cell is basically a p-n junction device. A p-n junction is a junction between a p-doped material (with excess holes) and an n-doped material (with excess electrons). The detailed process that takes place in a solar cell device is summarized in Figure 3. First of all, photons with energy larger than the bandgap of the used semiconductor are absorbed inside the material. Photons with energy smaller than the bandgap are transmitted and photons with energy much larger than the bandgap are excited above the conudction band and lost in thermalization. Thermalization is the loss of energy in the form of phonons vibrations or heat when the electron relaxes from higher energies to the conduction band edge. In addition, the absorption coefficient, which determines how far light should penetrate into a material before being absorbed, differ from a material to another. It mainly depends on the wavelength of the incident light and the extinction coefficient of the material as given by its equation:

$$\alpha = \frac{4\pi k}{\lambda}$$

where k is the extinction coefficient (i.e. the imaginary part of the refractive index). Figure 2 shows the absorption coefficient for some semiconductors. According to its band gap, each material cannot absorb light with wavelengths larger than a specific wavelength corresponding to its band gap ($E_{gap} = hc/\lambda$).

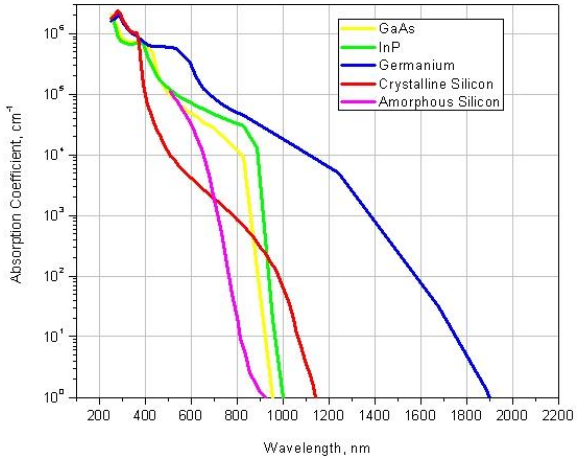

Figure 2: Absorption coefficient of some semiconductors (adopted from http://www.engineerdir.com/dictionary/catalog/5180/).

Absorbed photons then excite free electrons in the conduction level leaving free holes in the valence level (i.e. electron-hole pairs). The generation rate of electron-hole pairs in each point of the device depends on the absorption coefficient by the following equation:

$$G = \alpha N e^{-\alpha x}$$

Where N is the photon flux at the surface of the material and x is the distance into the material. Then, these excitons are separated by the built-in electric field at the p-n junction and diffused inside the material. They will then dissociate generating free carriers. These free carriers are then transported to their respective electrodes and collected at the solar cell terminals. Charge carriers have a chance to recombine before reaching the electrode. This is governed by their diffusion length (L) which depends on the quality of the material and is given by:

$$L = \sqrt{D\tau}$$

Where D is the diffusivity and τ is the charge carrier lifetime. Crystalline silicon, for example, has much larger diffusion length than amorphous silicon due to its well-defined crystal structure compared to the random crystal structure of amorphous materials. Each step in the process described in Figure 3 contribute to the overall efficiency of the solar cell. The lack to efficiently conduct any of these processes affects the overall performance of the solar cell and reduce its power conversion efficiency.

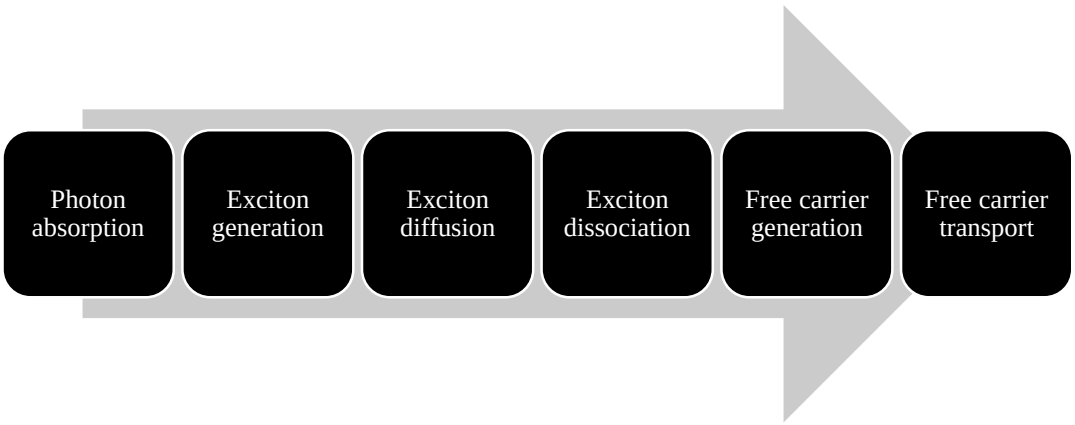

Figure 3: The detailed process that takes place in solar cell devices.

The electrical properties of the solar cell could be determined from its I-V curve. Short circuit current (J_{sc}), open circuit voltage (Voc), and the fill factor (FF) are the main parameters characterizing the solar cell and used to calculate its power conversion efficiency which is given by:

$$\eta = \frac{Isc\ Voc\ FF}{Pin}$$

Where Pin is the input power and is typically 100 mW/cm^2 for 1 sun concentration for AM1.5 irradiance. The short circuit current is the maximum current passing through the solar cell when the voltage across the solar cell is zero. The open circuit voltage is the maximum voltage across the solar cell when the current passing through it is zero. Since at the maximum current the voltage is zero, and vice versa, the power at these operating points is also zero. Thus, the maximum power is determined through the fill factor parameter which is defined as

$$FF = \frac{Imp\ Vmp}{Isc\ Voc}$$

Where Imp and Vmp are the current and voltage at the maximum point, respectively. These points are shown in a typical I-V curve in Figure 4.

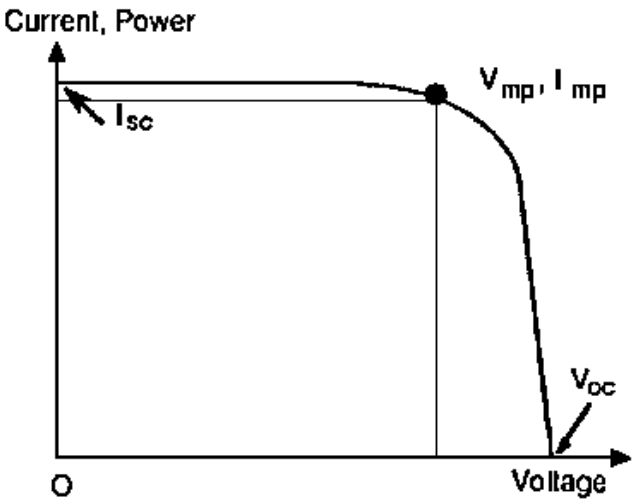

Figure 4: Typical solar cell I-V curve (adopted from https://www.re-innovation.co.uk/docs/pv-i-v-curve-tracer/).

The photon absorption efficiency is limited by the ability of the solar cell to absorb the incident photons. Only the absorbed photons will contribute in generating electron hole pairs. Some of these incident photons will be reflected due to mismatch in refractive index between air and the solar cell material (e.g. Silicon). Additionally, in case of thin films, some of the incident photons could be also transmitted after not being entirely absorbed due to the small thickness of the solar cell's active layer. This is due to the fact that absorbance is directly proportional to the path length as given by Beer's law:

$$A = \varepsilon bc$$

Where A is the absorbance, ε is the molar absorptivity (i.e. molar extinction coefficient), b is the path length inside the material and c is the concentration. These limitations will affect all the subsequent processes in the solar cell device and thus, severely affecting the overall efficiency of the solar cell. Thus, this thesis is primarily concerned with increasing the absorption efficiency of a solar cell.

Materials used in solar cells are mainly either organic or inorganic materials; in some cases, a combination of both is used. Figure 5 summarizes the efficiencies and trends of all types of solar cells. Inorganic solar cells are generally more stable and have relatively better performance than their organic counterparts. However, they require large absorbing layers to achieve decent absorption which make their fabrication complex and thus, increase their cost. In addition, the material's cost itself increases as the thickness increases. Moreover, a higher probability of carrier recombination is obtained in bulk

materials. Thus, thin film solar cells have attracted researchers. Their film thicknesses are in the range of 1 to 2 μm[1]. However, their low absorption makes their efficiency much lower than the bulk ones[1]. For small thicknesses, a low absorption in the NIR part of the spectrum is always observed[1]. For large thicknesses, the charge carriers recombine before hitting the surface of the junction where they should be collected leading to loosing these carriers' contribution to the output current.

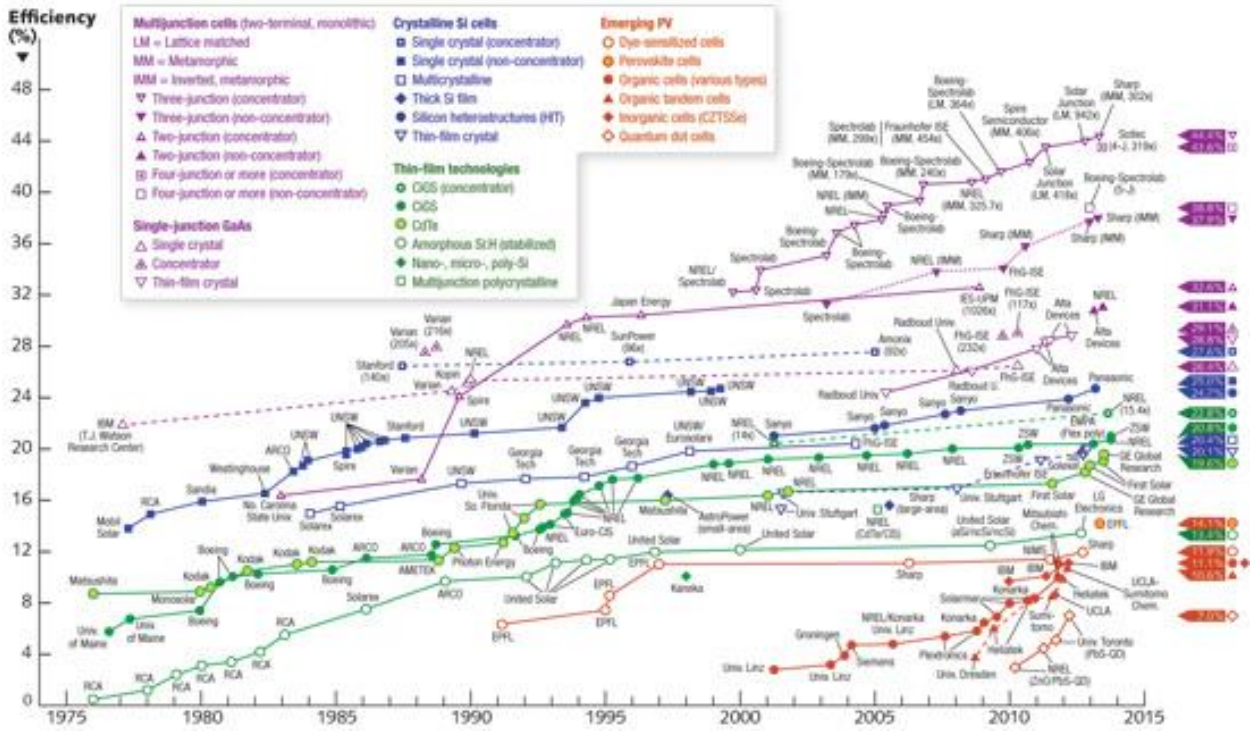

Figure 5: Efficiencies of vartious types of solar cells (adopted from http://www.laserfocusworld.com/articles/print/volume-49/issue-12/features/photonic-frontiers-photovoltaics-progress-in-the-quest-for-photovoltaic-power-generation.html).

1.3.Challenges in current commercial solar cells

The increasing energy demand challenge stated previously, and summarized in Figure 6, is believed to be solved with the help of renewable energy sources and more specifically photovoltaics. The primary solar cell type dominating the photovoltaic industry is the bulk crystalline silicon solar cell. Bulk crystalline silicon achieves the highest power conversion efficiency in silicon solar cells of 27.6%[8]. Crystalline silicon has many advantages such as the high diffusion length that amounts to few hundred micrometers which enables the fabrication of bulk materials ranging from 180-300 μm. This large thickness enables the absorption of most of the incoming photons. However, due to the large amount of

material used, the main cost of a solar cell comes from the pure silicon material. Additionally, the fabrication cost of a bulk crystalline silicon layer requires high cost and energy, in addition to the complex fabrication of a silicon p-n junction.

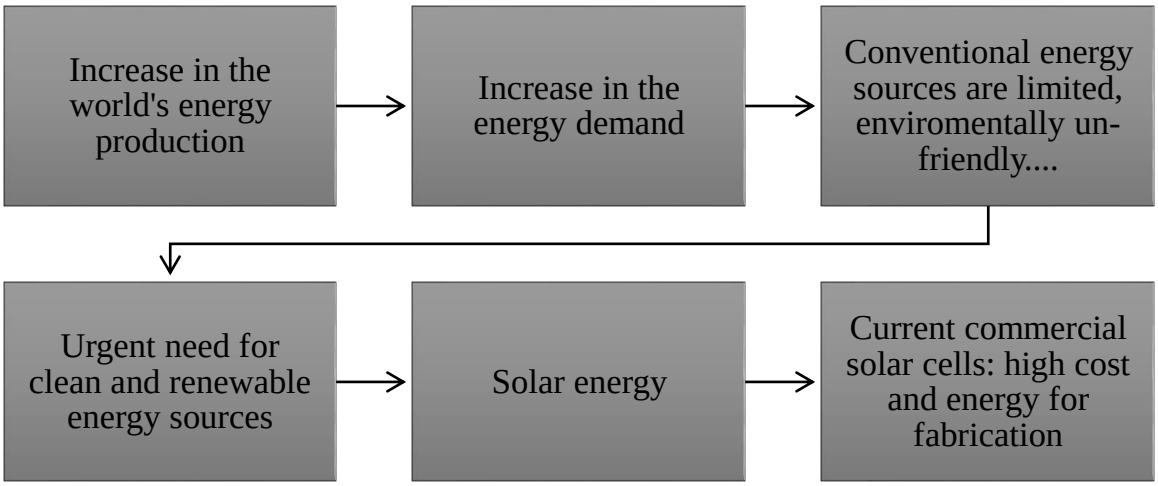

Figure 6: Problem Statement

1.4.Thin film solar cells

Driven by cost reduction and the need for easily fabricated and affordable solar cells that could compete with the current conventional energy sources, new materials are explored to achieve these goals. Thin film solar cells have attracted a great deal of interest due to the less material usage and the easier fabrication techniques. Moreover, it enables the usage of materials with lower diffusion length instead of the ultra-pure high-cost crystalline silicon. Organic solar cells and thin film amorphous silicon solar cells are the primary two examples for those emerging technologies. In addition, instead of the complex fabrication of silicon p-n junction, silicon/polymer hybrid solar cells are studied. In addition to the low cost of these materials, they could be fabricated at low temperature enabling the use of many types of substrates including flexible ones. Flexible solar cells open up the door for a new generation that could be integrated on flexible windows, portable power sources and others because of their light-weight and mechanical flexibility.

However, these advantages come on the expense of a small diffusion length due to the randomness of the crystal structure. Thus, their thicknesses are limited to few hundred nanometers to be able to collect the generated carriers before recombination. Since the absorption coefficient is directly proportional with the material thickness, un-efficient absorption is found for these structures. this un-efficient absorption result in low carrier generation and in turns low power conversion efficiency. This problem is summarized in Figure 7. For bulk solar cells, increasing the absorption is typically done through random texturing of the cell's surface. This roughness decreases the reflection and increases the light path length inside the cell[1,9]. However, this technique is not suitable for thin film solar cells because the rough area is generally larger than the film thickness leading to an increase in carrier recombination.

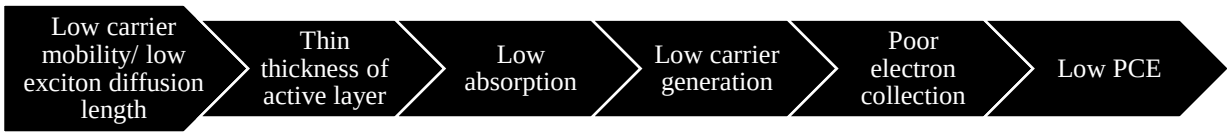

Figure 7: Reasons behind low power conversion efficiency of thin film solar cells

It could be seen that there is a trade-off here: a large thickness is needed for efficient absorption and a small thickness is required for efficient carrier collection. Here is where photon management play a significant role.

When nanostructures are properly engineered, they could trap the light inside the active layer increasing the light path length, and in turns increasing the absorption, without increasing the physical thickness of the device. Thus, absorption could be enhanced without sacrificing the electrical properties of the solar cell. Many light trapping strategies could be implemented using 2D and 3D photonic nanostructures to increase the absorption efficiency of thin films solar cells. In the next section, different light trapping strategies are discussed. The main focus of this work is to increase the optical path length of incident light inside the material without increasing the physical thickness.

1.5.Different light trapping strategies

Thin film solar cells are based on a thin active layer. Thus, they need light management techniques to be able to enhance the low absorption of this thin layer and increase the conversion efficiency of the

solar cell. Light trapping is the proper form of light management that could enhance the absorption by increasing the light path length inside the active layer. The main aim is to reduce the reflection at the surface of the active layer and increase light scattering inside it. Thus, photons could be trapped within the active layer and absorption could be enhanced which in turns will increase the overall power conversion efficiency of the solar cell. This trapping mechanism could be achieved by incorporating properly engineered photonic nanostructures. Large, broadband and wide angle absorption enhancement and reflection suppression in the visible range are the main goals for these nanostructures incorporation.

Several techniques could be used for light trapping inside the solar cells: incorporation of plasmonic nanostructures inside or outside the active layer, incorporation of nanocones (NCs), nanowires (NWs), tapered nanowires (TNWs), nanodoms, nanopyramids, or random surface texturing (i.e. random roughness). In the next sub-sections, the main three mechanisms which this thesis focuses on are discussed: plasmonic solar cells, surface texturing including nanocones, and different nanowires structures.

1.5.1. Plasmonic solar cells

When light interacts with a metal, the cloud of free electrons in the metal oscillates in its surface and cause field enhancement. the rising field of plasmonics seems promising for all optoelectronic devices as it has the ability to localize and guide light in the nanoscale; which was impossible with conventional photonic devices due to the diffraction limit of light. Thus, this field is attractive for photovoltaic designers due to its ability to increase the absorption of solar cells by localizing light in their active layers. Using plasmonic nanostructures, optical thickness can be increased without an actual increase in physical thickness of the active layer. Metallic nanostructures excite surface plasmon polaritons (SPP) at the metal/dielectric interface or localized surface plasmons (LSP) around the metal nanoparticles, which are basically the coupling of light electromagnetic waves with free electrons of the metal, and thus trap light around them. Consequently, the absorption of light enhances which boosts the current density without increasing the active layer thickness[9].

There are many ways to use plasmonic nanostructures in solar cells, the main ones are summarized

in Figure 8[1]. Metallic nanoparticles (NPs) with diameters in the subwavelength scale could be placed on the surface of the structure to scatter the freely propagating light waves into the active layer (Figure 8 (a)).Because the particles are placed at the interface between two media, light preferentially scatters in the medium with larger permittivity. Due to this scattering, light waves will hit the back electrode at a certain angle and if this angle exceeds the critical angle, the light will totally reflect internally and it will be trapped in the active layer leading to further increase in absorption. In Figure 8 (b), the near field of the NPs is coupled to the active layer increasing its effective absorption. In this case, the NPs could be placed inside the active layer, outside the active layer (i.e. inside a buffer layer), or at the interface between them. Another well-known technique is shown in Figure 8 (c) where the metallic electrode is nanostructured so that it can support SPP modes that couples to the absorbing layer.

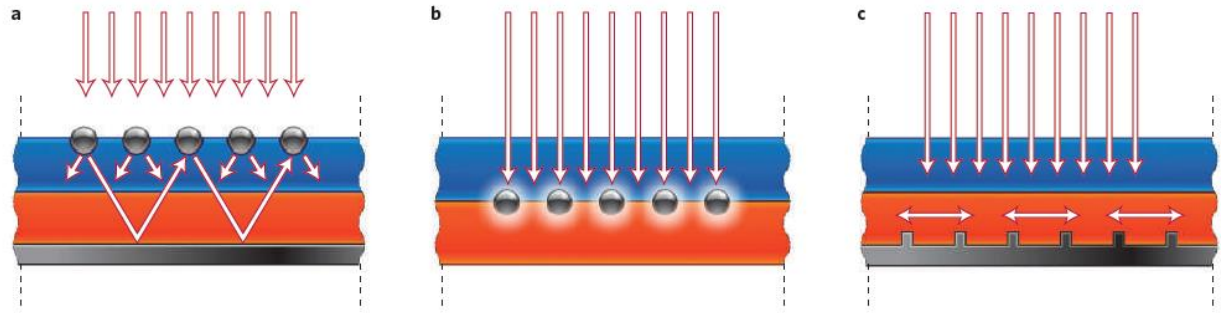

Figure 8 (a): Metallic NPs subwavelength structures placed to scatter light, (b) Near field of metallic NP couple to the active layer, (c) Nanostructured metal electrode excite SPP that couple to the active layer[1].

1.5.2. Surface texturing

For flat surface solar cells, a thick material is required to achieve decent absorption which will sacrifice the carrier collection efficiency due the small diffusion length of the material. Having a texture on the solar cell surface will reduce the reflection at a wide angle and increase the light scattering inside the under layer.

Various 3D structures are used for surface texturing of thin film amorphous silicon solar cells, such as nanodomes, nanopyramids, inverse nanopyramids, and nanocones. Nanocones (NCs) are found to be the most effective strategy for light trapping due the graded change in refractive between the air the active layer. Thus, extremely low reflections are measured for these structures at a wide angle of incidence.

1.5.3. Different nanowires structures

Thin films could be 1D, 2D or 3D nanostructured to be able to capture the same amount of light captured by flat bulk materials. In addition, these nanostructures offer shorter carrier diffusion length which results in more efficient carrier collection. Nanowires (NWs) are one of the widely investigated shapes in many fields including solar cells. Structuring the semiconductor material in a NW shape has many advantages. First, absorption will be enhanced due to the multiple light scattering between the array of nanowires [Figure 9(c)] which will result in better light trapping inside the material and better absorption. Second, reduced reflection will be achieved due to the graded change in refractive index between the air the active layer. Finally, the use of a radial p-n junction will result in decoupling the absorption direction and the charge collection direction as shown in Figure 9(a) . Thus, the length of the NW will act as the absorption direction and will depend on the desired optical path length. The radius of the NW will act as the charge collection direction and will depend on the diffusion length of the material. Therefore, this enables the use of cheap low cost material with small diffusion length.

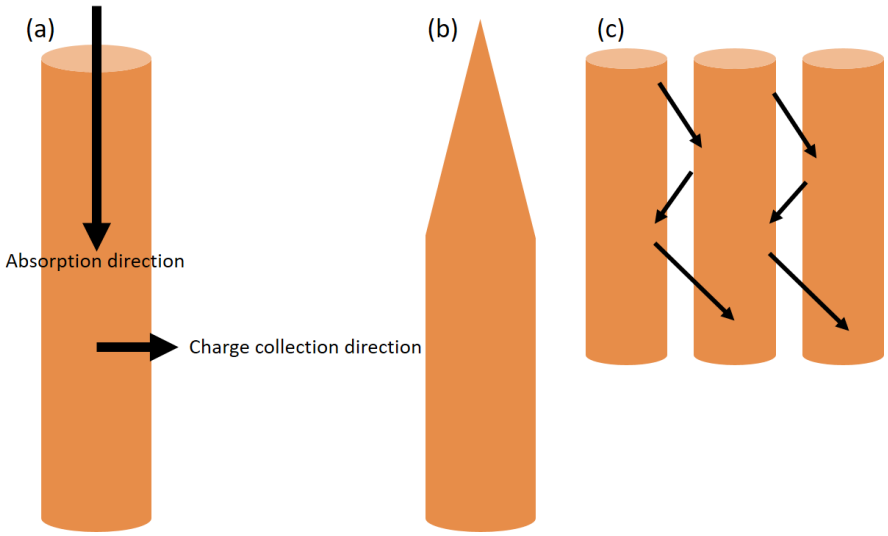

Figure 9: Schematic showing (a) nanowire's configuration, (b) tapered nanowire's configuration and (c) array of nanowires.

Nanowires could have several shapes. One of the most interesting ones are tapered nanowires shown in Figure 9(b). This structure has better refractive index matching resulting in further reduced reflection. In addition, the sharp tip of the wire is a hot spot that is very efficient in trapping the light.

1.6.Thesis scope and outline

Thin film amorphous silicon and organic solar cells are promising configurations for affordable energy alternative that could compete with the current conventional ones. Incorporating nanostructures with these thin films is a field that it extensively investigated to boost their conversion efficiencies and make them competitive with current commercial solar cells. The main focus of this thesis is to use low-cost material and fabrication techniques to boost the efficiency of these solar cells without increasing their cost. The thesis objective and scope are summarized in Figure 10.

Chapter 2 is a literature review that summarizes the previous work related to each topic discussed in the thesis. It contains three sections covering the literature of each following chapter in the thesis. The first section summarizes previous work on plasmonic organic solar cells, while the second section summarizes previous work on light trapping in amorphous silicon solar cells. The third section talks about hybrid/silicon polymer solar cells.

Chapter 3 presents the new designs proposed for organic plasmonic solar cells. Optical simulations showing the absorption enhancement obtained upon incorporation of refractory plasmonics in organic solar cells are presented.

Chapter 4 explains the new fabrication technique used to form silicon nanocones and nanowires from amorphous thin film layer. Enhanced absorption and reduced reflection at a wide angle is measured for these structures. In addition, optical simulation of a novel double light trapping structure for thin film amorphous silicon solar cells is presented.

Chapter 5 combines polymer based solar cells with silicon based solar cells in hybrid configuration. A thorough optical analysis of tapered nanowires solar cells is presented with and without polymer coating. Different polymers are added and comparisons between the performance of each in the solar cell device are explained.

Chapter 6 summarizes the conclusions of each chapter along with the future directions that will be taken for further analysis of the presented work.

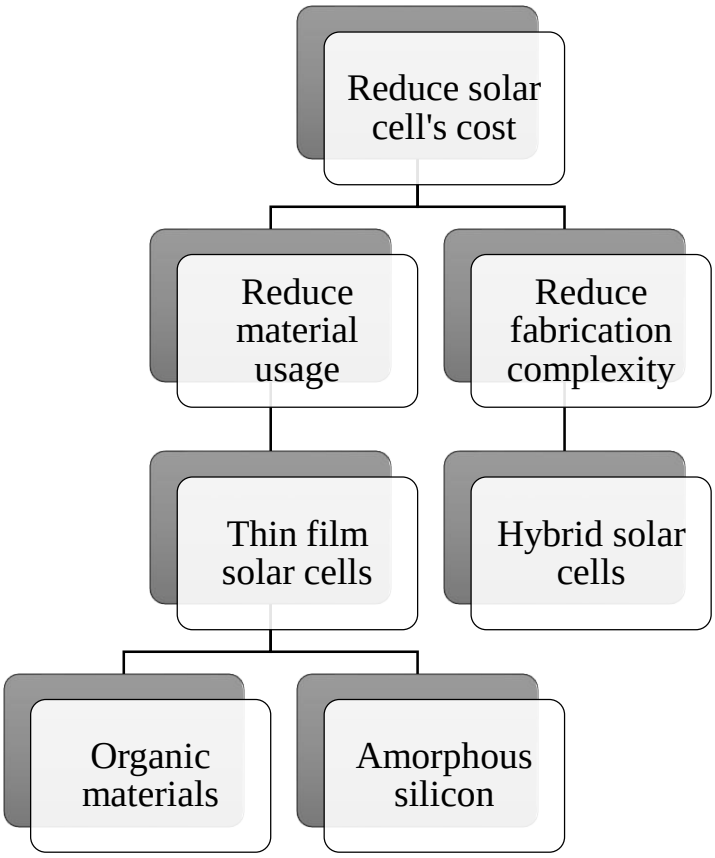

Figure 10: Thesis scope and objective

Chapter 2 : Literature review on light trapping in thin film solar cells

2.1.Light trapping in organic solar cells using plasmonic nanostructures

In the progress of achieving high efficiency thin film solar cells with low cost, organic solar cells (OSC) play an important role in attaining affordable solar cells while maintaining comparable efficiency to their inorganic counterparts[10–15]. After the discovery of conductive polymers by Hideki Shirakawa, Alan Macdiarmid, and Alan Heeger, this kind of materials became very interesting in many applications. A huge interest was devoted to solar cells based on conductive polymers. Organic solar cells have many advantages over their inorganic counterparts. They are fabricated from low cost materials and could be solution processed instead of the complex fabrication techniques of silicon solar cells. They are mainly painted on any substrate (e.g. rigid or flexible) making their fabrication lower in cost than many inorganic materials.

Although OSC are promising type of photovoltaic devices, they still have to overcome some challenges to be able to compete with the current commercial solar cells (e.g. silicon solar cells). The main two problems are their instability and low absorption. OSC are simply composed of a polymer as an active layer (i.e. absorbing layer), a front and back electrode, and typically a hole transport layer and an electron transport layer to match the materials' work functions. Due to the complex composition of polymers, they have a low exciton (i.e. electron-hole pairs that are still bounded) diffusion length and low charge carrier mobility[9,16–18.]This problem limits the active layer's thickness to be in the range of the nanometer scale (30-100 nm), which in turn limit the absorption of these layers[9]. Thus, the carrier generation becomes low and a small number of electrons are collected in comparison to the number of the incident photons which causes low power conversion efficiency (PCE) for such cells[9].

Absorption efficiency could be increased with different light trapping techniques such as surface texturing[19–21], photonic crystals[22], and plasmonic nanostructures[1,23–30]. Plasmonic solar cells are promising configurations that have the ability to overcome the thin film low absorption challenge by using metallic nanostructures. These nanostructures concentrate light inside the active layer resulting in

larger optical path length and, hence, larger absorption efficiency[31]. Most light trapping techniques reported for OSC are based on metal plasmonic nanostructures[32–34].

Random nanostructures such as nanoparticles, nanowires, nanomeshes, and nanodisks are incorporated in the OSC either inside or outside the active layer. Addition of nanostructures outside the active layer excites localized surface plasmons (LSP). These LSP depend mainly on the size and shape of the nanostructure. They scatter or concentrate light, according to their size, and trap it in the active layer. It has been also reported that addition of nanostructures inside OSC buffer layer decreases the series resistance of these layers which in turn leads to increased PCE[9].

It has been reported by Aneesh *et al.* that incorporation of Au NPs at the interface between a transparent conductive oxide (TCO) layer and a buffer layer, in a P3HT:PCBM based solar cell, has enhanced the short circuit current by 16% and PCE by 25%. The authors referred this enhancement to the coupling of the LSP of Au to the active layer resulting in enhanced absorption in active layer. This work was experimentally demonstrated and external quantum efficiency was measured confirming the enhancement in absorption observed by the PL spectroscopy[16]. In addition, the enhancement of short circuit current has been attributed to the decrease of series resistance of the TCO and buffer layer after introducing the Au NPs in them with almost no change in open circuit voltage.

The other common scheme is the addition of nanostructures inside the active layer. In this case, nanostructures either enhance the near field or act as scattering centers for light depending on their size[35]. Generally, small NPs are more likely to excite plasmonic modes around them resulting in near field enhancement, whereas larger particles (>100 nm) scatter light more efficiently. A mix of small and large nanostructures could also be used. In addition, incorporation of nanostructures inside active layers improves the morphology of the organic layers increasing its stability and leading to enhanced performance[9]. It was also reported that incorporation of Cu NPs inside the active layer shows an enhancement in the photocurrent even if no enhancement in absorption was found. This is believed to be due to the NPs ability to promote exciton dissociation leading to an increased number of charge carriers[36].

On the other hand, one dimensional 1D and two dimensional 2D periodic structures could be used

in metal electrodes to couple light to SPP modes leading to the confinement of light between the metal electrode and the active layer. The 2D metallic nanostructures have three important advantages that are very essential for high efficiency PV. First, they are polarization independent. The SPP are, in this case, in different directions, thus, they couple to TE and TM light waves efficiently enabling them to contribute in enhanced confinement. Second, they achieve broadband enhancement due to the exciting of the broad bandwidth short range SPP using ultrathin metal films. Third, many 2D periodic structures successfully achieved angle independent enhancement which is an important aspect for high efficiency PV[9].

One of the structures that incorporated 2D metal nanostructured back electrode in OSC is shown in Figure 11. The structure consists of a glass substrate deposited on it ITO as the transparent conductive electrode, then a buffer layer is placed (PEDOT:PSS) and on top of it the active layer is deposited. Finally, a Ag back electrode is placed with the nanoholes array structure, the diameter and the period of the holes are optimized using FDTD simulation tool (i.e. Lumerical)[37]. They reported an enhancement in the polymer's absorption due the excitation of short range SPP. Figure 12 (a) shows the absorption enhancement that happened due the addition of the nanoholes in the Ag back electrode. Figure 12 (b and c) clarifies that this absorption is due to the localization of the light around the holes.

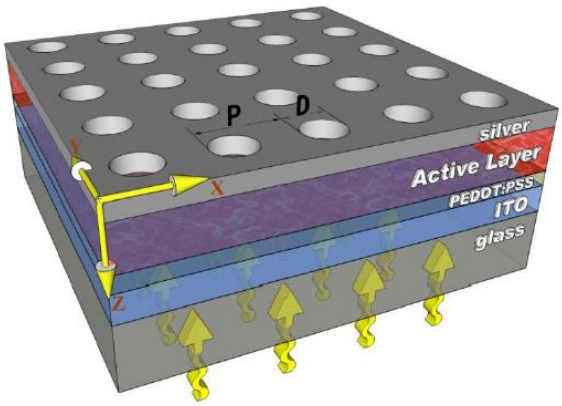

Figure 11: solar cell structure incorporating Ag nanopatterned back electrode[37]

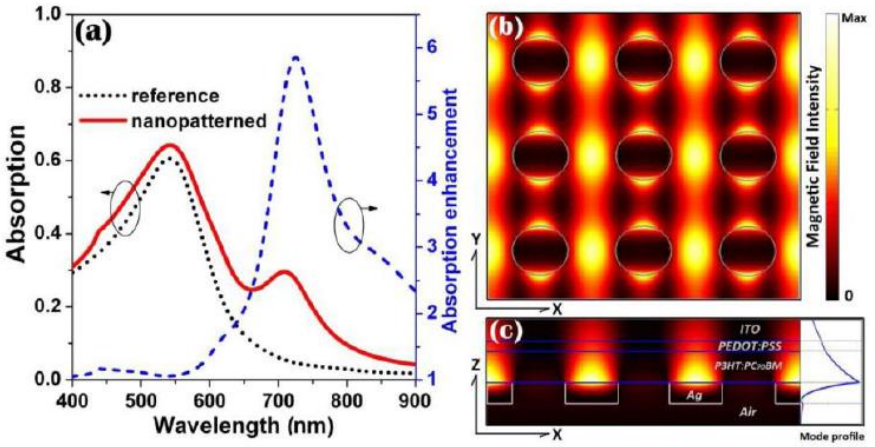

Figure 12: (a) absorption enhancement due the nano-patterning of the back electrode, (b) Magnetic field intensity inside the structure showing the localization of light around the holes[37].

This structure was further enhanced in another study by incorporating metal nanodisks inside the buffer layer to excite LSPR leading to significant confinement of light between these two plasmonic structures (i.e. inside the active layer). The modified structure is shown in Figure 13(a). Figure 13(b) clarifies the enhancement of absorption obtained using this structure. It can be seen that incorporating the nanodisks alone or the nanoholes alone leads to an enhancement. However, using both plasmonic structures increases the obtained improvement in the absorption and demonstrates significant enhancement over the reference cell. After the optimization of this structure, by changing the nanodisks and nanoholes diameter and period, an enhancement of 128% in the total photon absorption was obtained.

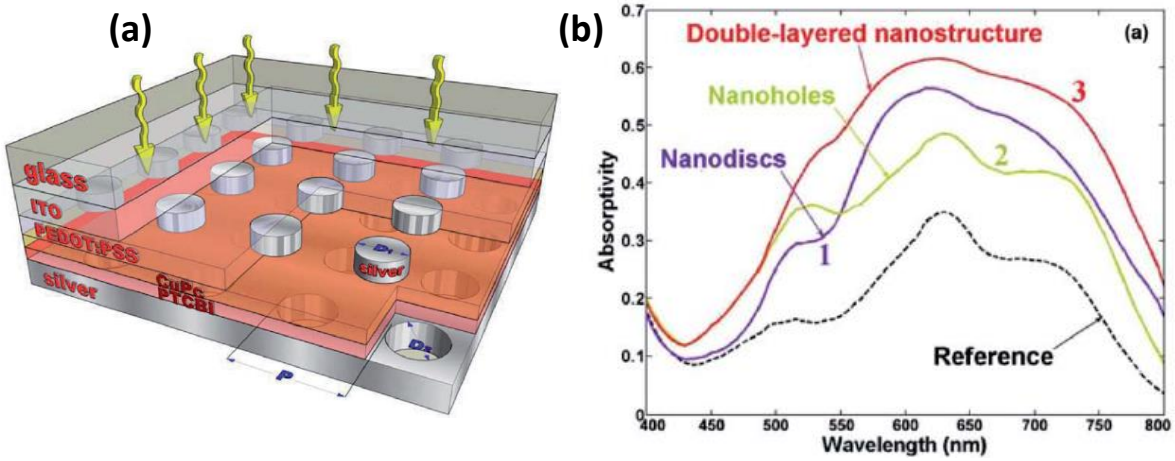

Figure 13: (a) Modified structure after addition of Ag nanodisks in buffer layer in addition to the nano-hole patterned back electrode. (b) Comparison between the absorption of each structure[17].

It could be noticed that there are many ways for incorporating plasmonic nanostructures inside OSC. However, the most commonly used materials are Ag and Au. This thesis will focus on using a new type of plasmonic materials (i.e. refractory plasmonics) to overcome the limitations of metals. These new designs are explained in details in chapter 3.

2.1.Light trapping in amorphous silicon solar cells

Amorphous silicon (a-Si) is a promising low-cost candidate that could overcome the high cost and complex fabrication of their crystalline counterparts. Since the performance of the solar cell mainly depends on their optical absorption as explained previously, thin film amorphous silicon solar cells suffer from low power conversion efficiency because of their weak light absorption. The thickness of a-Si layer could not be increased to enhance the absorption because of the random crystal structure of the material resulting in poor carrier transport properties. The carrier diffusion length in a-Si is limited to ~300 nm.

In this regard, many light trapping strategies are investigated to increase the absorption efficiency of these thin film a-Si layers. Examples of different light trapping techniques are the use of plasmonic structures such as back reflectors[38], periodic gratings[26,39–41], and metal nanoparticles. These techniques mainly depend on the excitation of surface plasmon polaritons waves or localized surface plasmons[42].

The other technique used for light trapping in a-Si is surface texturing[43]. This is usually done by texturing the transparent conductive oxide layer (i.e. the front contact) and the texture propagates through the layers and determine the morphology of the deposited a-Si layer. Periodic and random textures have been explored[44]. The record efficiency of a single junction a-Si silicon cell was attained in 2009 on a random morphology achieving 10.09% conversion efficiency[45]. The structure was implemented on random pyramidal morphology with p-i-n cell configuration with thickness equals 250 nm. Other structures include texturing the ZnO interlayer between the back contact and a-Si[46–51]. In other cases, the substrate is textured causing the deposited a-Si on top to have textured surface[52–55].

In some cases, dual light trapping configurations are implemented in the same solar cell to achieve efficient light trapping in the sandwiched a-Si layer. Lin *et al.* proposed a dual-layer nanostructured a-Si solar cell achieving 42% improvement in efficiency[56]. The structure consisted of a PDMS nanopillar

membrane on top and 3D nanodent array as back reflector on a flexible Ti foil. The structure is shown in Figure 14(a). The deposition of a-Si on top of the nanodents resulted in nano-texturing the surface of a-Si achieving higher absorption in the short wavelength range as shown in Figure 14(b). The back reflector containing the nanodents also resulted in the excitation of SPP modes and photonics modes achieving higher absorption in the long wavelength range. The addition of the nanopillar PDMS (n=1.4) on top caused further increase in the absorption at short wavelengths due to better impedance matching air and ITO (n=1.8)[57].

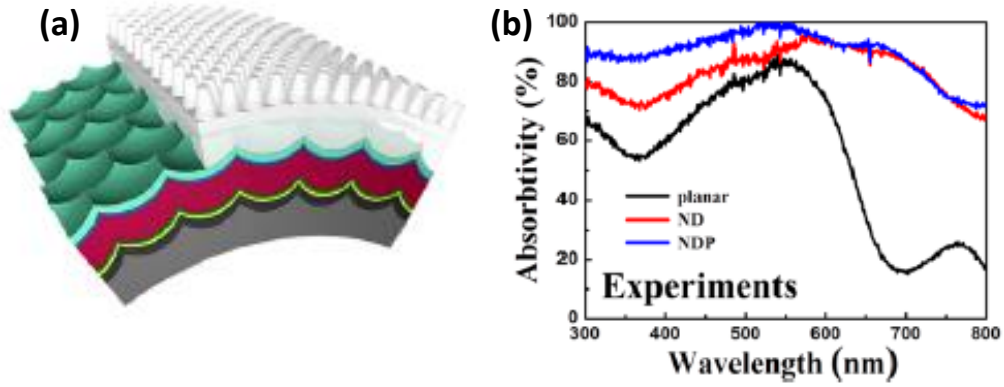

Figure 14: (a) Structure proposed by Lin *et al.* for dual light trapping in a-Si solar cell. (b) Absorption measured for the prosed structure.

Silicon nanocones (NCs) and nanowires (NWs) are another configuration that gained increased attention due to their unique optical properties[58–62]. Nanocones have proven to be the most effective 3D structure to capture incident sunlight due to graded change in refractive index provided by these structures in addition to the hot spot provided by their sharp tips. Moreover, nanowires have unique optical and electrical properties due to the decoupling of light absorption direction and carrier collection direction. Thus, they provide efficient means to efficiently capture sunlight without losing a good electrical performance.

Random a-Si NCs have been fabricated previously using reactive ion etching (RIE) along with nanospheres template[63,64]. The fabrication involved the deposition of SiO_2 using PECVD to act as a hard mask, the preparation of PS-PMMA nanospheres template by nanoscopic phase separation, and the transfer of patterned template to a-Si by RIE. This technique resulted in the formation of random

nanocone texture with low control over dimensions. In addition, no clear anti-reflection effect was observed. This was attributed to the small aspect ratio of the structure (height = 150 nm, Diameter = 50 nm). On the other hand, well-defined periodic NC arrays was reported by Zhu *et al.* using RIE etching[65]. The etch mask was formed from closed packet SiO_2 nanoparticles assembled using Langmuir Blodgett method. The NCs had an average length of 600 nm and base diameter of 300 nm. Amorphous silicon NCs fabricated using the latter method showed much reduced reflection. More than 93% absorption was reported between 400 and 650 nm wavelength. Moreover, this performance was maintained for many angle of incidences (up to 60^o).

Amorphous Silicon nanowires were also fabricated using the same method reported by Zhu *et al*.[65]. Although NWs also showed enhanced absorption compared to bare thin film with 75% absorption between 400 and 650 nm, it showed less absorption than NCs. In addition, their absorption showed a decrease with increasing the angle of incidence. This was attributed to the better impedance matching provided by the NCs. Dhindsa *et al.* also reported the fabrication of a-Si NWs using a lithographic technique[66,67]. Electron beam lithography was used with a PMMA photoresist. Periodic patterns were written to the photoresist and developed in MIBK. Electron bean evaporation of Aluminum was implemented as a hard mask. Then, a-Si was etched using RIE. 400 nm long nanowires were obtained using this method and showed increased absorption.

Although the previous methods showed enhanced absorption due to the formation of a-Si NCs and NWs relative to the bare a-Si layer, they require multiple fabrication steps and the use of expensive techniques such as lithography and RIE. In addition, they involve the removal (i.e. etching) of the some of the deposited a-Si layer.

In this thesis, we developed a new technique involving the formation of controllable NCs and NWs using one step fabrication technique that is fast, easily scalable and does not require any special conditions. The irradiation of a-Si thin films with excimer laser resulted in the formation of either NCs or NWs depending on the excimer laser conditions without etching any of the deposited a-Si film. This method along with the optical results are explicitly discussed in chapter 4. In addition, a novel design for double light trapping schemes in a-Si solar cells is numerically presented in chapter 4.

2.2.Hybrid solar cells

In the previous sections, the importance of nanostructuring the active layer was discussed and their impact on increasing the absorption is explained. Using the previously discussed light trapping schemes, the efficiency of thin film solar cells could be increased which will result in a significant decrease in the solar cell cost due to the less material usage and the less complex fabrication. This will allow the total cost of solar modules to be decreased while maintaining high efficiency. However, the quality of the material and the complexity of fabrication of bulk crystalline silicon solar cells are not the only reasons behind the high cost of solar modules. The formation of the p-n junction also requires complex fabrication that significantly contribute in increasing the cost of solar panels. Thus, another configuration is proposed that does not require this complexity in fabrication.

Hybrid solar cells provide an efficient mean for forming the junction in solar cell devices in addition to combining the advantages of both materials (i.e. organic and inorganic materials). Inorganic and organic semiconductor materials each have their advantages and drawbacks. Hybrid solar cells combine organic and inorganic materials with the purpose of utilizing the stability, industry domination and good electronic properties of the inorganic materials with the low-cost, easy processable and high optical absorption capabilities of organic materials[68,69]. In addition, the combined absorption band of each material will result in a broader absorption spectrum taking more benefit of the incident photons. However, many factors should be carefully designed in these structures to be able to achieve high efficiencies.

Generally, conductive polymers have mobility higher for holes than for electrons[70]. Thus, p-type polymers are combined with n-type semiconductors in order to donate the electrons to the inorganic material giving them a better charge transport pathway. In a pure organic solar cell, a fullerenes acceptor (i.e. typically PCBM) is added to the donating polymer. Fullerene derivatives are almost transparent and their contribution in light absorption is minimal[70]. In the hybrid structure, the organic acceptor is replaced by an n-type absorbing inorganic material. When an electron donating polymer is added to the inorganic material, charge separation takes place at the interface between both materials where electrons move to the inorganic material while the holes stay in the conductive polymer.

Many factors affect the charge separation in a polymer/inorganic interface. First factors are the interface area and the morphology of the interfaces. Thus, a well-designed structure with large interfacial area will result in better charge separation and hence, better charge collection. In addition, the differences in energy level across the interface should enhance electrons and holes transport in their respective direction. Thus, the choice of materials to be combined together must be carefully implemented. Moreover, the mixture homogeneity also affects the charge separation as well as the crystallinity of each material.

Figure 15 contains a schematic showing the charge separation and transport mechanism intro a hybrid structure. Upon light excitation, electron and hole pairs are generated where the donating polymer donates the electron to the acceptor inorganic material and the holes remains in the polymer. The importance of choosing each material is obvious at this stage. Band gap alignment should be taken into consideration to allow the transport of electrons and holes efficiently since the free carrier generation depends on the band alignment at the interface between the donor and acceptor. After charge dissociation at the interface, electrons and holes move to their respective electrodes. Here, the transport of charge carriers to the respective electrode depends on the band alignment of that electrode with the donor or acceptor material. Thus, the choice of electrodes materials should also be carefully designed.

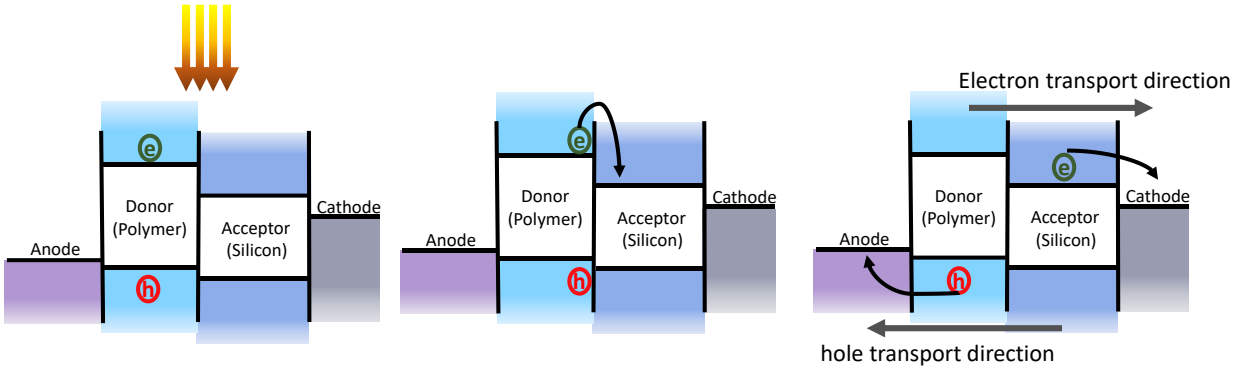

Figure 15: Schematic showing charge separation and transport mechanism upon light excitation of polymer/silicon solar cells.

As mentioned previously, the interfacial area and the morphology of the interface play a significant role in this mechanism[71]. The charge separation at the interface is the most important step on which all the remaining process depends. Larger interfacial area allows more excitons to be separated before

recombination. This will result in more carriers reaching the electrodes and higher power conversion efficiency. Nanostructuring the components of the hybrid system allows for larger interfacial area between both materials due to having many interfaces instead of the single interface if both materials are only deposited subsequently. This will give the chance for a larger number of excitons to be separated.

Several schemes could be done to allow for this large interfacial area. Only the inorganic material could be nanostructured and added to a polymer matrix. For example, the addition of inorganic nanostructures such as nanoparticles, nanorods or quantum dots in a polymer matrix[71,72]. Cadmium based quantum dots such as CdS and CdTe, lead based quantum dots such as PbS and PbSe, in addition to silicon and TiO_2 nanoparticles are all examples of inorganic nanoparticles incorporated into hybrid solar cells.

Coating a well-defined inorganic nanostructure with a polymer is another scheme that guarantee a large and a well-defined interface between both materials[73–82]. Spin coating the polymer on inorganic nanowires, adding the polymer inside nanotubes of the inorganic material, or filling an inorganic porous material with the polymer are all example of the latter scheme. Sometimes Ag nanoparticles are added to this structure for better light confinement in the absorbing layers upon the excitation of localized surface plasmons[83–86].

Another scheme includes nanostructuring both materials for better interface morphology. A high power conversion efficiency was achieved by Ren *et al*. using this scheme by adding CdS quantum dots to P3HT nanowires[87].

Since charge transport between the components of the hybrid system is of great importance, it is believed that the well-defined structures such as nanowires and nanorods have a better opportunity to achieve higher current densities[69]. In these structures, charge carriers have a continuous path to their respective electrodes. On the contrary, in case of random nanoparticles or quantum dots, charge carriers have to hop between nanostructures in order to reach their respective electrodes. Thus, in this thesis we suggest a structure containing well-defined silicon nanopillars coated with a low band gap polymer.

Spin coating a p-type polymer on silicon nanowires is a well-known technique in hybrid solar cells.

The addition of many conductive polymers, absorbing and non-absorbing on silicon nanowires are well-reported in literature. However, the choice of the polymer is crucial in this case. PEDOT:PSS is a conductive polymer that is typically used in organic solar cells as a hole transport layer. It is also used in silicon/polymer solar cells as a p-type material with n-type silicon nanowires[73,80,82,86,88–90]. PEDOT:PSS have excellent electronic properties, however, it is transparent to incident sunlight. Thus, it does not contribute in the absorption and all photons are mainly absorbed in the silicon material. P3HT:PCBM is another conductive, absorbing polymer that is typically used in organic solar cells and in hybrid solar cells[75–77,79,81,85,91]. However, its maximum absorption range is in the same maximum absorption range of silicon. Thus, they compete over the absorption of the incident photons in this range leaving the lower energy photons un-absorbed. In our opinion, the use of low band gap polymers is the most promising for incorporation with silicon nanowires[92]. It was suggested in a review by Liu that an optimal bandgap of the conductive polymer should be in the range of 1.5 eV to harvest the larger portion of sunlight. In our work, we studied few polymers having a bandgap of this range.

Moreover, the structure of the inorganic material is vital for the performance of the device. In case of using silicon nanowires as the inorganic semiconductor nanomaterial, the morphology of the nanowires affects the electro-optical properties of the solar cell device[93,94]. Thus, in our proposed structure, tapered nanowires are chosen for their remarkable light trapping properties[95–98]. A thorough optical analysis of these structures are given in chapter 5.

Chapter 3 : Light trapping in organic solar cells using refractory plasmonics

3.1.Introduction

Plasmonic devices have recently attracted enormous interest due to their unconventional optical properties. These unconventional properties arise from the resonance oscillation of free electrons in metals upon excitation by electromagnetic waves resulting in surface plasmons[99]. Great deal of interest has been directed to utilize these unusual properties in order to design highly efficient solar cells with low cost[1,100,32]. Plasmonic solar cells paved the way for new generation solar cells with optically thick and physically thin active layer achieving high absorption without sacrificing the electronic properties of the device. More specifically, ongoing intense research in plasmonic organic solar cells is carried out due to the unique properties of these devices[1,35,32,101,102].

Organic solar cells (OSC) have already reached 10% power conversion efficiency and beyond[32,13–15,10,103,11,12]. Thus, with further increase, they could be in direct competition with currently commercial solar cells. They are intrinsically thin because they suffer from low carrier diffusion length and small carrier mobility[32,104,105], which make their incorporation with plasmonic structures very promising. Ag and Au, the most widely used materials for plasmonic applications, have been extensively studied in solar cells[1,105,106,79,107]. However, they suffer from few limitations such as their lack of robustness, high cost and incompatibility with current fabrication technologies[99,108–110]. Ag has been used in many OSC devices and achieved enhanced absorption, but its chemical instability[105] along with the previously mentioned limitations hold back the commercialization of these devices.

Another set of plasmonic materials that recently gained increased attention are the transition metal nitrides[99,108,110–112]. Specifically, titanium nitride (TiN) and zirconium nitride (ZrN) are known for their unique properties of being refractory and similar in behavior to metals[99]. The zero crossing of their dielectric permittivity is in the visible range[99]. In addition to being plasmonic in the most important range for solar cells, they also exhibit outstanding advantages such as their abundance, low cost, CMOS compatibility, thermal and chemical stability, and resistance to corrosion[99].

In addition, TiN has a nonstoichiometric behavior, meaning that its properties are varied according to its deposition conditions[112]. For example, the work function of TiN film made by DC sputtering is reported to differ between 4.4 and 4.9 eV by varying the nitrogen gas flow during the reactive sputter deposition[113–115]. This is important to know since the open circuit voltage scales with the difference between the work functions of the two electrodes for non-ohmic contacts; as in the proposed device[116]. Thus, TiN could be fabricated with a low work function to achieve high open circuit voltage for solar cells. Moreover, the resistivity of TiN differ with the method of deposition and deposition parameters such as N_2 flow rate, TiN evaporation rate, film thickness and substrate temperature. It was reported that TiN fabricated using ion beam assisted deposition has resistivity of $30x10^{-8}$ Ω.m[117]. Similarly, the resistivity of ZrN varies with the N_2 flow ratio and could reach $21x10^{-6}$ Ω.m[118]. These resistivity values are less than typical of materials use as for solar cells electrodes such as Cu[119,120]. Thus, a thin layer of Cu back electrode could be used underneath the TiN layer.

In this chapter, 3D finite difference time domain (FDTD) simulations have been carried out to examine the performance of TiN and ZrN in OSC and their behavior is compared to Ag. Two dimensions (2D) periodic patterns have been assessed due to their ability to make polarization independent structures as opposed to 1D periodic strcutures[32]. The proposed structure in this chapter consists of nanopatterned back electrode with 2D periodic nanoholes. Comparisons between TiN, ZrN and Ag are discussed with analysis of the electric and magnetic field.

The analysis is done for two OSC with different active layers to generalize these designs and ensure that they could be used for different polymers to obtain similar enhancement. The first one consists of electron-donor material regioregular poly(3-hexylthiophene) (P3HT) and the electron-acceptor fullerene derivative [6,6]-phenyl-C71 butyric acid methyl ester ($PC_{70}BM$), and the second one consists of the low band gap polymer poly[3,6-bis(40-dodecyl-[2,20]bithiophenyl-5-yl)-2,5-bis(2-ethylhexyl)-2,5-dihydropyrrolo[3,4-]pyrrole-1,4-dione] (pBBTDPP2):PCBM.

3.2.Excitation of surface plasmon polaritons using ceramics in organic solar cells

3.2.1. Simulation method

3D finite difference time domain (FDTD) simulations are performed to analyze the proposed

structures. Since all the structures presented in this chapter are periodic symmetrical structures, periodic boundary conditions are used in the lateral boundaries of the simulation region and symmetry was applied to reduce the simulation time. Perfectly matched layer boundaries (PML) are applied to the vertical boundaries. The light source is simulated as a plane wave source with wavelength range from 400 nm to 900 nm. The permittivity data of P3HT:$PC_{70}BM$[121], PEDOT:PSS and ITO[122] are used in the FDTD tool for full-electromagnetic 3D simulation.

The absorption ($A(\lambda)$) was measured by calculating the difference between the power incident and the power transmitted through the active layer at each wavelength. Thus, absorption by other layers in the structure was not taken into consideration in the following calculations. Absorbed power and short circuit current calculations are done using post scripting. The absorbed power (AP) is measured using post scripting by integrating this difference over the desired range of wavelengths (i.e. from 400 nm to 900 nm) and weighting it by the AM1.5 solar intensity ($I_{AM1.5}$) as follows:

$$AP = \int_{\lambda_1}^{\lambda_2} A(\lambda)\, I_{AM1.5}\, d\lambda \qquad \text{(Eq. 1)}$$

Then, the short circuit current (J_{sc}) is calculated as a function of the absorption by the following equation[112]:

$$J_{sc} = \int_{\lambda_1}^{\lambda_2} \frac{e\,\lambda}{h\,c}\, A(\lambda)\, I_{AM1.5}\, d\lambda \qquad \text{(Eq. 2)}$$

where e is the electron charge, h is Plank's constant, and c is the speed of light. It should be noted here that the J_{sc} calculations assume that each absorbed photon will result in an electron-hole pair (i.e. internal quantum efficiency equals 100%).

Enhancement in absorbed power (AP_{enh}) is calculated using

$$AP_{enh}\ (\%) = \frac{\int_{\lambda_1}^{\lambda_2} A(\lambda)\, I_{AM1.5}\, d\lambda - \int_{\lambda_1}^{\lambda_2} A_{ref}(\lambda)\, I_{AM1.5}\, d\lambda}{\int_{\lambda_1}^{\lambda_2} A_{ref}(\lambda)\, I_{AM1.5}\, d\lambda}\, x100 \qquad \text{(Eq. 3)}$$

Similarly, enhancement in short circuit current ($J_{sc_{enh}}$) is calculated using

$$J_{sc_{enh}}\ (\%) = \frac{\int_{\lambda_1}^{\lambda_2} \frac{e\,\lambda}{h\,c}\, A(\lambda)\, I_{AM1.5}\, d\lambda - \int_{\lambda_1}^{\lambda_2} \frac{e\,\lambda}{h\,c}\, A_{ref}(\lambda)\, I_{AM1.5}\, d\lambda}{\int_{\lambda_1}^{\lambda_2} \frac{e\,\lambda}{h\,c}\, A_{ref}(\lambda)\, I_{AM1.5}\, d\lambda}\, x100 \qquad \text{(Eq. 4)}$$

where $A(\lambda)$ is the absorption in the polymer after the addition of the nanostructure and $A_{ref}(\lambda)$ is the

absorption in the polymer without the nanostructure. λ_1 and λ_2 are taken here from 400 nm to 900 nm as this is the range where the polymer has high optical responsivity.

3.2.2. Optical simulations of organic solar cells with nanopatterned back electrode

The proposed structure consists of a glass substrate, deposited on it a 20 nm indium tin oxide (ITO) layer, then a 10 nm poly(3,4-ethylenedioxythiophene):poly(styrenesulfonate) (PEDOT:PSS) buffer layer used as a hole transport layer, then a 30 nm active layer consisting of P3HT:$PC_{70}BM$. Finally, a nanopatterned electrode with a 2D periodic hole array is placed. The entire band diagram of the proposed structure is drawn in Figure 16[123,124]. The band alignments in the band diagram confirms that the proposed structure offer a feasible direction for electron transport as well as hole transport. A schematic of the whole structure is shown in Figure 17(a). The cell is illuminated from the glass substrate side with AM1.5 illumination.

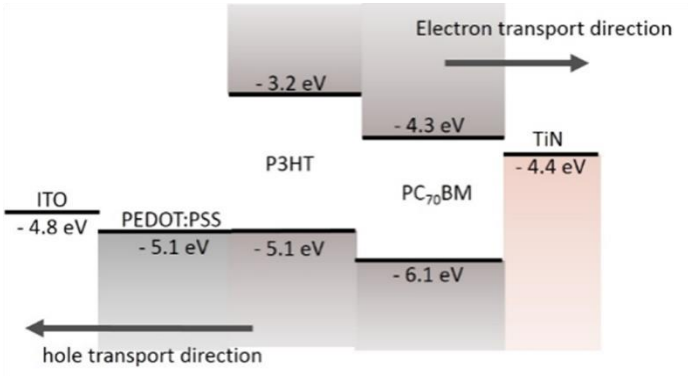

Figure 16: Band diagram of the proposed solar cell structure

First, TiN is placed as back electrode and the structure is optimized. The optimization is done by varying the TiN thickness from 10 to 80 nm and varying the nanoholes' diameter from 50 to 300 nm at each TiN thickness with keeping the period (P) equals to double the diameter (D) first and then keeping P = 1.5 D. AP is measured for each case and the highest one was found at D = 230 nm, P = 345 nm and TiN layer thickness = 35 nm.

An enhancement peak is observed in the absorption of the polymer around λ=750 nm as shown in the red dashed line in Figure 17(b). In Figure 17(b), absorption of previously published data for similar structure with Ag back electrode with 150 nm hole diameter and 300 nm period is also plotted[106]. For the Ag case, a large absorption enhancement occurred around λ=700 nm. This enhancement was

attributed to the excitation of short range surface plasmon polaritons (SRSPP) modes resulting in less amount of light transmitted through the nanopatterned metal layer than through the flat metal layer[106].

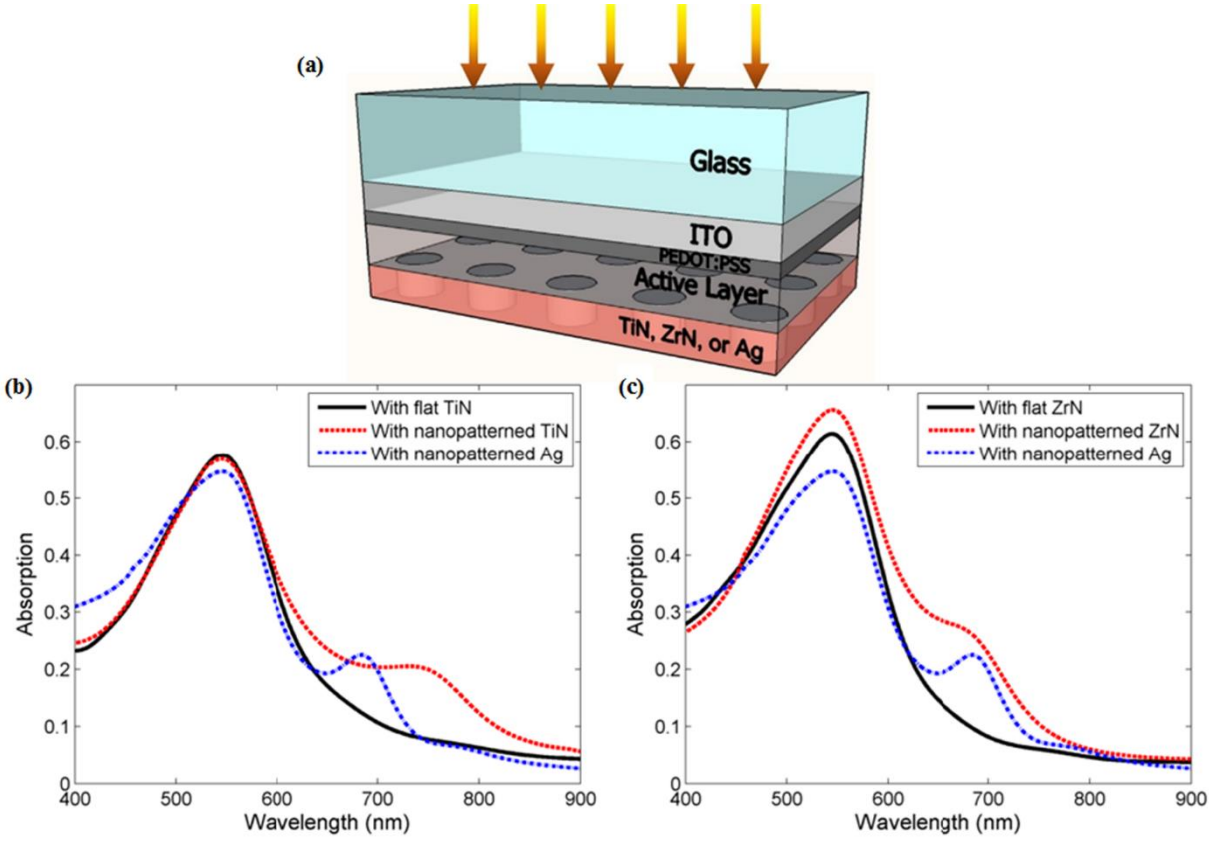

Figure 17: a) Schematic diagram of the solar cell with nanopatterned back electrode b) and c) Absorption of the cell with nanopatterned TiN/ZrN back electrode (red dashed line), with flat TiN/ZrN back electrode (black solid line) and with nanopatterned Ag back electrode (blue dashed line) for P3HT:$PC_{70}BM$.

The performance of TiN is almost similar to Ag but with even broader resonance peak (i.e. over larger number of wavelengths). This agrees with the broad peak observed for the field enhancement of TiN[111,125]. The broadband enhancement obtained using TiN makes it a possible solution for the narrow absorption peak of polymers in OSC. The optimized cell showed 14.5% enhancement in AP and 18.7% enhancement in J_{sc} than a reference cell (with flat TiN back electrode) in addition to 9% and 13.7% enhancement in AP and J_{sc}, respectively, over the structure with Ag nanopatterned back electrode due to the broader enhancement peak[106].

ZrN has similar SPP quality factor to TiN suggesting that it would induce comparable effect[126]. Thus, ZrN nanopatterned back electrode was optimized and similar enhancement was obtained with

20% increase is AP and 23.8% in J_{sc} over the reference cell (with flat ZrN electrode). This enhancement could be visualized in Figure 17(c) where an increase is found in the absorption around λ=680 nm.

The organic active layer is then changed to pBBTDPP2:PCBM; a low bandgap polymer. The cell from top to bottom is composed of glass substrate, 20 nm ITO, 10 nm PEDOT:PSS, 40 nm pBBTDPP2:PCBM active layer, and TiN or ZrN back electrode. The absorption of the optimized structure using TiN and ZrN are shown in Figure 18(a and b), respectively, compared to the absorption of the reference cell. It is shown in the figure that a large enhancement appears in the absorption range of pBBTDPP2:PCBM, from 650 nm to 900 nm, which is expected to contribute significantly in the power conversion efficiency of the solar cell. The optimization was done with the same process explained previously and resulted in 26% enhancement in AP and 29% enhancement in J_{sc} for TiN. For ZrN, 36.5% and 40.8% enhancement in AP and J_{sc}, respectively, was achieved. Using ZrN nanopatterned back electrode in pBBTDPP2:PCBM based solar cell showed the highest absorption enhancement reported for this structure.

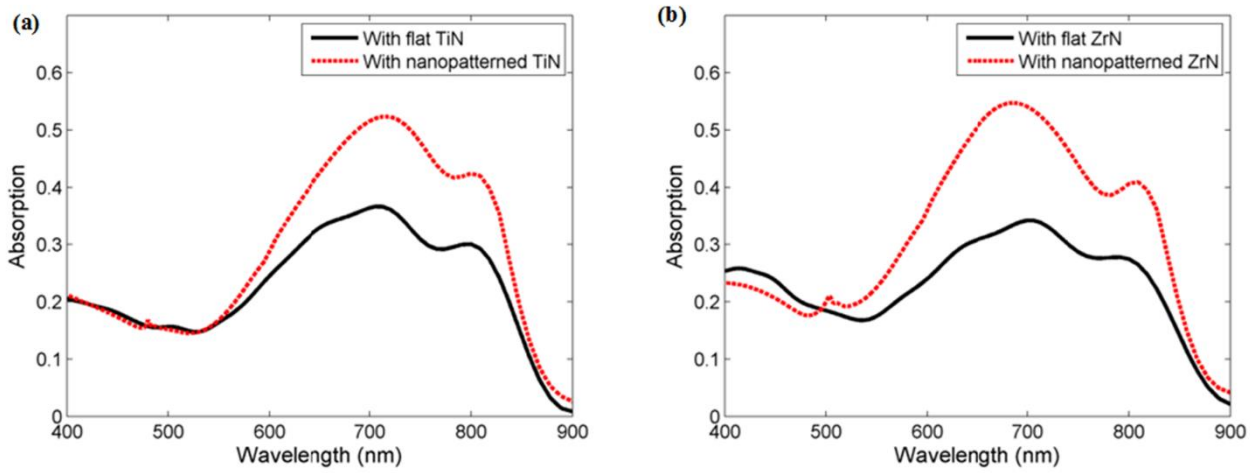

Figure 18: (a) and (b) Absorption of the cell with nanopatterned TiN and ZrN back electrode (red dashed line), respectively, and a reference cell with flat TiN and ZrN back electrode (black solid line) for pBBTDPP2:PCBM
.

In order to understand the theory behind the obtained absorption enhancement, the electric and magnetic field intensities are plotted for the P3HT:$PC_{70}BM$ based structure at the wavelength where most of the enhancement took place (i.e. 720 nm for TiN in P3HT:$PC_{70}BM$ based solar cell). Figure 19

(a) shows the x-y plane of the electric field for TiN back electrode with nanoholes. As expected, the electric field is localized around the holes. The magnetic field is also plotted at the same wavelength in the x-y plane and x-z plane as shown in Figure 19(b and c), respectively. The x-y plane shows that the plasmonic mode is confined in the TiN regions, around the holes. The x-z plane shows that the field is mainly localized in the organic active layer which explains the enhancement in the AP at this specific wavelength. This justifies the ability of TiN to support SRSPP waves similar to that of Ag and validates its usage as back electrode for potentially commercial plasmonic OSC. The fields for the pBBTDPP2:PCBM and for ZrN showed the exact similar behavior.

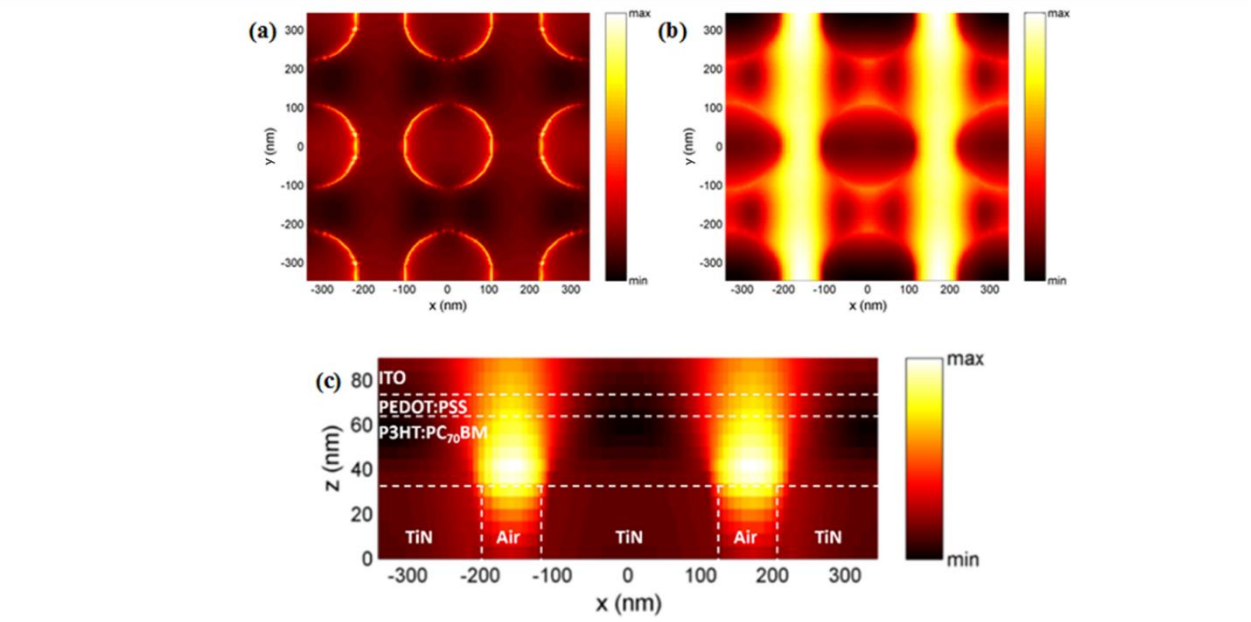

Figure 19: (a) x-y plane of the electric field. (b) and (c) x-y plane and x-z plane of the magnetic field, respectively, for the cell with P3HT:$PC_{70}BM$ active layer and TiN back electrode at λ=720 nm.

For SRSPP, the resonant wavelength (λ_{spp}) is directly proportional to the period of the nanohole array (P) from the expression[105]:

$$k_{spp} = \frac{2\pi}{\lambda_{spp}} = \frac{2\pi m}{P} \qquad \text{(Eq. 5)}$$

where m is an integer. Thus, according to the mechanism of coupling sunlight to SRSPP, it is expected that as the period of the array increases the λ_{spp} red-shifts. This could be observed from Figure 20 where a 2D map of the optical absorption enhancement as a function of the hole diameter and the

wavelength for the OSC with P3HT:$PC_{70}BM$ active layer is shown. Other parameters in the cell remained constant and the period is fixed as P=1.5 D while changing the diameter from 50 nm to 300 nm. In agreement with Eq. 5, a red shift in the absorption enhancement peak is observed as the diameter/period increases. In addition, a strong enhancement is achieved over a wide range of diameters (from 200 nm to 300 nm) which gives a good fabrication tolerance and relaxes the constrains related to synthesizing such devices making them more feasible for commercialization.

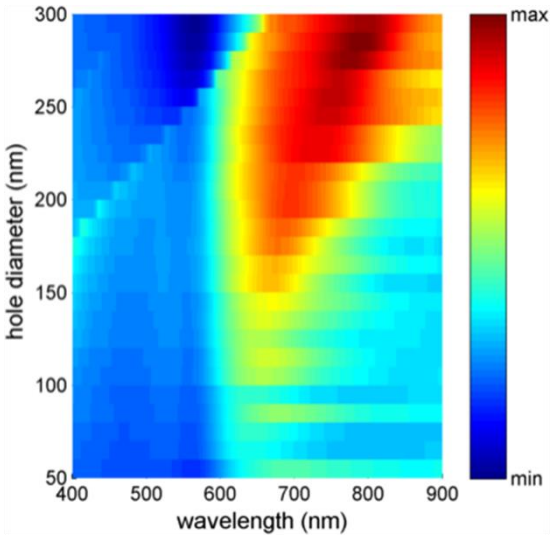

Figure 20: 2D optical absorption enhancement map as a function of the hole diameter and the wavelength for P3HT:PC70BM OSC.

The fabrication of this structure could be realized using simple 2D colloidal crystals[127]. In this method, 2D silica colloidal crystals will be spin coated on the sample and the layer to be patterned (i.e. TiN) will be deposited on the silica crystals using, for example, atomic layer deposition (ALD) or DC-magnetron sputtering. Finally, the silica crystals will be removed using ultrasonication in water leaving a TiN layer with nanoholes array on the top of the polymer.

3.3.Excitation of surface localized surface plasmons using ceramics in organic solar cells

This part highlights a new category of materials that could be used to achieve a broadband absorption enhancement in OSC and overcomes the limitations of metals, such as interband losses, high cost, incompatibility with C-MOS technology[128], and chemical instability. Refractory plasmonics have

gained increased attention recently due to their ability to excite surface plasmon polaritons (SPP) and localized surface plasmons (LSP) [99,109,112,125,129–134]. In the previous chapter, TiN and ZrN has proven to have similar behavior to Ag regarding the excitation of SPP. Here, we investigate these same ceramics for LSP applications.

Out of these refractory plasmonics, Zirconium Nitride (ZrN) has proved to be a good candidate for LSP applications due to having a high localized surface plasmon resonance (LSPR) quality factor comparable to plasmonic metals (i.e. Ag and Au)[126].

In this part, we analyze several TiN and ZrN plasmonic nanostructures in a polymer environment and in a complete OSC device. The main objective of this work is to use the light trapping capabilities of TiN and ZrN while reducing the parasitic losses inside the plasmonic nanostructure to achieve highest absorption enhancement in the active layer. These nanostructures are nanospheres (NSs), nanowires (NWs), nanocubes (NCs), spherical nanoshells (SNSs), cubical nanoshells (CNSs), and nanodisks (NDs). While several plasmonic metallic nanoshell structures have been studied before in different solar cells [24,31,135–139], we study refractory plasmonics nanoshells for the first time, to the best of our knowledge, and their effect in enhancing OSC performance.

The analysis in this work is done by calculating the Mie efficiency for TiN and ZrN nanostructures in a polymer environment. In addition, an OSC that incorporates a square periodic pattern of each nanostructure is simulated. A comparison between these structures is thoroughly analyzed and their impacts on trapping the light in the OSC device are evaluated and compared. Increasing the absorption of OSC using a cheap and abundant material such as these refractory plasmonics could considerably contribute in the commercialization of such devices.

3.3.1. Simulation method

The objective of adding TiN and ZrN nanostructures is to trap the light inside the active layer and hence increase the solar cell's absorption. Thus, the aim is to obtain large scattering efficiency with the minimum absorption efficiency for the nanostructures. Absorption inside TiN and ZrN nanostructures is considered parasitic losses because it does not contribute in the solar cells' output current[24,133,140].

Mie scattering and absorption cross section efficiencies are calculated to know the optimum radius

for maximum scattering and minimum absorption. The simulation is done using 3-D finite difference time domain (FDTD) tool by placing a total field scattered field (TFSF) source that surrounds the nanostructure. Perfectly matched layer (PML) boundaries are chosen around the structure with an x and y span of 1.5 μm in order to prevent any boundaries' reflection from affecting the calculations. Absorption and scattering cross sections are calculated by measuring the net power flow into the particle and the net power flow scattered from the particle, respectively, normalized to the source intensity

$$\text{Cross section} = \frac{\text{Power (W)}}{\text{Intensity (W/m}^2\text{)}} \quad \text{(Eq. 6)}$$

The Mie efficiency is calculated as the ratio between the cross section and the particle area. Then, the nanostructures were incorporated inside the organic solar cell. The details of each configuration is explained in the subsequent sections. However, in all organic solar cells simulations, the upper and lower boundaries in the simulation region are PML while the lateral boundaries are periodic.

The technique with which the absorption is calculated in the previous chapter measures the absorption in the whole layer without differentiating between the polymer and refractory plasmonic nanostructure. Thus, a more accurate technique had to be used to identify whether this enhancement is due to TiN or ZrN absorption or enhanced absorption in polymer. Here, the absorption inside the active layer is measured using a 3D electrical field monitor. A 3D refractive index monitor is also added to differentiate between the absorption inside the polymer and inside the TiN or ZrN by differentiating between their refractive indices. Using post scripting, a comparison between the refractive index of the polymer and TiN or ZrN is made and dependently the absorption in each material was calculated separately. Thus, the absorption calculated in the rest of the chapter is attributed to the polymer active layer only excluding any absorption in the nanostructures.

Absorbed power and short circuit current calculations along with enhancement in absorbed power (AP_{enh}) and enhancement in short circuit current ($J_{sc_{enh}}$) are done using post scripting with the same technique equations explained in the previous chapter.

3.3.2. Optical simulations of organic solar cells with TiN nanospheres (NSs)

It was stated in literature that TiN is a suitable alternative plasmonic material for localized surface

Plasmon resonance (LSPR) applications[99,110,125]. Thus, a structure that investigates this property in organic solar cells is implemented. The structure consists of a glass substrate, deposited on it a 20 nm indium tin oxide (ITO) layer, then a 10 nm poly(3,4-ethylenedioxythiophene):poly(styrenesulfonate) (PEDOT:PSS) buffer layer used as a hole transport layer, then a 30 nm active layer consisting of P3HT:PC_{70}BM and finally a TiN flat back electrode is used as shown in Figure 21. TiN nanospheres are incorporated inside the 30 nm organic P3HT:PC_{70}BM active layer. The optical absorption was calculated for nanospheres diameter ranging from 10 nm to 200 nm and the period was varied between 15 nm and 300 nm for each diameter. The vertical diameter of the NS was kept less than 30 nm to fit in the active layer. Period values less than the diameter were discarded.

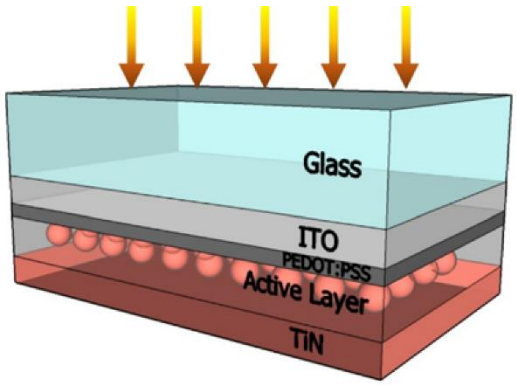

Figure 21: Schematic diagram of the cell with TiN NS incorporated inside the active layer

A large increase in the overall absorption was found. However, it was verified using the technique used to measure the absorption, explained in the previous section, that the large enhancement found was due to TiN absorption. It was reported previously that the maximum near field enhancement in TiN NSs occur at 750 nm with D = 150 nm[99,125]. Thus, the absence of strong near field enhancement or scattering of the TiN NSs in the structure is attributed to their small size. In order to verify this, TiN NSs with diameter ranging from 10 to 150 nm were placed inside a 150 nm P3HT:PC_{70}BM then pBBTDPP2:PCBM as shown in Figure 22(a). Due to the exciton small diffusion length of polymers and small electron mobility, the active layer could not be increased more than 150 nm. For both polymers, it was found that the absorption in TiN NSs increases as their diameter increases from 10 nm to 70 nm, and then it starts to decrease. The polymer absorption was almost unaffected by the TiN diameter change. This is believed to be due to the absorbing behavior of TiN (i.e. high parasitic

losses)[133]. This was proved by measuring the Mie scattering and absorption efficiencies for TiN NSs in a polymer environment (P3HT:$PC_{70}BM$) for different NS diameters. Generally, the environment surrounding the NS affects its scattering and absorption[79]. It was found that absorption cross section starts to decrease for TiN NS diameter equals 100 nm and larger (Figure 23 (a)), while scattering cross section starts to increase for particle sizes larger than 100 nm (Figure 23 (b)). It could be concluded that TiN NSs have the ability to localize light inside the active layer of the solar cell [Figure 22 (b)], but their absorption competes with the one of the polymer resulting in very limited enhancement. Thus, an optimum structure could be achieved by using TiN below the active layer as the one presented in the first section.

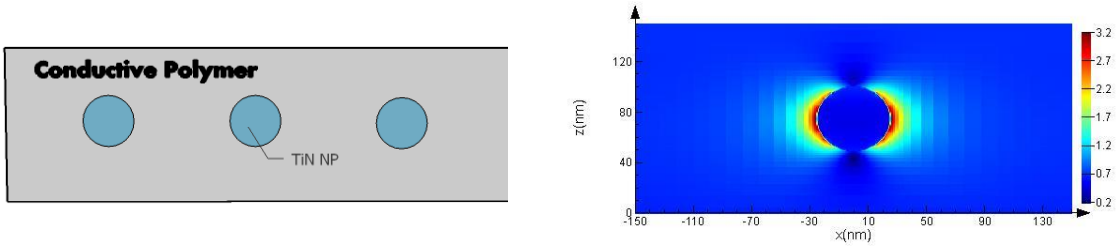

Figure 22: (a) Schematic showing the TiN NSs inside the conductive polymer active layer (b) Electric field around TiN NS in a P3HT:$PC_{70}BM$ layer.

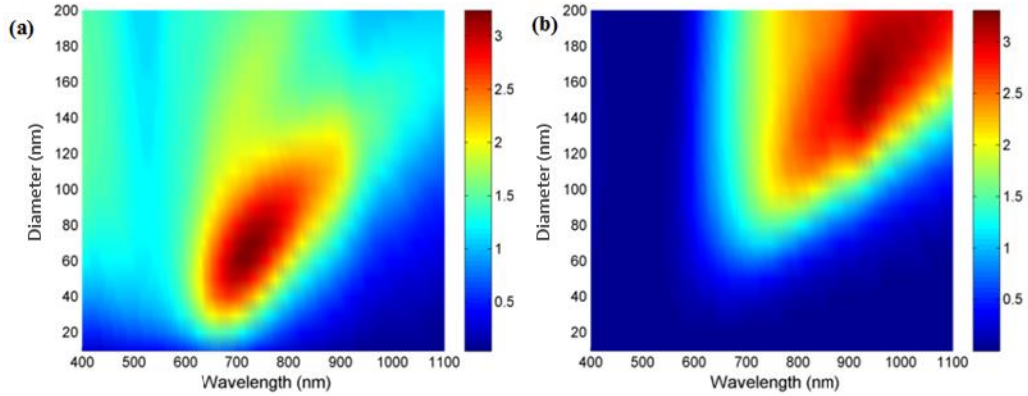

Figure 23: (a) Mie absorption efficiency and (b) scattering efficiency for TiN NSs in a P3HT:$PC_{70}BM$ environment

3.3.3. Optical simulations of organic solar cells with TiN nanowires (NWs)

Another structure is proposed in this section that could benefit from the absorption of TiN. It was reported that TiN has the ability to generate photoelectrons upon light absorption[141]. Thus, the structure is based on the ability to collect these photo-generated carriers by the back electrode. In the previous

section, the TiN NS absorption is considered as losses because there is no path for electron collection. In this structure, they are replaced by TiN short nanowires connected to the TiN back electrode so that the generated electrons in TiN could be collected efficiently and transported directly to the back electrode. Again, the structure was optimized by the same way the NSs were optimized. The length of the wire is fixed to 25 nm and the diameter/period were chosen after the optimization as D = 60 nm and P = 90 nm. Using the combination of TiN and polymer significantly enhanced the absorption due to the different absorption ranges of each material as shown in Figure 24(a).

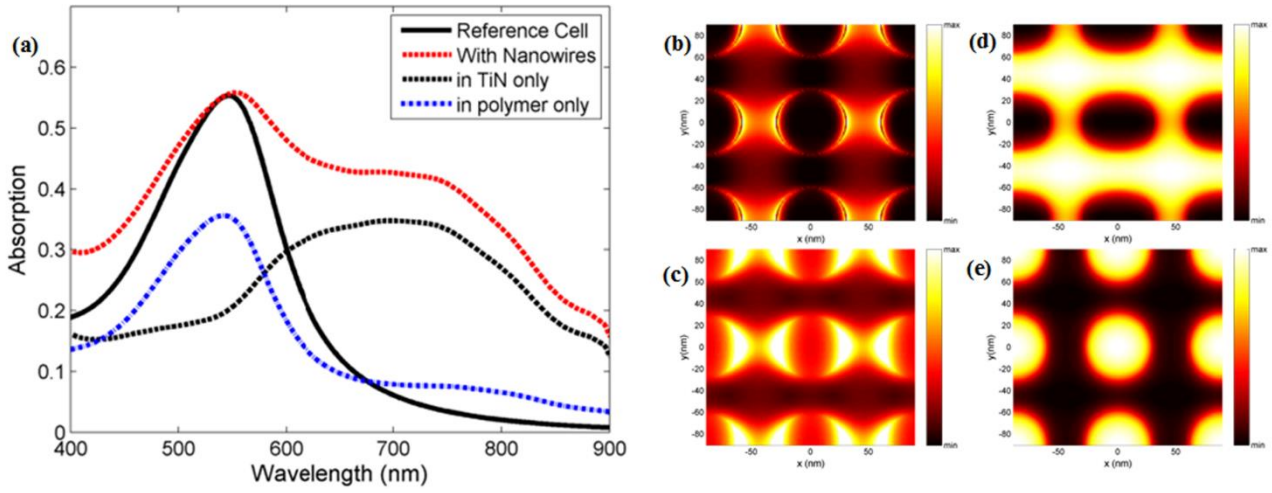

Figure 24: (a) Absorption of the cell with TiN NW (red dashed line) and reference cell with flat TiN electrode and without the NWs (black solid line) for P3HT:$PC_{70}BM$. The blue and black dashed line shows the separate absorption in P3HT:$PC_{70}BM$ and TiN, respectively. (b) and (c) Electric field at 540 nm and 720 nm, respectively, inside the active layer of the NW structure. (d) and (e) Magnetic field at 540 nm and 720 nm, respectively.

The use of this hybrid combination enhanced the AP by 95% over the reference structure. The J_{sc} was significantly improved by 123%. Separate absorption is calculated for each material using the filter method described in the previous section. Figure 25 shows a side view (a and b) and a top view (c and d) for the filter indicating the places were the organic material exists and the places where the TiN exists using the index monitor so that the absorption of each material is calculated separately. As shown in the absorption in Figure 24, the peak of the absorption of P3HT:$PC_{70}BM$ is at 520 nm (blue dashed line) and that of TiN NW is at 740 nm (black dashed line).

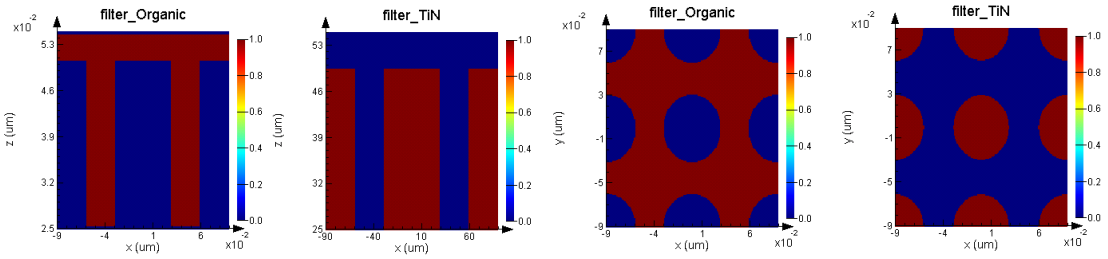

Figure 25: (a) and (b) side view for the nanowires showing the polymer's areas and the TiN nanowires' areas, respectively. (c) and (d) Top view for the nanowires showing the polymer's areas and the TiN nanowires' areas, respectively

To gain further insight on the localization of light in this structure, the electric field component of the light at the peak absorption wavelengths of P3HT:$PC_{70}BM$ and TiN are shown in Figure 24(a and b), respectively. In Figure 24(b), the light is mainly localized around the wires justifying the absorption of the polymer at λ=540 nm. In Figure 24(c), the electric field started to be more intense inside the wires explaining the high absorption of TiN. The field is also localized around the NWs which clarifies the absorption enhancement that appears in the polymer (blue dashed line) in this range over the structure without the nanowires (black solid line). It is even more apparent in the magnetic field distribution (Figure 24 (d and e)) that the light is localized in the polymer at 540nm and inside the wires at 720nm.

Regarding the fabrication this configuration, the TiN NW structure will be fabricated using e-beam lithography and the active polymer (e.g. P3HT:$PC_{70}BM$) will be spin coated on the patterned TiN. The PEDOT:PSS will be deposited on ITO/glass substrate using spin coating. Finally, the PEDOT:PSS/ITO/glass part will be coated on the P3HT:$PC_{70}BM$/TiN part and fixed with a clip as reported previously in similar structures[85]. TiN NSs could be also fabricated using e-beam lithography[99]. NSs will be added on the back electrode with the periodic structure and the active polymer will then be spun on the NSs after sintering to ensure that the NSs will keep their periodicity after spin coating. Finally, the PEDOT:PSS/ITO/glass part will be coated on the P3HT:$PC_{70}BM$/TiN part and could be fixed with a clip similar to the NW configuration.

3.3.4. Optical simulations of organic solar cells with ZrN nanospheres (NSs) and Nanocubes (NCs)

Zirconium Nitride (ZrN) has proved to be a good candidate for LSP applications due to having a

high localized surface plasmon resonance (LSPR) quality factor comparable to plasmonic metals (i.e. Ag and Au)[126]. DFT analysis has shown that ZrN and HfN have the highest localized surface plasmons quality factory out of all refractory plasmonics (i.e. even higher than TiN) [126]. Hence, in this section and the following sections, a prime focus has been given to several ZrN nanostructures with the permittivity data taken from the published DFT analysis[126].

Before incorporating ZrN nanostructures inside an OSC device, an isolated single nanostructure is studied in P3HT:$PC_{70}BM$ environment. Figure 26 shows the Mie scattering and absorption efficiencies for various diameters of ZrN nanoparticles. For nanospheres, it could be seen that scattering starts to increase at diameter of 60 nm while absorption decreases as shown in Figure 26 (a) and (b). These results agree with previously published data calculated by DFT for ZrN[126]. However, the resonance peak here is slightly lower and red shifted due to the higher refractive index of the environment. Additionally, the scattering peak red shifts at larger radii causing it to deviate from the polymer's absorption range which is undesirable. Thus, it could be concluded that an optimum diameter would be from 70 to 140 nm. After D=140nm, although absorption cross section significantly decreases, the scattering peak starts to appear after 900 nm which is outside the absorption range of the polymer and wouldn't affect the performance of the organic solar cell.

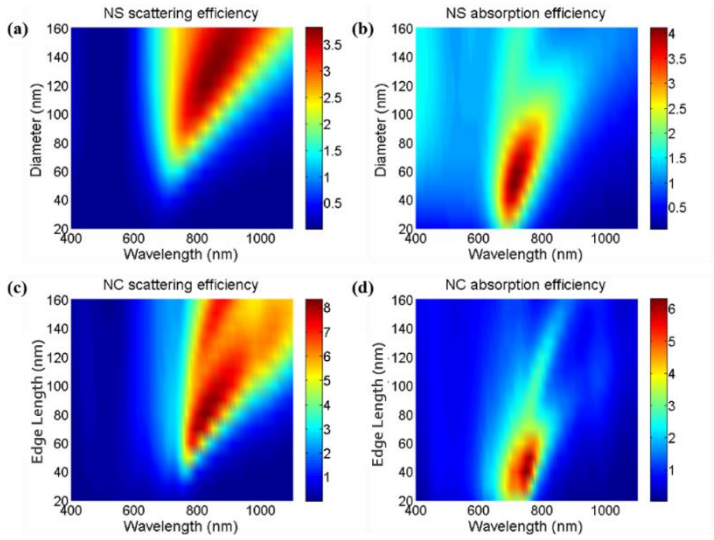

Figure 26: (a) Scattering and (b) absorption efficiencies of ZrN NSs with different diameters in P3HT:$PC_{70}BM$ environment. (c) Scattering and (d) absorption efficiencies of ZrN NCs with different edge lengths in P3HT:$PC_{70}BM$ environment.

Nanocubes (NCs) are another plasmonic structure that gained increased attention[142–144]. They have the ability to cause a high near field enhancement due to the hot spots at their sharp corners. Scattering and absorption efficiencies were also calculated for ZrN NCs with various edge lengths. At small edge lengths, from 20 nm up to 60 nm, the NCs showed absorption efficiency larger than the NSs as shown in Figure 26 (c). For larger NCs, absorption efficiency was decreased with more enhanced scattering efficiency compared to their NSs counterparts [Figure 26 *(*d)].

Next, ZrN NSs are incorporated in a whole OSC device, shown in Figure 27 (a), consists of 20 nm Ag back electrode, P3HT:$PC_{70}BM$ active polymer, 10 nm PEDOT:PSS, 20 nm ITO and finally glass substrate. Figure 27(b) shows a cross section of the structure with the NS embedded inside the active layer. The upper and lower boundaries in the simulation region are perfectly matched layer (PML) and the lateral boundaries are periodic.

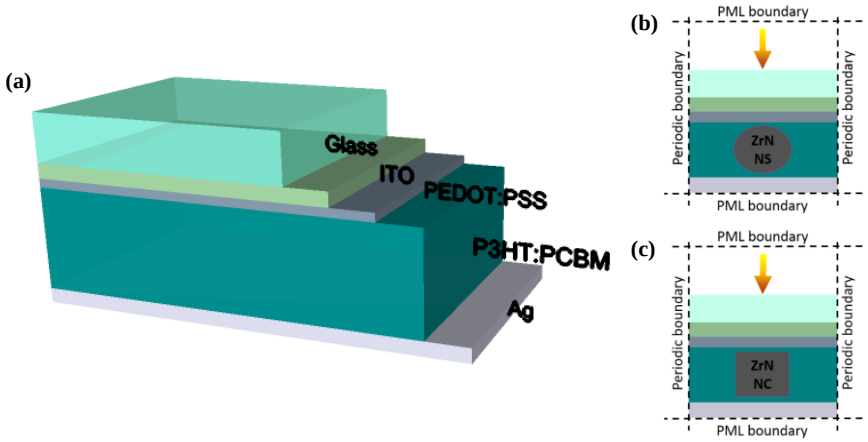

Figure 27: (a) 3D structure of the proposed organic solar cell. (b) and (c) Cross sections of the structure containing ZrN nanoshperes and nanocubes, respectively.

In order to calculate the optimum enhancement that could be achieved, the following optimization technique was implemented. An initial coarse sweep over the diameter (D) was done with a minimum D=50 nm and maximum D=T-10, where T is the polymer's thickness. This was done for polymer thicknesses from 60 to 150 nm. In agreement with the Mie efficiency analysis, absorbed power was maximum at D=130 nm and then it started to decrease. The maximum enhancement was found when the polymer's thickness was 100 nm and D=90 nm. At lower polymer's thicknesses (80 nm and less), the diameter of the NS is restricted to maximum of 70 nm where the absorption efficiency of the

nanoparticle starts to increase and thus overall enhancement is reduced. Several periods for each case was simulated and it was found that the larger period (i.e. three times the diameter (P=3D)) shows higher absorbed power than the smaller ones. In the case of 100 nm polymer thickness, the effect of diameter variation on the absorbed power and short circuit current enhancement is shown in Figure 28 with P fixed as triple the diameter (3D). As expected, the larger particles cause a larger enhancement. Thus, the optimized structure have D = 90 nm and P = 270 nm. The calculated AP_{enh} is 22% and Jsc_{enh} is 29%. This enhancement could be seen in Figure 29(a) where two peaks are observed at 730 nm and 620 nm (red dashed line).

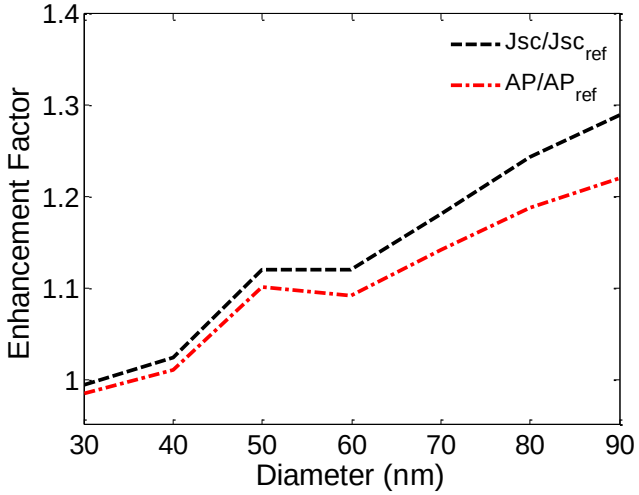

Figure 28: Enhancement factor of the absorbed power (red line) and short circuit current (black line) for various ZrN nanospheres' diameters in 100 nm P3HT:PC70BM active layer.

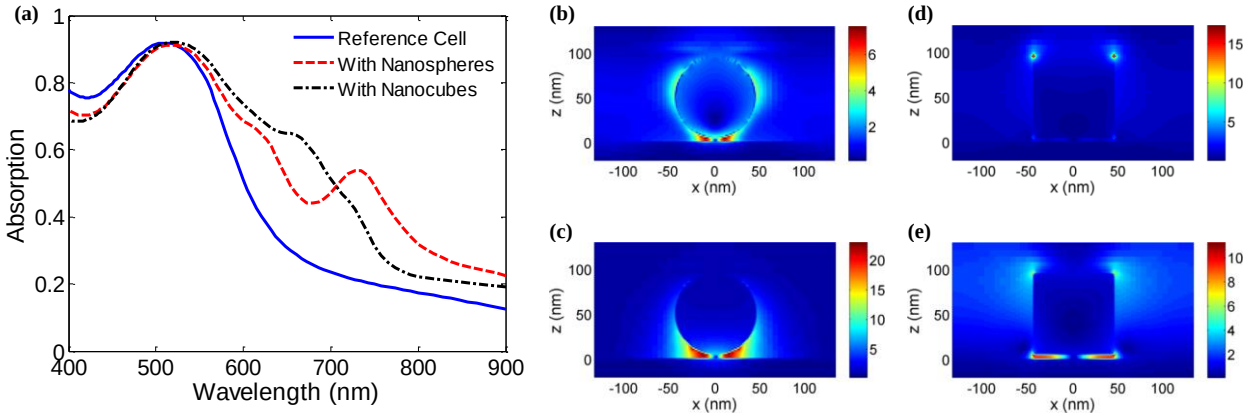

Figure 29: (a) Absorption in P3HT:PC_{70}BM with (red dashed line) and without (blue solid line) the addition of ZrN NSs. (b) and (c) Electric field distribution inside the structure with NS at 620nm and 730 nm, respectively. (d) and (e) Electric field distribution inside the structure with NC at 650nm and 850 nm, respectively. Units of the bar code are V/m.

The absorption profile in Figure 29(a) can be explained by analyzing the electric field distribution at different wavelengths. At 620 nm, light localization around the NS could be observed confirming the capability of ZrN to excite strong LSPR [Figure 29(b)]. At 730 nm wavelength, a much higher field was observed in the space between the NS and the Ag back electrode [Figure 29(c)] justifying the strong enhancement in absorption observed at this wavelength.

For NCs, the maximum scattering efficiency occurred at edge lengths between 70 and 90 nm. Thus, a NC with an edge length of 90 nm was incorporated in the same device instead of the NSs. The period was varied between 120 nm and 270 nm. At P=270 nm, an enhancement of 21.7% in absorbed power was calculated and Jsc_{enh} was 27%. This enhancement could be seen in Figure 29(a) (black dashed line). Although NCs have higher scattering efficiency than NSs, overall AP_{enh} and Jsc_{enh} are almost the same. This could be attributed to two reasons. The first one is that the field enhancement in the case of NCs has smaller area than in the case of NSs (i.e. only at the sharp corners of the cube as shown in Figure 29(d)). The second reason could be noticed from Figure 29(e) where the field enhancement between the NC and Ag back electrode has a lower value than between the NS and Ag.

Transition metal nitride nanoparticles have been fabricated previously using both top down and bottom up approaches[99]. Many non-lithographic techniques have been used to produce titanium nitride (TiN) powder in a solution such as nitridation of Ti[145] or TiO_2[146]. TiN nanocubes have been produced using laser ablation of TiN powder target[147] or from aqueous solution of commercially available TiN powders[111]. Due to the high similarity between TiN and ZrN structure and properties, same techniques could be used to fabricate ZrN nanospheres and nanocubes.

3.3.5. Optical simulations of organic solar cells with ZrN Nanoshells

While metallic nanoshells have been studied and utilized before in several solar cells such as dye sensitized solar cells[136], Si solar cells[24,137–139], and perovskites[135], we propose a nanoshell configuration where the core consists of SiO_2, covered with ZrN shell. A systematic study for scattering and absorption efficiencies of ZrN spherical nanoshells (SNS) and cubical nanoshells (CNS) have been implemented. Isolated single nanoshell in a polymer environment is studied first to examine the effect of changing the core diameter (core D) and shell thickness (shell T) on the scattering and absorption peaks. The

refractive index of SiO_2 is fixed to 1.45 throughout the simulation range and the extinction coefficient is zero.

For SNS structures, the resonance peak changes with changing both the core D and shell T[24], which could be tuned to be in the polymer's absorption range despite the type of the polymer used. This could be confirmed by the scattering and absorption efficiencies shown in Figure 31(a and b) for fixed SiO_2 core diameter of 50 nm and a variable shell thickness, respectively. The extinction efficiency, which is the sum of the scattering and absorption efficiency, of SNS with variable shell T is shown in Figure 30(a). By increasing the shell thickness, the extinction resonance is slightly blue shifted, unlike the case of solid NS[24]. Interestingly, a very high absorption peak appears at thin ZrN shell thickness (5 nm), then it decreases with increasing shell T [Figure 31(b)]. This is attributed to a strong light confinement at the ZrN and SiO_2 interface. This field could be seen in Figure 32 for SNS with core D=50nm and shell T=5nm at 870 nm . While the conventional plasmonic mode between the SNS and surrounding medium is excited, similar to the case of NS, another plasmonic mode between the SNS and SiO_2 core is excited and is stronger at small SNS thicknesses[24]. Figure 31(a) shows the scattering efficiency which experience an increase with increasing shell T.

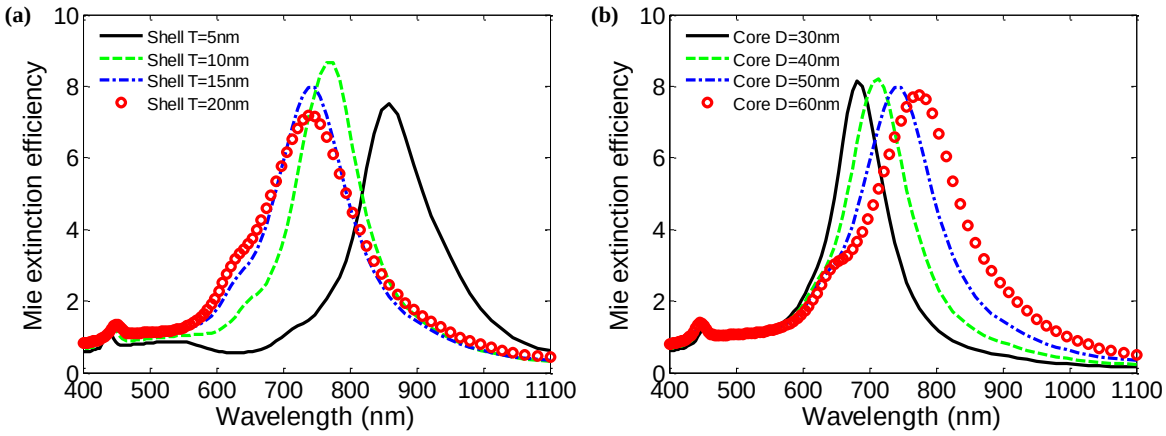

Figure 30: Extinction efficiency of spherical nanoshells with (a) various shell thicknesses and fixed core diameter (core50nm) and (b) various core diameters with a fixed shell thickness (15nm).

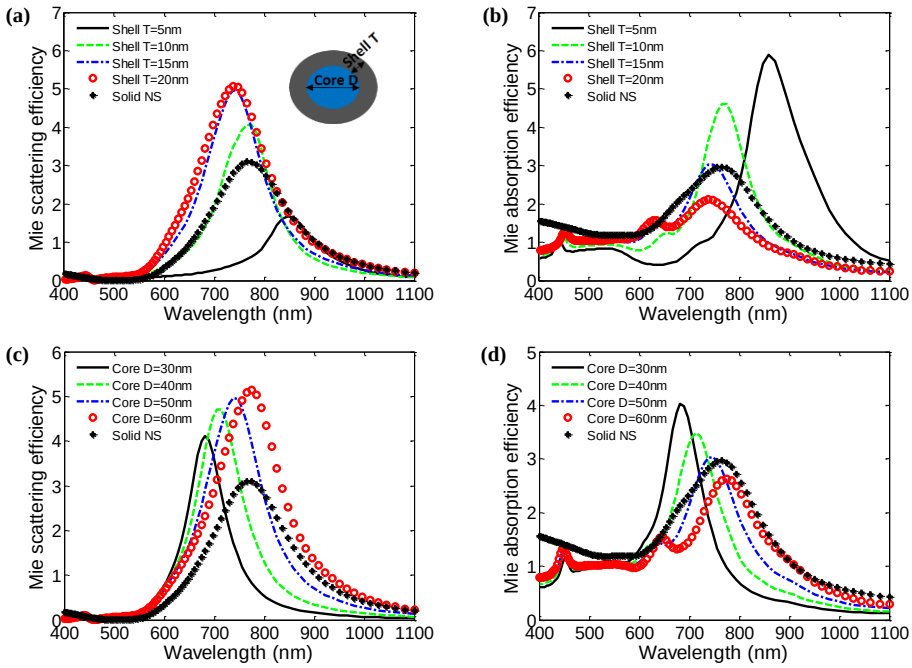

Figure 31: (a) Scattering and (b) absorption efficiencies of SNS with various shell thicknesses and fixed core diameter (50nm), in comparison with solid NS with D=90nm. (c) Scattering and (d) absorption efficiencies of SNSs with various core diameters and a fixed shell thickness (15nm).

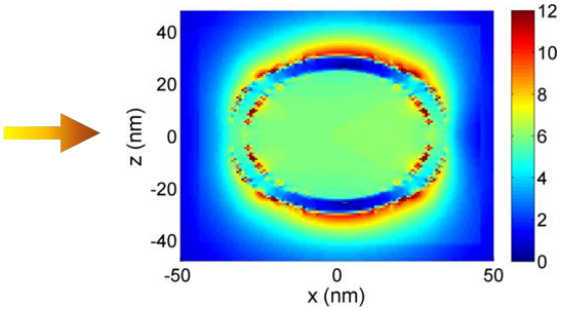

Figure 32: Electric field around spherical nanoshell with core D=50nm and shell T=5nm at 870nm. Notice the localization of light at the interface between the SiO_2 core and the ZrN shell. Units of the bar code are V/m.

On the other hand, fixing the shell thickness and varying the core diameter showed a similar behavior to conventional NSs where the resonance wavelength in the extinction efficiency is red-shifted with increasing the core diameter [Figure 30(b)]. Although the extinction efficiency showed almost a fixed amplitude for all core diameters, the scattering efficiency increased with increasing the core diameter [Figure 31(c)] while absorption efficiency decreased [Figure 31(d)]. The decrease in the absorption efficiency is probably due to the less usage of lossy ZrN material.

To compare between the behavior of NSs and SNSs, scattering and absorption efficiency of NS with

D = 90 nm have been added to Figure 31 (black dotted line). It could be seen from Figure 31(a) that, except for shell T = 5nm, the Mie scattering efficiency of SNSs overcomes the one of the 90 nm diameter solid NS. Mie absorption efficiency is less for SNS with shell T= 20nm and T=15 nm. In case of varying the core D, the scattering efficiency is less for the solid NS compared to all SNSs' cores. Nevertheless, the absorption efficiency is less than the solid NS in the case of SNS core D= 50 nm and 60 nm. The high absorption efficiency for nanoshells is due to the mode between the SiO_2 and the ZrN shell layer.

Cubical nanoshells (CNS) are analyzed with the same method. Mie extinction efficiency has been calculated for ZrN CNS with the same core edge length (L = 60 nm) and different shell T (Figure 33). Similar to SNSs, a blue shift in the resonance wavelength of the extinction efficiency occurs while increasing the shell T, with decrease in the absorption efficiency peak as shown in Figure 34(b). However, for wavelengths below 900 nm, the absorption efficiency increases with increasing the shell thickness. The absorption efficiency for the 90 nm solid NC is higher than all CNSs in the visible range. Figure 34(a) shows that scattering efficiency peak slightly increases only from shell T=5nm to shell T=10 nm and then it decreases. It could be noticed that small shell T in CNS also cause a significant increase in the absorption efficiency analogous to what was found in SNS. However, this high absorption peak in this case is outside the absorption range of the polymer. Shell T = 10 nm shows a low absorption efficiency for wavelengths below 900 nm among the other CNSs and highest scattering peak. Therefore, a CNS with shell T = 10 nm has been integrated into the OSC device.

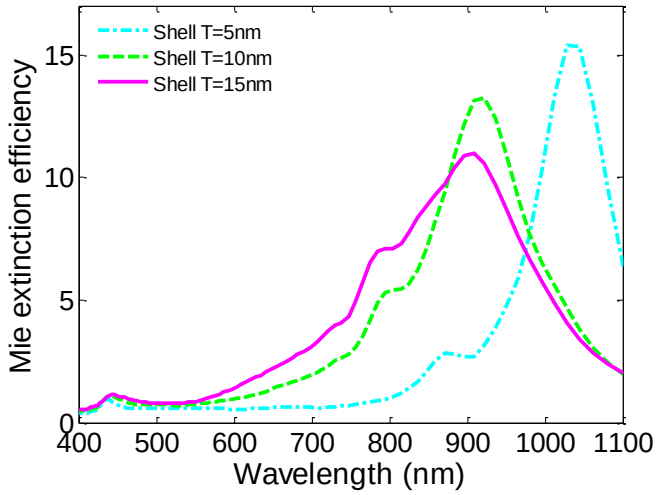

Figure 33: Extinction efficiency of cubical nanoshell with core edge length=60nm and various shell thicknesses.

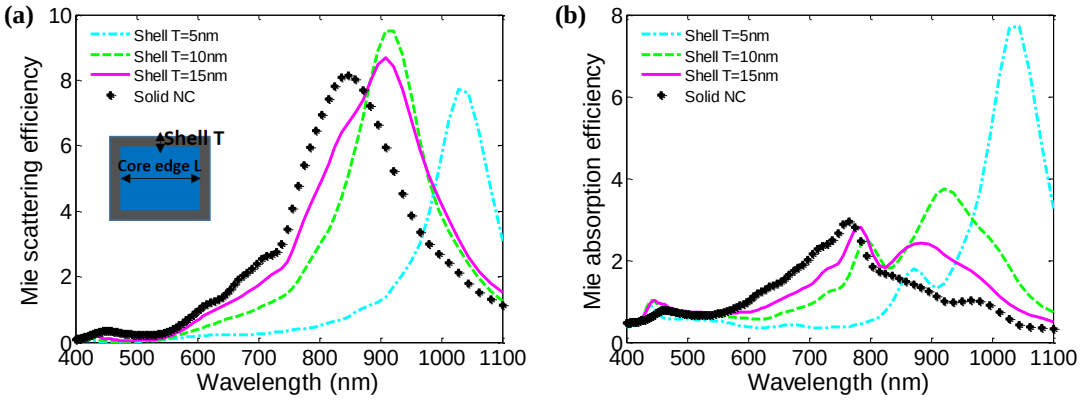

Figure 34: (a) Scattering and (b) absorption efficiencies of CNS with various shell thickness and fixed core edge length (60nm).

To summarize the above results, it could be concluded that increasing shell T increases the scattering efficiency for SNSs, which is favorable, and decreases the absorption efficiency (i.e. parasitic losses). In addition, the resonance wavelength is blue-shifted for both SNSs and CNSs. Oppositely, increasing the core D causes a red-shift in the resonance wavelength while increasing the scattering and decreasing the absorption. Thus, an optimum shell T/core D could be found to achieve the desired condition of maximum scattering and minimum absorption. The maximum scattering efficiency was found for the CNS with the fixed core edge length of 60 nm and shell T = 10 nm. This structure also showed low absorption efficiency in the visible range. Consequently, the dependence of the absorbed power on each

parameter is taken into consideration while optimizing the nanoshells inside the OSC.

For SNS, the dependence of the absorbed power in the organic solar cell on the SiO_2 core D was calculated and plotted in Figure 35(a) with fixed P = 250 nm and shell T = 20 nm. For all core diameters, the enhancement in absorbed power was higher in the case of SNS than for NSs (i.e. with the same core D of ZrN and no shell). Thus, for core D = 40 nm, an absorbed power enhancement map for the shell T versus P is plotted to locate the highest absorption enhancement inside the polymer [Figure 36(a)]. An important thing to note in the enhancement map is that the same enhancement could be found for a range of P and D which significantly relaxes the fabrication constrains of this structure and facilitate its commercial production. The maximum enhancement is found for the larger periods (i,e 220-300 nm) and shell T (i.e. 20 and 25 nm). Thus, a SNS with core D = 40nm, shell T= 25 nm, and P = 280 nm is simulated. Two resonant peaks similar to the ones achieved using ZrN NSs appeared. An increase in the absorption relative to the reference cell occurred at these peaks resulting in 21% enhancement in absorbed power and 28% in short circuit current. The electric fields at these two wavelengths are shown in Figure 37(b) and (c).

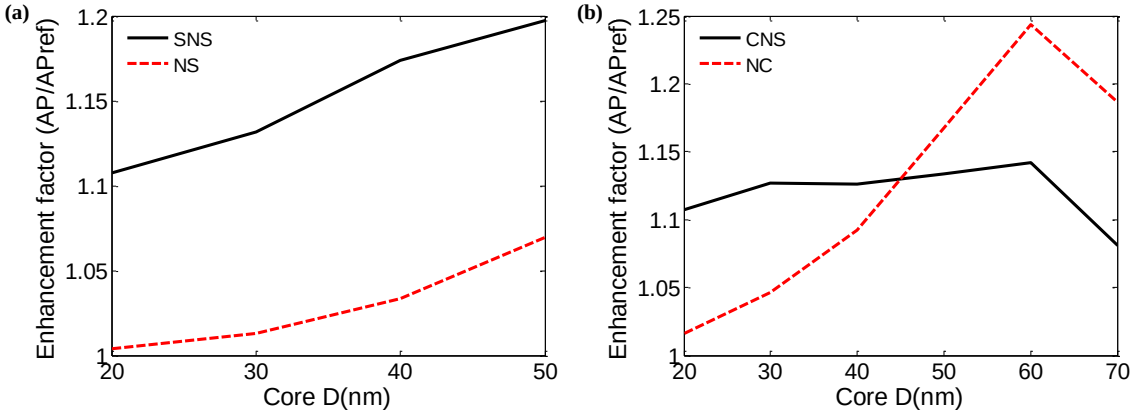

Figure 35: (a) Enhancement factor for spherical nanoshells with different core diameters and shell T = 20nm (black solid line) and for nanospheres with different diameters (red dashed line) for P = 250 nm. (b) Enhancement Factor for cubical nanoshells with different core edge lengths and shell thickness = 10nm (black solid line) and for nanocubes with different edge lengths (red dashed line) for P = 250 nm.

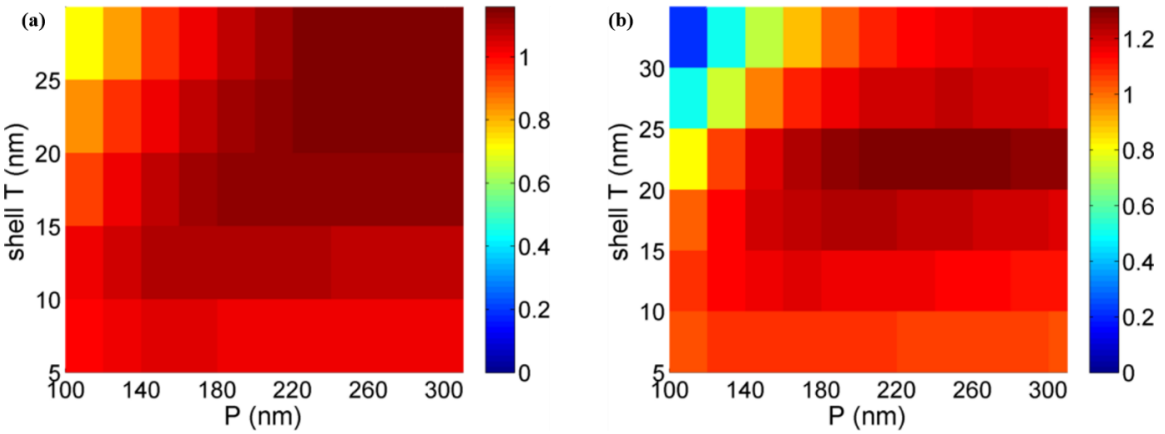

Figure 36: Absorbed power enhancement map for (a) spherical nanoshell with core diameter = 40 nm and (b) cubical nanoshell with core edge length = 30 nm.

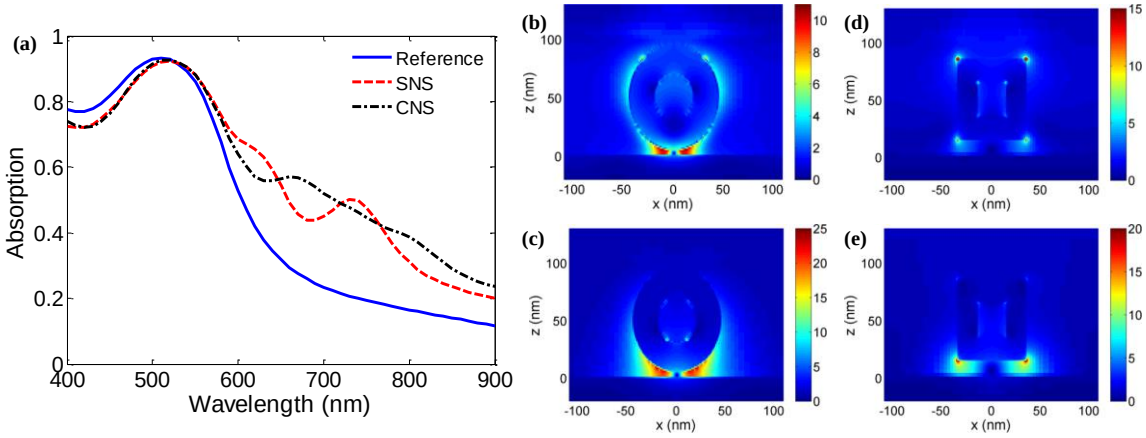

Figure 37: (a) Absorption in P3HT:$PC_{70}BM$ for a reference cell (blue line), with SNS (red dotted line), and with CNS (black dotted line). (b) and (c) Electric field distribution inside the structure with SNS at 630nm and 740 nm, respectively. (d) and (e) Electric field distribution inside the structure with CNS at 700nm and 825 nm, respectively. Units of bar code are V/m.

For CNSs, the dependence of the enhancement factor on the core edge length was measured first while keeping P = 250 nm and shell T = 10 nm. Figure 35(b) shows this enhancement compared to the one obtained for solid NC of same core edge length of ZrN and no shell. It could be seen that CNS show better enhancement factor for small core edge lengths. However, for larger core edge lengths, solid NC shows higher enhancement factor. Thus, a sweep over the period and shell T for a fixed core edge length of 30 nm is implemented and shown in Figure 36(b). Highest enhancement occurred for shell T = 20 nm and a wide range of periods (i.e. from 180 nm to 300 nm). Absorption for the structure with core L = 30 nm, shell T = 20 nm and P = 220 is plotted in Figure 37(a) (black dotted line). CNS achieved the highest enhancement in all structures presented in this paper. The optimized structure containing CNS

exhibited an enhancement in absorbed power of 25.6% and 34.7% enhancement in short circuit current. Electric field for this structure is shown in Figure 37(d) and (e) at 700 nm and 825 nm, respectively. The higher near field enhancement obtained for CNS compared to the solid NC is the reason for the better enhancement. It could be seen that ZrN CNS have the ability to localize light better than solid NC achieving higher absorption in the active polymer. It could be concluded that the two main mechanisms responsible for this absorption enhancement in this work are the surface plasmon enhanced scattering and the field enhancement due to the excitation of localized surface plasmons.

Regarding the fabrication of SNS and CNS structures, SiO_2 nanoparticles could be fabricated with one of the well-known methods such as the Stober method[148]. The ZrN shell could be added using a similar technique reported previously [149]. In this technique, they coated carbon nanotubes with TiN shell by depositing TiO_2 precursors on the surface of carbon nanotubes. Conversion from TiO_2 to TiN occurred when the samples were heat treated in ammonia gas. Thus, ZrN nanoshells could be fabricated by the deposition of ZrO_2 precursors on the SiO_2 particles followed by heat treatment in ammonia gas.

3.3.6. Optical simulations of organic solar cells with ZrN Nanodisks (NDs)

The minimum diameter for ZrN nanoparticles, to achieve high scattering, restricts the reduction of active polymer layer thickness to less than 100 nm. Hence, other nanostructures could be exploited for thinner polymer layers. ZrN nanodisks (NDs) of 20 nm length was added into the same device but with 50 nm thick P3HT:PC_{70}BM and 20 nm PEDOT:PSS. It is expected that ZrN NDs are also capable of supporting LSP modes and will be able to increase the polymer's absorption. The location of ZrN NDs is varied to achieve highest absorption in P3HT:PC_{70}BM. ZrN NDs were incorporated outside the active layer [Figure 38(a)], at the interface between buffer and active layer [Figure 38(b)], and inside the active layer [Figure 38(c)].

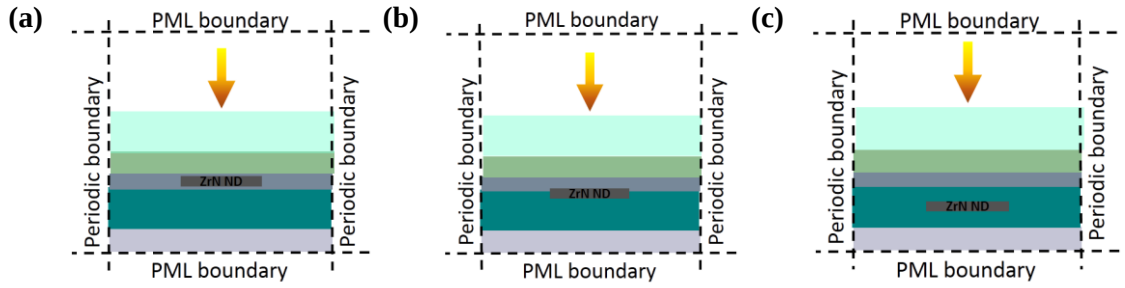

Figure 38: OSC structure with ZrN ND (a) inside the buffer layer, (b) at the interface between active and buffer layer, and (c) inside the active layer.

The absorbed power was calculated for each structure for various ND diameters (D) and periods (P). The enhancement map was plotted by measuring the enhancement factor of the absorbed power for each D and P combination. For each ND location, the optimum D and P combination is identified and marked with a white dashed square in Figure 39. It could noticed that there are multiple D and P combination that gives high enhancement factor relaxing the fabrication tolerance of these structures. It could be concluded from comparing between the enhancement maps that the lowest enhancement happens when the ND is in the buffer layer. This is also obvious from its absorption spectrum in Figure 40(a). It could be easily seen that the absorption due to the presence of the ND in the buffer layer shows the least enhancement. This is explained by looking at the electric field of this configuration in Figure 40(b). A high electric field enhancement could be observed which proves that ZrN NDs are capable of supporting LSP modes. However, this strong near field is distributed latterly along the PEDOT:PSS layer and does not penetrate strongly in the active layer limiting the increase in absorption in P3HT:$PC_{70}BM$[104].

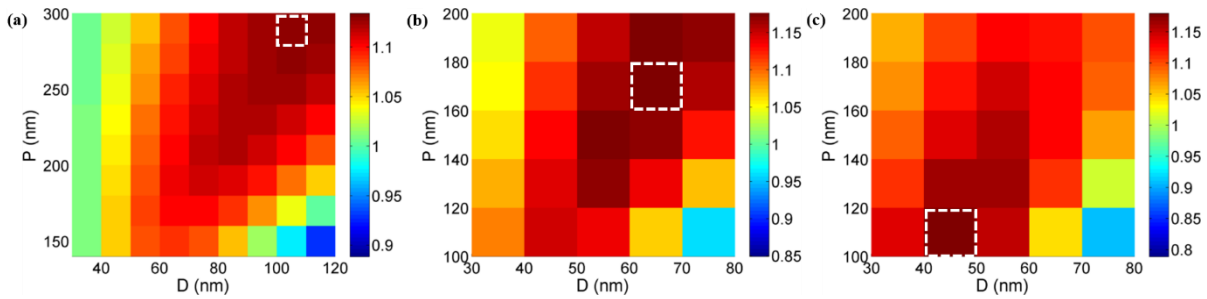

Figure 39: Enhancement map for ZrN nanodisks (a) inside buffer layer, (b) at the interface between buffer and active layer, and (c) inside the active layer.

For the other two configurations, the maximum enhancement observed in the absorbed power is similar [Figure 39 (b and c)]. To know the exact enhancement achieved for each configuration, the AP_{enh} and Jsc_{enh} were calculated for all three structures. In the case of ND at the interface and in the active layer, AP_{enh} are found to be 17.6% and 16.9%, respectively. In the case of ND in buffer layer, AP_{enh} was only 13.2%. The lateral localization of light directly affects the P3HT:PC_{70}BM layer when the ND is directly placed in it [Figure 40 (d)]. When the ND is placed at the interface, an even stronger near field enhancement is obtained at the lower edges of the ND that is directly inside the P3HT:PC_{70}BM layer [Figure 40 (c)].

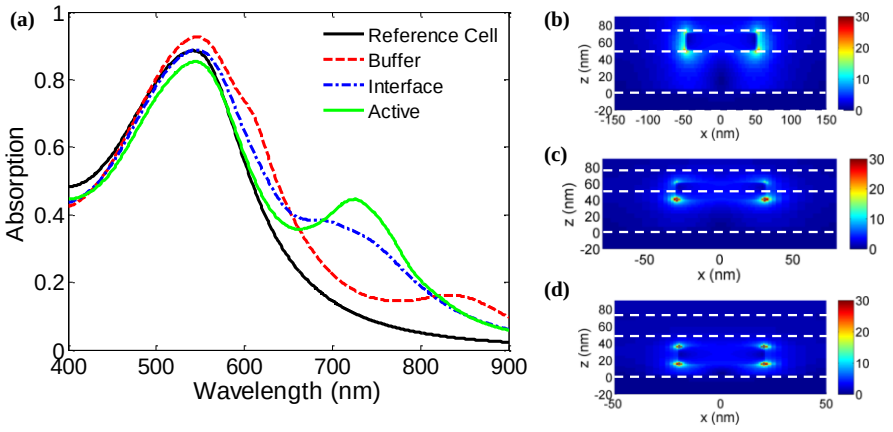

Figure 40: (a) Absorption inside P3HT:PC_{70}BM for all 3 configurations for the ZrN ND. (b), (c), and (d) Electric field for ND inside the buffer layer at 850nm, at the interface at 712 nm, and inside the active layer at 720nm, respectively. Units of the bar code are V/m.

ZrN nanodisks could be fabricated with electron beam lithography. Electron beam lithography has been used previously to obtain TiN nanodisks after deposition of TiN films using dc reactive magnetron sputtering[150]. ZrN films could also be deposited using dc magnetron sputtering [131] and array of nanoparticles could be fabricated using electron beam lithography.

3.4.Conclusion

Localizing light using plasmonic nanostructures has the potential to overcome the absorption limitations of OSC and improve their power conversion efficiency. It was proven that transition metal nitrides have the potential to replace Ag and Au in certain plasmonic applications. In this chapter, simulation results show that some transition metal nitrides such as TiN and ZrN have

comparable performance to Ag in addition to providing indispensable advantages such as the abundance, chemical stability, lower cost and broader resonance peak. We numerically demonstrate absorption enhancement in organic solar cells (OSC) due to the incorporation of TiN and ZrN nanopatterned back electrode. Up to 40% enhancement in short circuit current is reported for organic solar cell based on pBBTDPP2:PCBM active layer with ZrN nanopatterned back electrode.

We numerically demonstrated also broadband absorption enhancement in organic solar cell (OSC) using several ZrN nanostructures. Scattering and absorption efficiencies of ZrN nanospheres (NSs), nanocubes (NCs), spherical nanoshells (SNSs), and cubical nanoshells (CNSs) in a polymer environment have been calculated using FDTD tool. The highest absorption enhancement with 34.7% increase in short circuit current is obtained in the organic solar cell with ZrN CNSs. In addition, it was proved that ZrN NDs are also capable of localizing the light laterally achieving absorption enhancement in ultra-thin active layers. Using ZrN nanoparticles with wide size distribution could help in making the enhancement even broader by exciting multiple plasmon resonances. In addition, randomly distributed nanoparticles with close proximity could be studied in order to make use of the plasmon near field coupling resonance between the particles. Using plasmonic nanostructures for absorption enhancement in OSC could overcome their major limitation (i.e. low absorption). Implementing this using a cheap and abundant material such as ZrN could significantly contribute in the commercialization of such devices.

3.5.Future directions

Future investigations will require more understanding for the electrical behavior of the structure to know the internal quantum efficiency and take it into consideration while calculating the power conversion efficiency. In addition, actual fabrication and characterization of these devices will help in giving a deeper understanding of their behavior.

Chapter 4 : Novel light trapping techniques in amorphous Silicon solar cells

4.1.Introduction

The deposition of highly crystalline silicon layers requires very high energy, temperature and cost. Thus, thin film amorphous silicon (a-Si) solar cells have gained increased attention due to the less energy and cost needed for their fabrication compared to their crystalline counterparts[44]. It offers an affordable alternative with shorter energy-payback time[56]. In addition, deposition of amorphous silicon (a-Si) does not require high temperature or energy (i.e. typical temperature between 100 and 250ºC). It is a direct band gap material, which makes the excitation of electrons upon photons absorption easier compared to indirect band gap materials such as crystalline silicon. However, amorphous silicon has higher refractive index (4.32) and thus higher surface reflection due to the high mismatch between the a-Si and air refractive indices. Additionally, it suffers from low carrier diffusion length due to the randomness of its crystal structure which significantly limits its thickness to few hundred nanometers[47]. This small thickness reduces the absorption within the solar cell. Thus, several techniques have been developed to overcome this limitation, such as surface texturing[47,54,48,55,50,43], anti-reflection coatings[151], plasmonics[152–154], and photonic crystals[155]. One way to efficiently trap light inside the silicon active layer is to introduce a surface texture that could scatter light inside the underneath silicon layer. In addition, surface texturing significantly reduces the reflection at a wide angle[20].

Surface nanotexturing have been introduced on a-Si solar cells using several techniques. Usually, the underlying substrate is textured using chemical techniques and the texture propagates through the a-Si layer deposited on top[46,47,54,56,49]. Among various 3D nanostructuring, silicon nanocones (NCs) are considered as the most efficient light trapping configuration for solar cells because of their better refractive index matching with air[58]. Arrays of a-Si NCs have been fabricated using reactive ion etching along with nanospheres template[63–65]. Although it resulted in enhanced absorption in a-Si, this technique is expensive and requires multiple fabrication steps.

Moreover, the unique one-dimensional structure of silicon nanowires (NWs) made it one of the most

promising configurations to realize highly efficient solar cells with low cost[156]. The decoupling of the absorption depth and minority carrier diffusion length in the NW structures could solve the trade-off between obtaining highly absorbing solar cells with decent electrical properties[93,157,158]. Crystalline silicon NWs have been extensively studied numerically and experimentally[159–162]. However, to obtain the NWs structure, etching in the deposited material is one the most commonly used methods which results in wasting some of the deposited Silicon material[161,162].

Driven by the promising optical and electrical properties of NWs, it is believed that NWs fabricated from low cost a-Si materials using an easily scalable method and with enhanced optical properties, would be a strong candidate in the photovoltaic market. Amorphous silicon nanowires have been fabricated previously using lithography and reactive ion etching[65–67]. Although well controllable NWs with enhanced absorption were reported, these techniques are expensive and require multiple fabrication steps.

Here, we report a lithography-free one step fabrication method of large area a-Si NCs and NWs using excimer laser. In this method, the silicon is not etched to produce the NCs or NWs as conventional methods. However, the silicon mass is re-distributed within the sample forming the nanostructure and thus, none of the deposited silicon material is lost. Furthermore, this method is fast, easily scalable and does not require the use of a catalyst, special gases, vacuum, or clean room environment. This work reports for the first time, to the best of our knowledge, the fabrication of Silicon NWs using excimer laser. NWs with length up to 2.7 μm are obtained. Large and broadband absorption enhancement is obtained for nanostructured a-Si compared to the bare a-Si over the entire visible wavelength range. Angle dependence analysis showed that the reduced reflection is stable for many angle of incidences. The current work provides a detailed systematic study on the effect of changing excimer laser parameters on the morphology and optical properties of a-Si.

4.2.Fabrication of amorphous Silicon nanostructures using excimer laser

4.2.1. Experimental details of fabricating amorphous Silicon nanocones and nanowires

All fabricated samples went through the same fabrication process shown in Figure 41. The parameters of each stage in the fabrication process varied depending on the desired final structure.

Amorphous Silicon films were deposited on glass slides substrates from a SiH_4 source using plasma enhanced chemical vapor deposition PECVD (Oxford instruments). Prior to deposition, glass slides were cleaned using acetone, IPA and piranha. They were rinsed with acetone, IPA and DW, placed for 30 minutes in piranha solution (Sulfuric acid:H_2O_2 4:1), rinsed with DW again then immediately placed in the PECVD for deposition. Cleaning and deposition were done in a clean room environment.

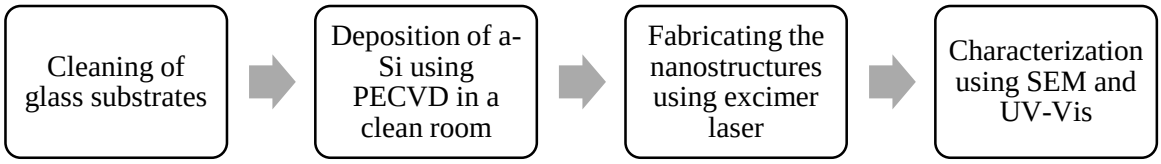

Figure 41: Fabrication process of laser annealed samples to form nanocones or nanowires.

Deposition parameters were fixed for all deposited a-Si films (pressure=1.5Torr, temperature=250 ºC, and power=6 W). He gas was added to obtain uniform films with the percentage of SiH_4:He set to 1:1[163,164]. The time was varied to give the desired thickness.

The deposited a-Si films were then irradiated by a KrF excimer laser (Lambda Physik, Compex205, λ = 248 nm, pulse duration = 24 ns). The irradiated spot area varied with the laser energy but was typically few millimeters. Samples were mounted on a motorized computer controlled stage in a closed chamber. The chamber is put under reduced pressure of 3.5 mbar during irradiation. The energy density, frequency, and time of irradiation were varied and the effects of changing each parameter on the morphology and optical properties of the films were systematically analyzed. Figure 42 and Figure 43 illustrate the whole fabrication process of Silicon nanocones and nanowires using excimer laser, respectively.

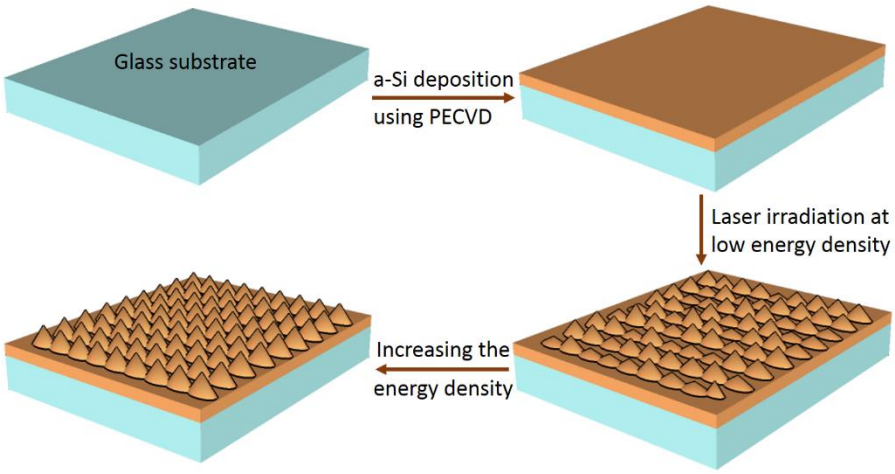

Figure 42: Sketch of the schematic fabrication process of Silicon nanocones

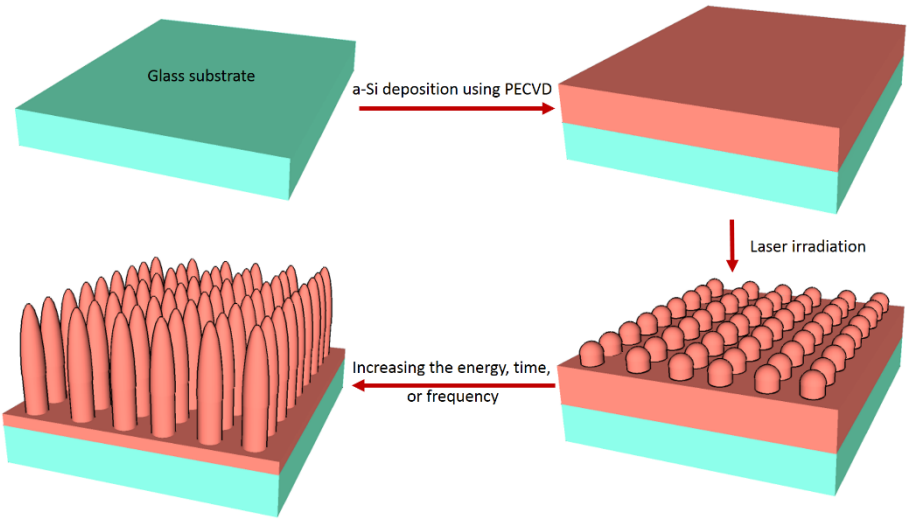

Figure 43: Sketch of the schematic fabrication process of Silicon nanowires.

The samples were then characterized using Zeiss LEO field emission scanning electron microscopy (FESEM) and Zeiss atomic force microscopy (AFM) for morphology analysis. For FESEM samples, 30 seconds Au sputtering was applied beforehand to make the surface conductive. All cross section images are taken with 20° tilt. The absorption was measured using a spectrophotometer (Perkin-Elmer Lambda, UV-VIS NIR) and the reflection at multiple angles was measured using the universal reflectance accessory.

As mentioned before, all PECVD parameters were fixed for all samples except the time. The time was varied to obtain the desired thickness of a-Si film. The time was set to 20 minutes for samples used in the fabrication of nanocones and 50 minutes for samples used for the fabrication of nanowires. Using

SEM, the thicknesses of the a-Si films after deposition was measured. A Sample of the SEM images for the deposited a-Si for nanocones fabrication and nanowires fabrication are shown in Figure 44 (a and b), respectively. The thickness of the deposited film was ~370 nm for nanocones samples and ~820 nm for nanowires samples.

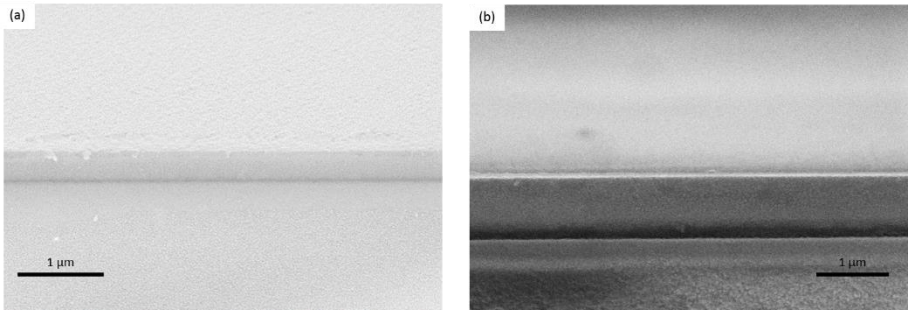

Figure 44: Amorphous Silicon films deposited at (a) 20 minutes and (b) 50 minutes

4.2.2. Morphology and optical properties of Silicon nanocones

Amorphous Silicon nanocones (NCs) are formed by gradually increasing the laser energy during laser exposure time. The energy density was gradually increased from 45 mJ/cm^2 to a maximum energy. The maximum energy density (E_{max}) was varied between 215 mJ/cm^2 to 520 mJ/cm^2.The frequency (f) was initially fixed to 10 Hz and the exposure time (t) was fixed to 40 seconds. It should be noted here that this energy is measured on the sample stage in air and the actual experiment is done in reduced pressure (3.5 mbar) as mentioned in the experimental details section. Thus, the actual energy density reaching the sample in reduced pressure is slightly less that these measured values.

Arrays of random NCs were formed with different sizes depending on the reached maximum energy. Silicon NCs were distributed throughout the laser spot. Figure 45 shows the NCs the center of the laser spot at different energies. Figure 45(a) and (b) shows the NCs formed with E_{max} = 215 mJ/cm^2. It could be seen that only the upper part of the deposited a-Si layer contributed in forming the NCs while leaving approximately 350 nm thick a-Si layer underneath. This indicates that the NCs are formed by transferring the a-Si material from some parts to others not by etching any of the deposited a-Si. Increasing the E_{max} increases the size of the NCs; the length and the diameter. Figure 45(c)-Figure 45(h) show the NCs formed with E_{max} equals 260 mJ/cm^2, 300 mJ/cm^2, and 350 mJ/cm^2, respectively.

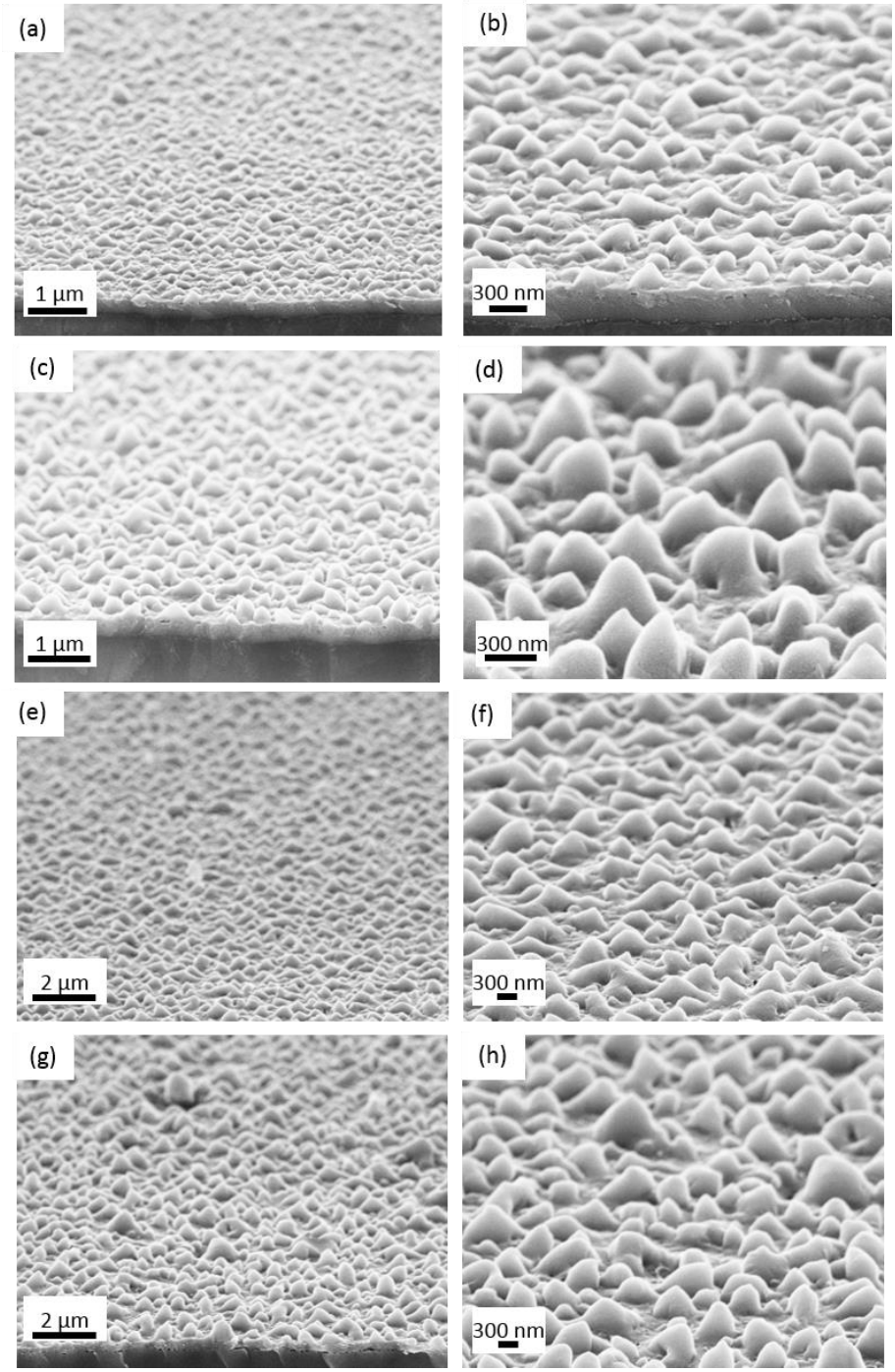

Figure 45: SEM images of NCs formed with increasing the energy density from 45 mJ/cm^2 to (a,b) 215 mJ/cm^2, (c,d) 260 mJ/cm^2, (e,f) 300 mJ/cm^2, and (g,h) 350 mJ/cm^2. All images are taken with 20^o tilt.

The length and diameter distribution for each case was measured. Figure 46 shows of the measured length and diameter distributions for all fabricated NCs. NCs formed with E_{max} equals 220 mJ/cm^2 had

an average length of 126 nm while the base diameter is 188 nm. Increasing the E_{max} to 260 mJ/cm^2 caused a rapid increase in the length (265 nm) and diameter (417 nm) [Figure 45(b)]. Further increase in E_{max} (300 mJ/cm^2) increased the length to 393 nm and the diameter to 613 nm as shown in Figure 45(c). For E_{max} equals 350 mJ/cm^2, the length of the NCs reached 450 nm and the diameter 650 nm as shown in Figure 45(d). It could be seen that NCs with lengths larger than the deposited a-Si is obtained confirming that the transfer in material is the mechanism forming the NCs. Clearly, both the length and the base diameter of the NCs increase with increasing E_{max}. The effect of changing the E_{max} on the length and base diameters is summarized in Figure 47.

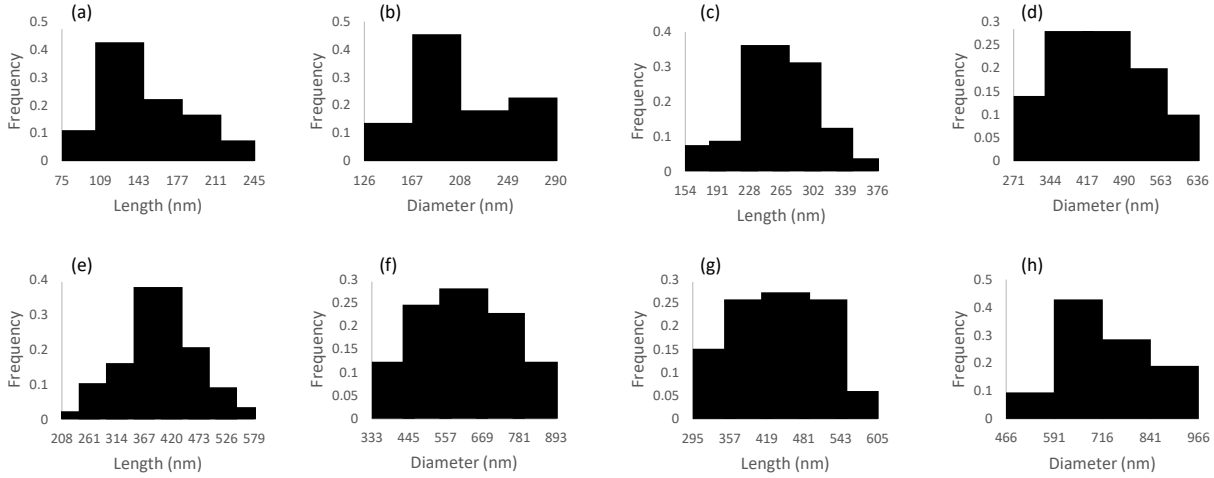

Figure 46: length and diameter distribution for the sample with (a,b) E_{max} = 215 mJ/cm^2, (c,d) E_{max} = 260 mJ/cm^2, (e,f) E_{max} = 305 mJ/cm^2, and (g,h) E_{max} = 345 mJ/cm^2, respectively.

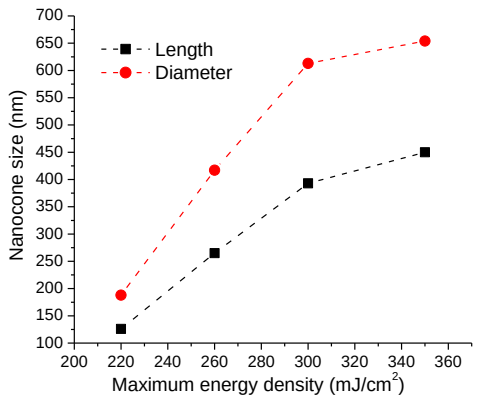

Figure 47: Effect of increasing the maximum energy density on the length (black cube line) and diameter (red circle line) of the formed NCs.

At 350 mJ/cm$^{2.}$, most of the deposited a-Si was already consumed in forming the NCs. Thus, any added energy resulted in forming irregular shapes as shown in Figure 48(a and b) for E_{max} equals 390 mJ/cm^2. Moreover, the layer started to be ablated with additional increase in energy as could be seen in the larger voids between the structures in Figure 48(c and d) for E_{max} equals 520 mJ/cm^2.

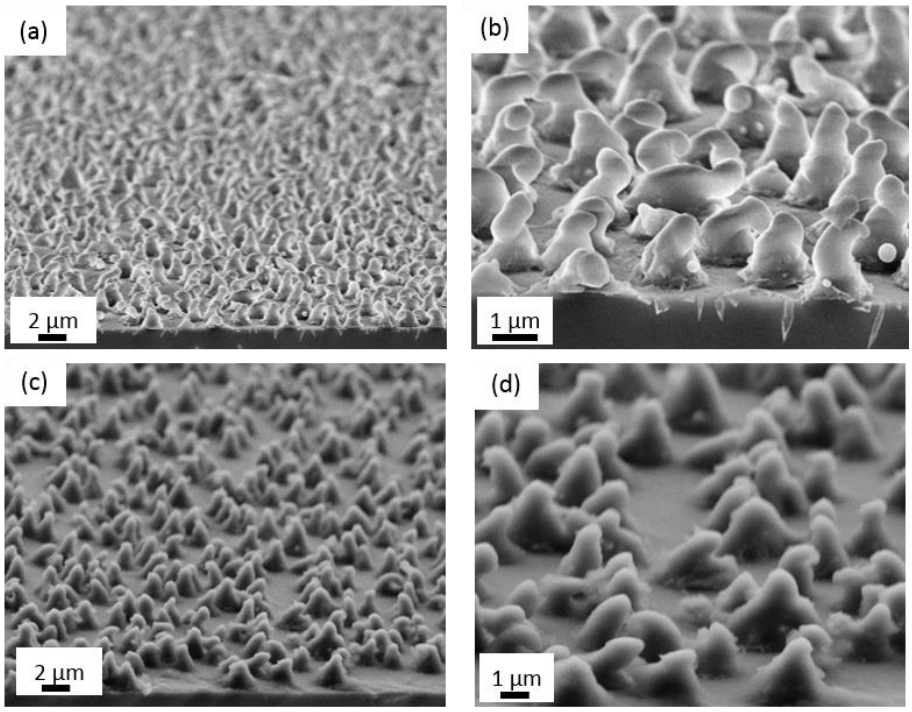

Figure 48: SEM images of NCs formed with increasing the energy density from 45 mJ/cm^2 to (a,b) 390 mJ/cm^2, and (c,d) 520 mJ/cm^2. All images are taken with 20^o tilt.

An important remark that could be noted here is that the formation of NCs does not significantly depend on the thickness of the a-Si film. In other words, if a-Si is larger in thickness, a-Si NCs will still be formed on top of the a-Si layer. This could be seen in Figure 49 where laser annealing is performed for a-Si samples deposited for 50 minutes and having a thickness of ~820 nm. The E_{max} used in this case was 300 mJ/cm^2 and the time increased to 60 seconds. It could be observed that NCs similar to the precious ones are formed on thicker a-Si film. Thus, the thickness of the underneath a-Si film could be adjusted by adjusting the original thickness of the deposited a-Si.

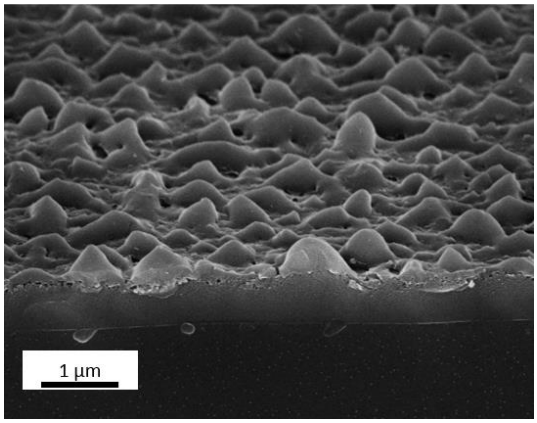

Figure 49: SEM image of Silicon NCs fabricted with 800 nm thick Silicon

The energy is gradually increased during laser irradiation to avoid exposing the extremely thin layer to high energy values at once. Expsoing the thin film to energy of 260 mJ/cm^2 directly caused the formation of irregular shapes as shown in Figure 50(b) compared to the formation of well defined NCs formed with gradually increasing the energy from 45 mJ/cm^2 to 260 mJ/cm^2. It should be noted also that the irregular shapes observed in Figure 50(b) are formed after 25 seconds only of laser exposure. Thus, these irregular shapes are formed even if less exposure time is implemented. The same observations are seen when the laser energy is set to 360 mJ/cm^2 as shown in Figure 50(e) . If the time is increased to 40 seconds, laser ablation starts to occur removing parts of the deposited a-Si layer as showin in Figure 50(c and f) for direct laser exposure with energy equals 260 mJ/cm^2 and 345 mJ/cm^2, respectively.

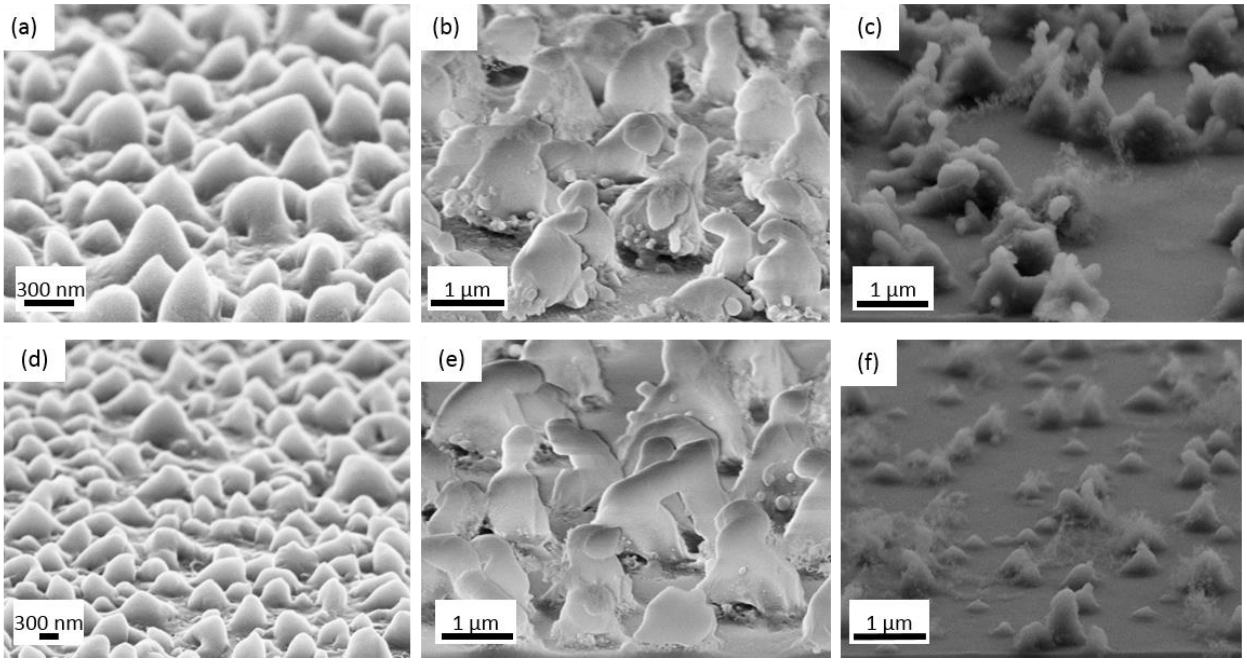

Figure 50: Comparison between SEM images of (a,d) gradually increasing the laser energy density from 45 mJ/cm^2 to 260 and 345 mJ/cm^2 in 40 seconds, respectively, (b,e) constant energy of 260 and 345 mJ/cm^2 in 25 seconds, respectively, and (c,f) constant energy of 260 and 345 mJ/cm^2 in 40 seconds, respectively.

To examine the optical properties of these nanostructured a-Si films, spectrophotometer analysis has been performed. A large, broadband increase in absorption has been detected for NCs compared to the reference bare a-Si film without any nanostructuring. The as-deposited 370 nm a-Si has two absorption peaks at 520 nm and 580 nm as shown in Figure 51(a). These peaks are attributed to the fabry perot resonances in the thin film. For wavelengths beyond 650, the bare a-Si layer has very low absorption of around 10%. At this small thickenss of a-Si, the losses at the long wavelength range become severe. Introducing the NCs on top of the a-Si resulted in a significant increase in absorption over the entire measured wavelength range as shown in Figure 51(a). Increasing E_{max} from 220 mJ/cm^2 to 260 mJ/cm^2 resulted in further increase in absorption. Further increase in E_{max} resulted in increasing the absorption in the short wavelength range while a slight decrease was observed at the long wavelength range. The randomness of the produced NCs offers a variety of diameters that yields to this broadband absorption enhancement.

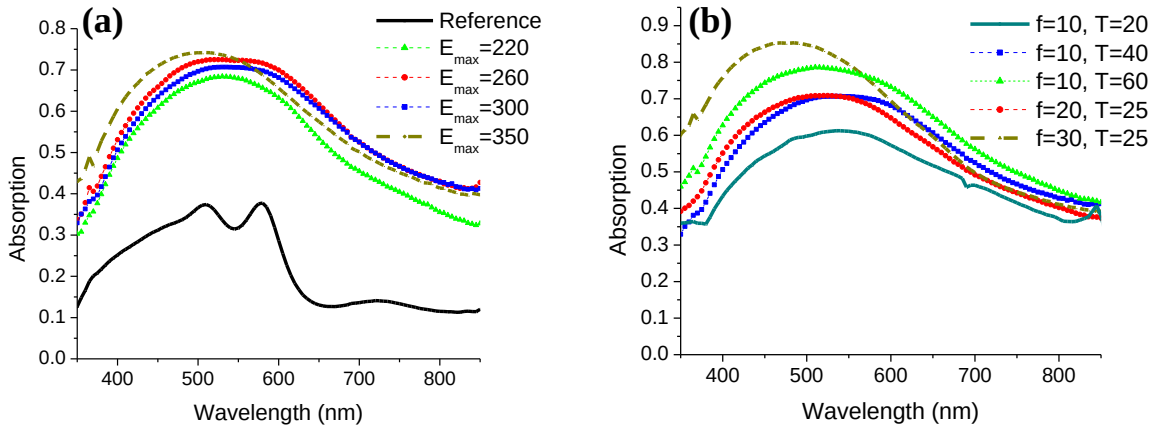

Figure 51: Absorption spectrum of a-Si irradiated by excimer laser with (a) different E_{max} while fixing f=10 Hz and T=40 s, and with (b) different frequencies and times while fixing E_{max}=300 mJ/cm^2.

In previous measurements, the energy was varied while keeping the time and frequency constant. Next, the effect of changing the time and frequency is studied while fixing E_{max} to 300 mJ/cm^2. Decreasing the time in which the energy is gradually increased to 300 mJ/cm^2, resulted in the formation of smaller NCs with average length of 230 nm and diameter of 290 nm as shown in Figure 52(a). In addition, the density of NCs are less compared to all other conditions with T=40 s. This indicates that the NCs continue to form throughout the time of increasing the energy not only at the beginning of laser pulses irradiation. For these reasons, this condition showed the least absorption as shown in Figure 51(b).

On the other hand, increasing the time to 60 s resulted in longer NCs with average length of 510 nm. However, the average diameter is only 415 nm. Hence, the structure in this case is different and has a length larger that the diameter. Figure 52(b) shows that this structure looks more like nanoparticles or extremely short nanowires.

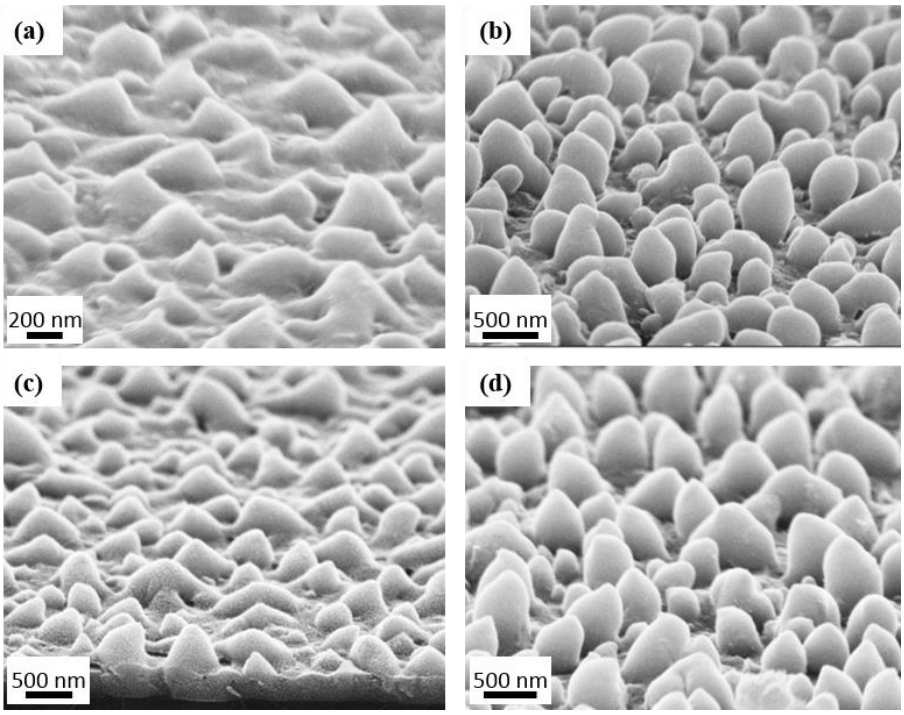

Figure 52: SEM images for NCs formed at fixed E_{max}=300 mJ/cm^2 and (a) T=20 s, f=10 Hz, (b) T=60 s, f=10 Hz, (c) T=25 s, f=20 Hz, and (d) T=25 s, f=30 Hz. All images are taken with 20^o tilt.

Regarding to varying the frequency, the frequency was increased to 20 and 30 Hz. For higher frequencies samples, the time was reduced to 25 s in order to prevent the formation of irregular shapes. Having a high frequency such as 30 Hz resulted in longer NCs, as shown in Figure 52(d), with average length of 545 nm and diameter of 465 nm. Here, longer NCs are obtained without causing irregular shapes as in the case of increasing the energy density. These long NCs resulted in the highest absorption especially in the short wavelength as shown in Figure 51(b) for the NCs formed with 30 Hz in 25 s. The slightly reduced absorption in the long wavelength range is maybe due to the more rounded tip of the NCs compared to the sharp tip obtained with other conditions. It could be concluded that increasing any of the laser parameters ($E_{max,}$ T, or f) increases the length the NCs. The length and diameter distribution for the samples where the time and frequency is varied were also calculated and shown in Figure 53.

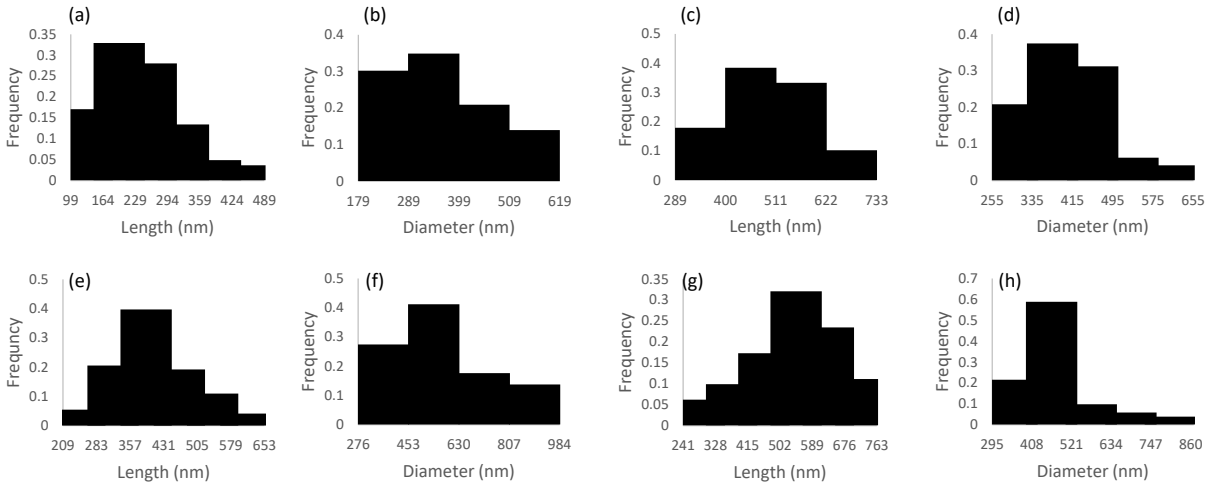

Figure 53: length and diameter distribution for for NCs formed at fixed E_{max}=300 mJ/cm^2 and (a,b) T=20 s, f=10 Hz, (c,d) T=60 s, f=10 Hz, (e,f) T=25 s, f=20 Hz, and (g,h) T=25 s, f=30 Hz, respectively.

The enhancement in absorption in calculated using the formula:

$$Enhancement\ factor(\%) = \frac{\mathrm{A}(\lambda) - \mathrm{A_{ref}}(\lambda)}{\mathrm{A_{ref}}(\lambda)}\ x100$$

where $\mathrm{A}(\lambda)$ is the absorption in a-Si after nanostructuring and $\mathrm{A_{ref}}(\lambda)$ is the absorption in the bare a-Si film. More than 100% enhancement in absorption is calculated over the whole measured wavelength range as shown in Figure 54 for NCs fabricated with E_{max}=350 mJ/cm^2, f=10 Hz, and T=40 s and NCs fabricated with for E_{max}=300 mJ/cm^2, f=30 Hz, and T=25 s. The NCs fabricated at 30 Hz shows higher enhancement factor in the short wavelength range. Up to 350% enhancement is obtained at the long wavelength range where the absorption in the bare a-Si layer were minimal due to the small thickness of the film.

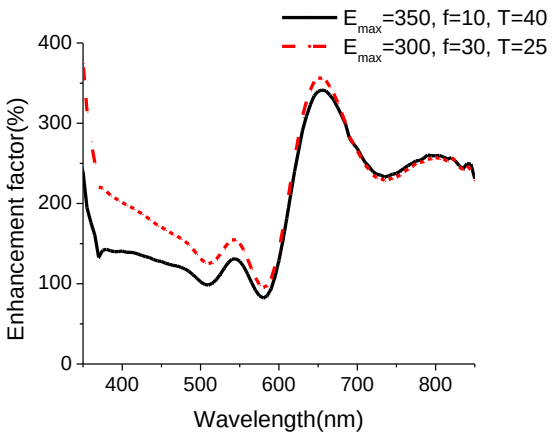

Figure 54: Enhancement factor for textured a-Si with (a) E_{max}=350 mJ/cm^2, f=10 Hz, and T=40 s, and (b) E_{max}=300 mJ/cm^2, f=30 Hz, and T=25 s.

The strong enhancement in light absorption is attributed to the reduced reflection of the textured a-Si layer compared to the flat one. Introducing a NC structure on top of the a-Si caused a gradual change in refractive index resulting in supressing the reflection. In addition, this surface texturing increase light scattering in the underneath a-Si layer resulting in increased light path length and thus increased absorption.

Another problem arises for many Silicon solar cells is the angle dependent absorption. Away from the oblique light incidence, the reflection starts to increase causing a reduced absorption in the solar cell. For the bare 370 nm a-Si layer, the refection at angles from 10^o to 60^o is shown in Figure 55(a). It could be seen that the two peaks found in the absorption corresponds to two dips in the reflection due to the Fabry Perot resonance in the thin film. Except at these two dips, the reflection in the whole wavelength range is above 30% and increases with increasing the angle of incidence. The proposed structure with NCs shows a much reduced reflection not exceeding 5% in the whole wavelength range for angle of incidences up to 40^o. At 50^o and 60^o, although the reflection slightly increases at longer wavelengths, it does not surpass 10% in all cases. This wide angle anti-reflective properties are essential in the new generation of thin film silicon solar cells and would play a significant role in the commercialization of such devices.

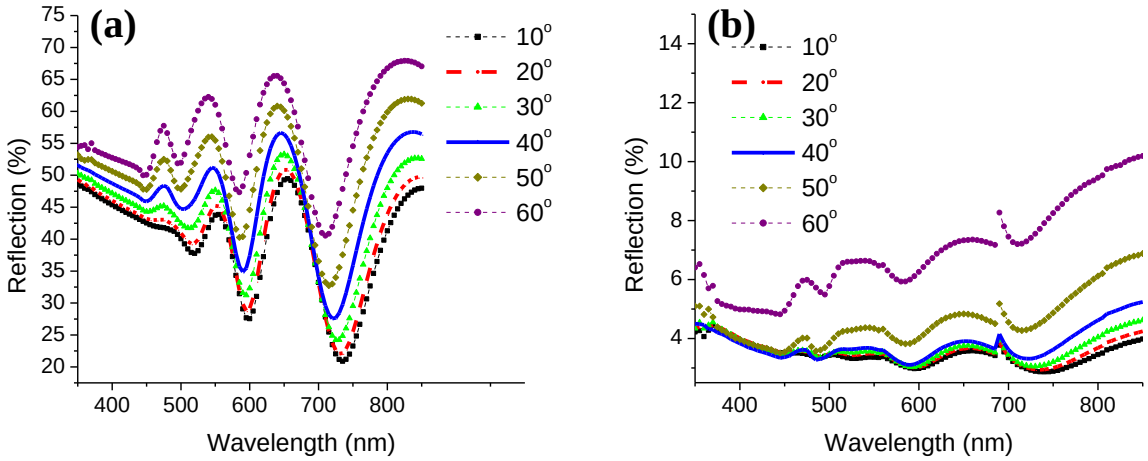

Figure 55: Reflection at angles from 10° to 60° for (a) bare a-Si and (b) textured a-Si with E_{max}=350 mJ/cm^2.

To gain further insight on the phenomena happening at each time interval while increasing the energy in 40 seconds, AFM is performed for 4 samples with gradually increasing the energy. The first sample had an energy density increasing from 45 to 130 mJ/cm^2 in 16 s [Figure 56(a)], the second one from 45 to 175 mJ/cm^2 in 24 seconds [Figure 56(b)], the third one from 45 to 215 mJ/cm^2 in 32 s [Figure 56(c)] and finally from 45 to 260 mJ/cm^2 in 60 s [Figure 56(d)]. In the first 16s, small NCs (i.e. 30 nm in length) are formed. Then, the length of NCs starts to increase in some areas in the sample reaching 120 nm as shown in Figure 56(b). Additional increase in length (i.e. 500 nm) is observed with additional increase in energy density and time. Further increase in energy density did not increase the length any further. However, more NCs were formed.

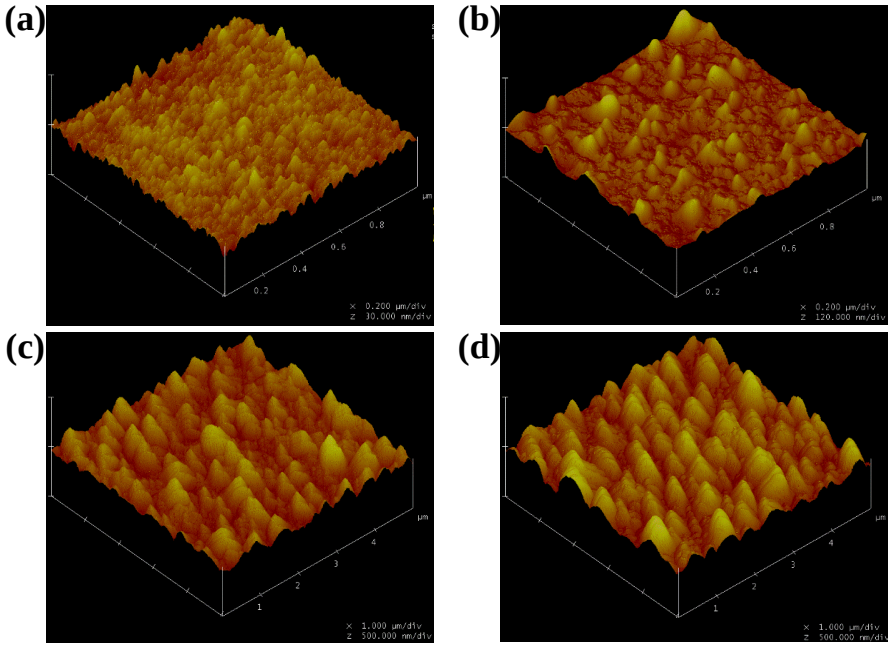

Figure 56: AFM images for each time interval for sample with E_{max} = 260 mJ/cm^2. The energy density was increased in (a) from 45 to 130 mJ/cm^2 in 16 s, (b) from 45 to 175 mJ/cm^2 in 24 seconds, (c) from 45 to 215 mJ/cm^2 in 32 s. and (d) from 45 to 260 mJ/cm^2 in 60 s.

Due to the lower thermal conductivity of silica substrate compared to Silicon, the absorbed heat due to laser irradiation is mainly dissipated laterally. The liquid silicon then moves in the direction that the melting/solidification front moves because liquid silicon (2.52 g/cm3) is denser than solid silicon (2.2 g/cm3 for a-Si). Thus, the thin film with a fixed mass expands to a greater volume pushing the liquid silicon toward the center and upward[165,166].The cone formation in this work could then be attributed to this lateral re-solidification where a mass transfer occurs[167,168].

4.2.3. Morphology and optical properties of Silicon nanowires

Silicon nanowires at atmospheric pressure

For first trials, the excimer laser was performed while the chamber was open. Thus, no reduced pressure was implemented and the irradiation occurred in air with atmospheric pressure. These samples were performed on 400 nm a-Si deposited on 2 µm SiO_2 with Silicon wafers as substrates. As in the case of forming Silicon NCs, the energy was gradually increased during irradiation from 45 mJ/cm^2 to a maximum energy in 40 seconds. Since the energy reaching the sample is higher in case of atmospheric pressure than in reduced pressure, a different structure was obtained. In addition, the open chamber also

reduced the losses resulting in a higher energy reaching the sample. Thus, instead of having the NCs reported in the previous section, a nanowire (NW) structure is obtained. The effect of changing the maximum energy density (E_{max}) on the fabricated NWs is shown in Figure 57. Figure 57(a to d) show the NWs formed with energy densities 215 $mJcm^{-2}$ to 565 $mJcm^{-2}$. It could be observed that as the E_{max} increases, the length and diameter of the NWs increases. For E_{max} = 215 mJ/cm^2, the average length of the wires was 750 nm with 450 nm average diameter. Increasing the E_{max} to 350 mJ/cm^2 increased the length to 1.5 μm and the diameter to 600 nm. At 435 mJ/cm^2, the length reached 2 μm with 750 nm diameter. Further increase in the energy caused the wires to bend and their overall length was decreased to 1.7 μm but the diameter was almost unchanged compared to the previous case.

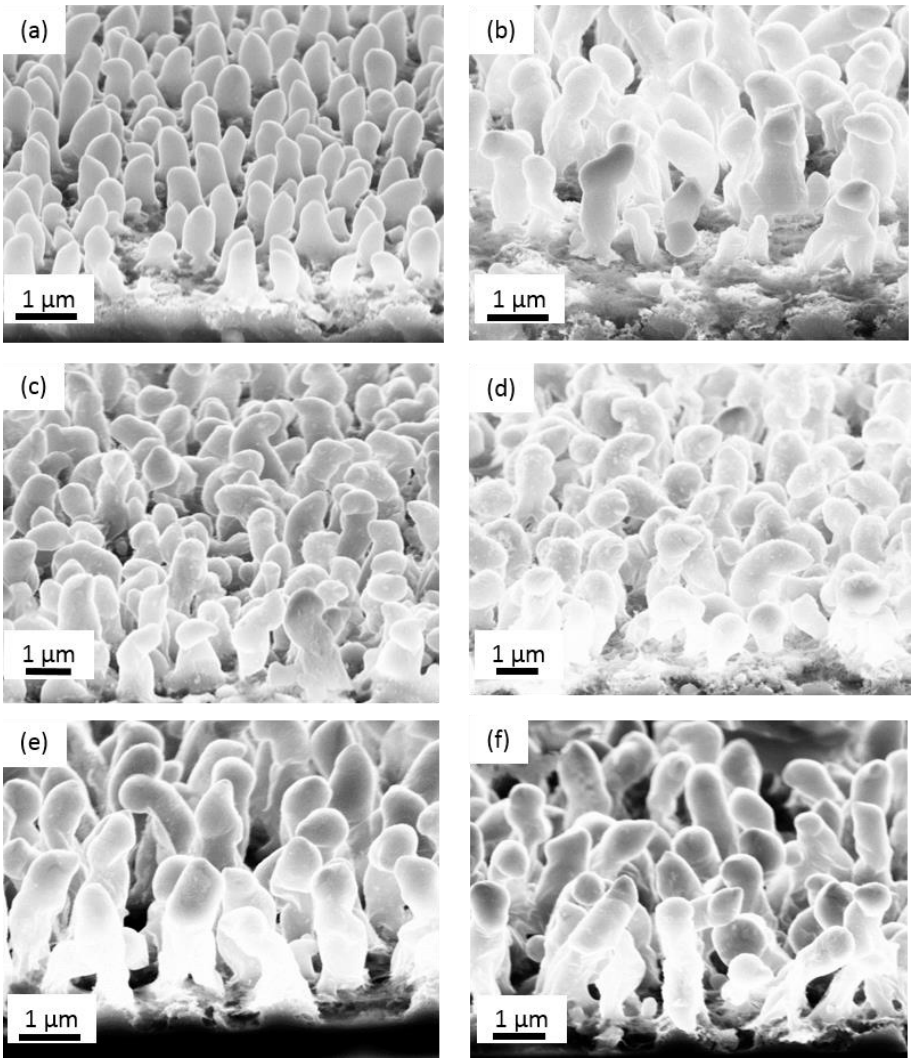

Figure 57: SEM images of Silicon NWs formed with maximum energy density (E_{max}) equals (a) 215 mJ/cm^2, (b) 350 mJ/cm^2, (c) 435 mJ/cm^2, (d) 565 mJ/cm^2, (e) 435 mJ/cm^2 with 100 additional pulses, and (f) 435 mJ/cm^2 with 200 additional pulses. All images are taken with 20^o tilt.

The effect of adding additional pulses at a constant energy after increasing the energy density from 45 mJ/cm^2 to E_{max} was also tried. Holding the energy at 435 mJ/cm^2 then adding 100 additional pulses caused an increase in the length to 2 µm and adding 200 additional pulses caused an increase to 2.5 µm. It could be noticed also that the roughness of the wires increase with increasing E_{max} or the number of additional pulses. Moreover, it could be seen in Figure 57 that the NWs formed in air are not perfectly vertical, some of them are bent and have irregularities along their length, especially at higher energies. In addition, the aspect ratio is small and there is little control over their dimensions. Decreasing the frequency to 5 Hz was also tried and no significant change in shape or dimension was observed.

Keeping the energy density constant during irradiation in air did not result in the formation of uniform wires, even if the energy is lower than the maximum energy reached in the previous case. This is probably because a-Si films were subjected to very high energy at once causing non-uniformities to occur. Figure 58 shows these observations. Figure 58 (a and b) show the wires formed at constant energy E= 130 and 175 mJ/cm^2, respectively. For these samples, the time of irradiation (t) was kept only 10 seconds. It could be seen that extremely short NWs were obtained with average length equals 150 nm for E= 130 mJ/cm^2. Increasing the energy to 175 mJ/cm^2 caused an increase in the length to 500 nm. However, the length was non-uniform throughout the sample.

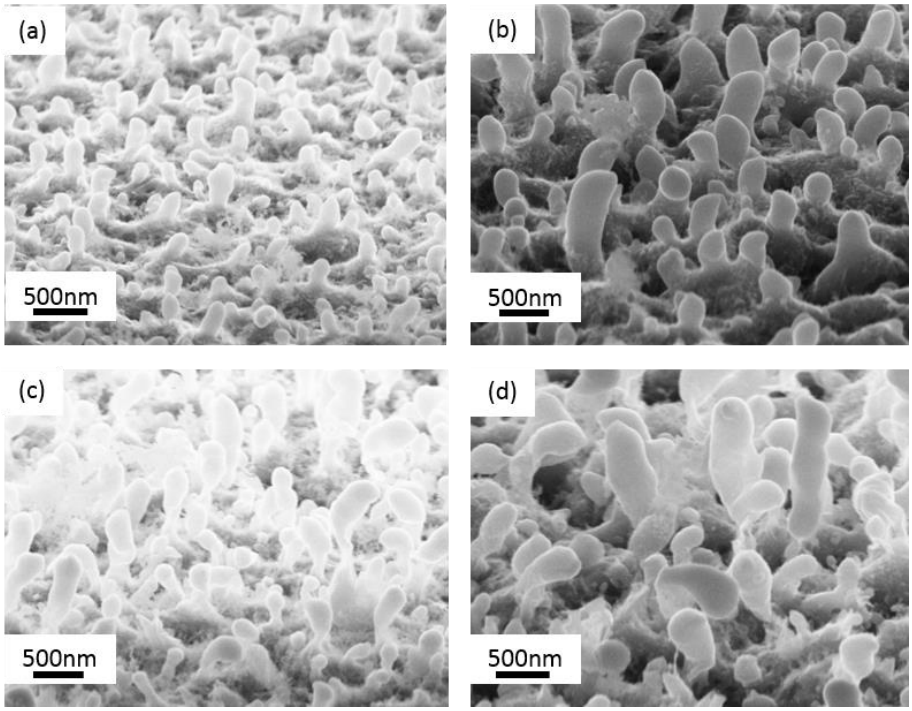

Figure 58: SEM images of Silicon NWs formed with constant energy density equals (a) E=130 mJ/cm^2 and t = 10 s, (b) E=175 mJ/cm^2 and t = 10 s, (c) E=130 mJ/cm^2 and t = 40 s, and (d) E=175 mJ/cm^2 and t = 40.

Similarly, increasing the time to 40 seconds while having a constant energy of 130 and 175 mJ/cm^2 resulted in a similar behavior as shown in Figure 58 (c and d), respectively. It could be seen the wires are bent and irregular and non-uniform lengths are obtained. Thus, in the next section, these NWs are formed in reduced pressure (i.e. 3.5 mbar) inside the chamber and the effects of changing the energy density, time, and frequency were studied. In addition, thicker a-Si films were deposited in order to give a chance to the deposited film to form well distributed nanowires. In the next section, all details

related to the new fabricated nanowires are given.

Silicon nanowires at reduced pressure

Silicon nanowires are fabricated by laser irradiation using nanosecond excimer laser. The energy density of the laser is fixed throughout the laser exposure time. Different energies, exposure times, and frequencies are studied in order to see their effect on the morphology of the fabricated NWs and to optimize the NWs to achieve the highest absorption in the visible range.

First, the frequency and exposure time are kept constant and the energy density was varied between 130 mJ/cm^2, 175 mJ/cm^2, 215 mJ/cm^2, 260 mJ/cm^2, 300 mJ/cm^2, and 350 mJ/cm^2. These energy densities are measured in air. The actual energy density reaching the sample is slightly less than these measured values due to the reduced pressure inside the chamber and the losses through the chamber glass window. The frequency (f) was initially set to 10 Hz and exposure time (t) was 40 seconds. Figure 59 shows the obtained NWs for different energy densities. At small energy density, 130 mJ/cm^2, small NWs were obtained with the average length (~190 nm) almost equals the average diameter. This gave some of them a nanoparticle-like structure as shown in Figure 59(a and b). Increasing the energy density to 175 mJ/cm^2, caused an increase in the average length (~720 nm) and the diameter (~320 nm) of the NW. It could be seen in Figure 59(c and d) for 175 mJ/cm^2 that some of the NWs grow with a rate higher than others. This could be observed because very small nanoparticles are still present in the sample while the length of other NWs reached 720 nm.

Further increase in energy to 215 mJ/cm^2 and 260 mJ/cm^2 caused a further increase in both the diameter and the length of the NW. Figure 59(e and f) and Figure 59(g and h) show the NWs formed with energy density equals 215 mJ/cm^2 and 260 mJ/cm^2, respectively, and it could be seen that a more uniform distribution in the NWs length is obtained with an average length of 1.62 μm and 1.8 μm, respectively. This length is larger than the thickness of the deposited a-Si layer (i.e. ~800 nm) indicating that the NWs are formed by re-distributing the mass within the sample and not by etching some the Silicon material. Any additional increase in energy caused the NWs to have irregular shapes. This is probably because the deposited material was already consumed and the added energy caused the

remaining residues of the material to re-deposit on the base of the NWs only forming these irregular shapes as shown in Figure 60(a and b) for energy density equals 300 mJ/cm^2 and 300 mJ/cm^2, respectively.

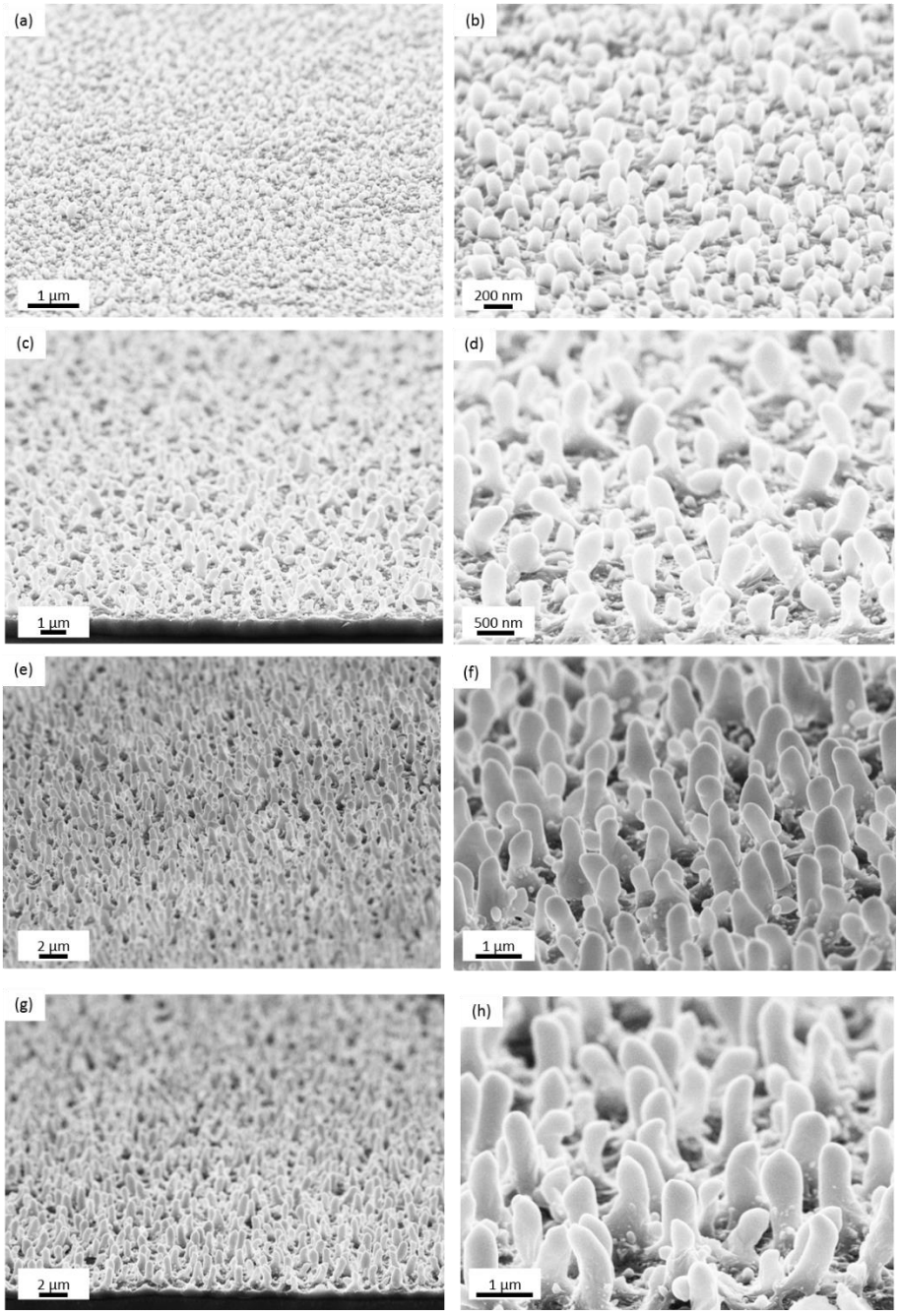

Figure 59: SEM images of Silicon NWs formed with energy density equals (a,b) 130 mJ/cm^2, (c,d) 175 mJ/cm^2, (e,f) 215 mJ/cm^2, and (g,h) 260 mJ/cm^2. All images are taken with 20^o tilt.

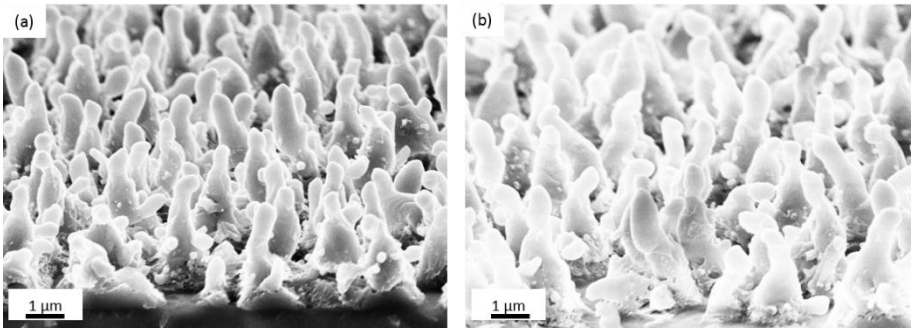

Figure 60: SEM images of Silicon NWs formed with energy density equals (a) 300 mJ/cm², and (b) 350 mJ/cm². All images are taken with 20° tilt.

To summarize the effect of changing the energy density on the morphology of the obtained NWs, the distribution of lengths and diameters for each energy density in each sample was calculated. Figure 61 shows the length and diameter distribution for all fabricated nanowires. Their averages were extracted and plotted in Figure 62. Changing the energy density from 130 mJ/cm^2 to 215 mJ/cm^2 increased the average length from ~200 nm to ~1.7 µm. A rapid increase in length was observed at lower energy densities (i.e. from 130 mJ/cm^2 to 215 mJ/cm^2). Increasing the energy from 215 mJ/cm^2 to 260 mJ/cm^2 showed only a slight increase in length from 1.6 µm to 1.7 µm. On the other hand, only a small increase in diameter from ~120 nm to ~530 nm is observed for increasing the energy. As the energy increases, more material is transferred from the edges to the middle forming NWs with increased length.

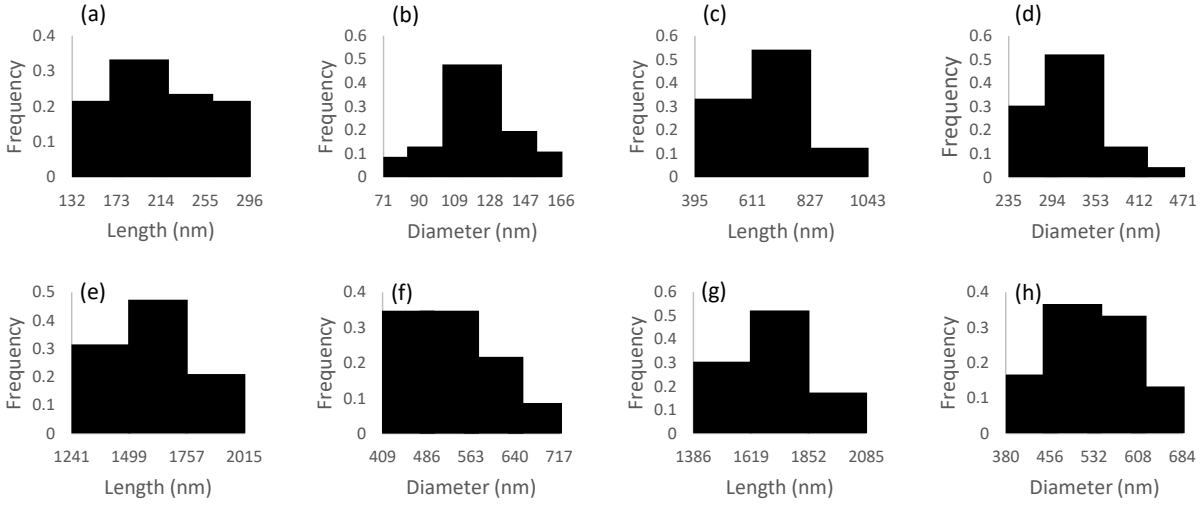

Figure 61: length and diameter distribution for NWs formed at fixed (a,b) E_{max}=130 mJ/cm², (c,d) E_{max}=175 mJ/cm², (e,f) E_{max}=215 mJ/cm², and (g,h) E_{max}=260 mJ/cm², respectively.

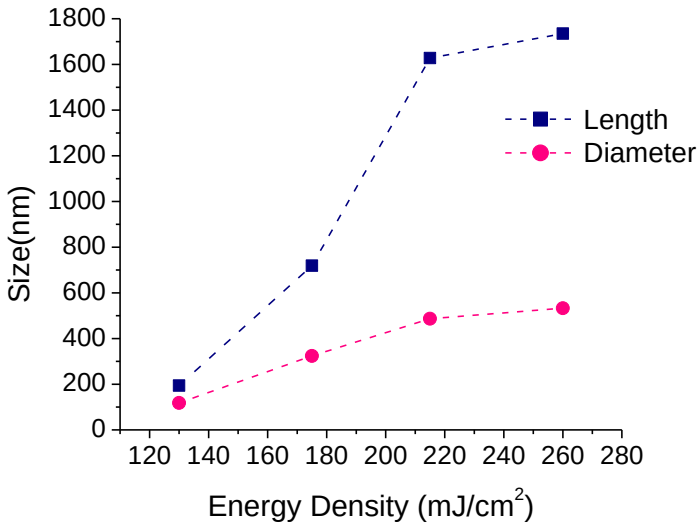

Figure 62: Average size (i.e. length and diameter) for NWs formed using excimer laser with different energy density and fixed frequency (10 Hz) and exposure time (40 s).

In the previous measurements, the frequency and time were fixed for all samples. Next, the effect of changing the laser exposure time (t) and frequency (f) is studied. A fixed energy density of 215 mJ/cm^2 was set while the exposure time is changed from 20 seconds to 70 seconds. Similar to increasing the energy, increasing the time increased the length of the NWs as shown in Figure 63(a to e) for t = 20 to 70 seconds, respectively. This could be expected, as the sample is exposed for more time to laser energy, more material is transferred forming longer NWs. The average length and diameter distributions for these samples were also calculated and plotted in Figure 64. The effect of increasing the time on the length of the NWs was not as strong as increasing the energy as could be seen in the blue square line in Figure 65. In addition, changing the exposure time had almost no effect in changing the NW diameter (pink circle line in Figure 65).

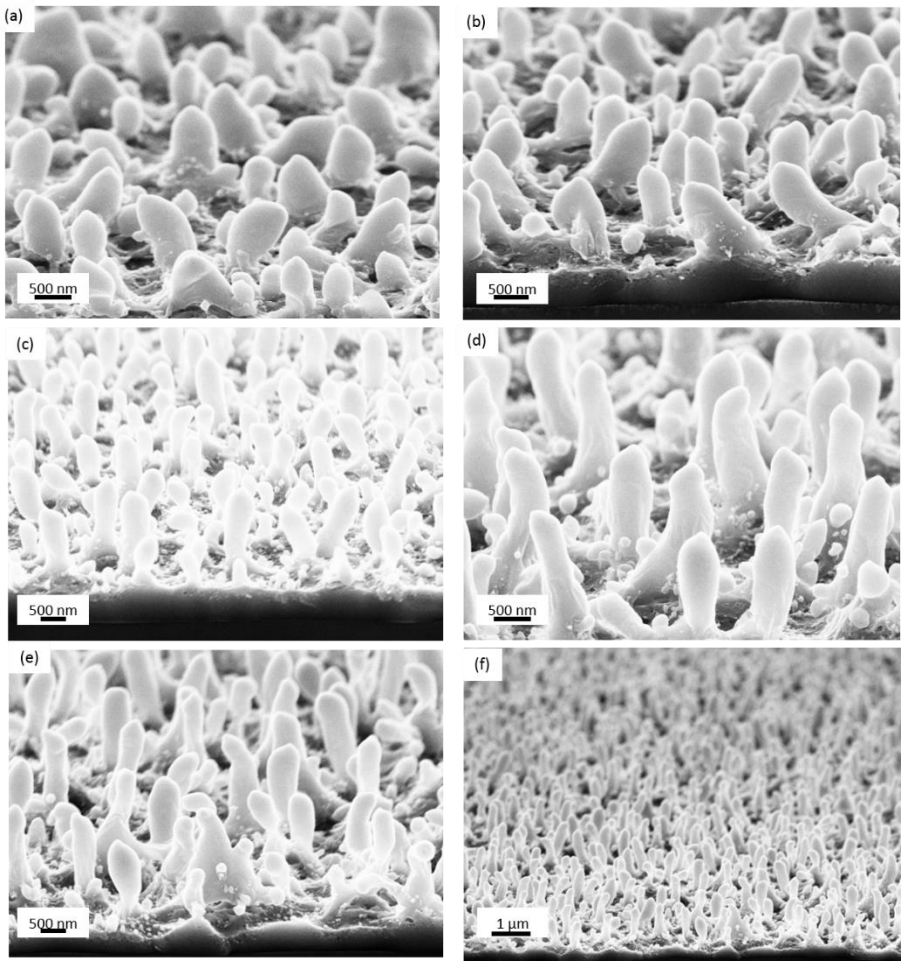

Figure 63: SEM of NWs fabricated with fixed laser energy equals 215 mJ/cm^2 and frequency equals 10 Hz and time equals (a) 20 s, (b) 30 s, (c) 50 s, (d) 60 s, and (e,f) 70 s. All images are taken with 20^o tilt.

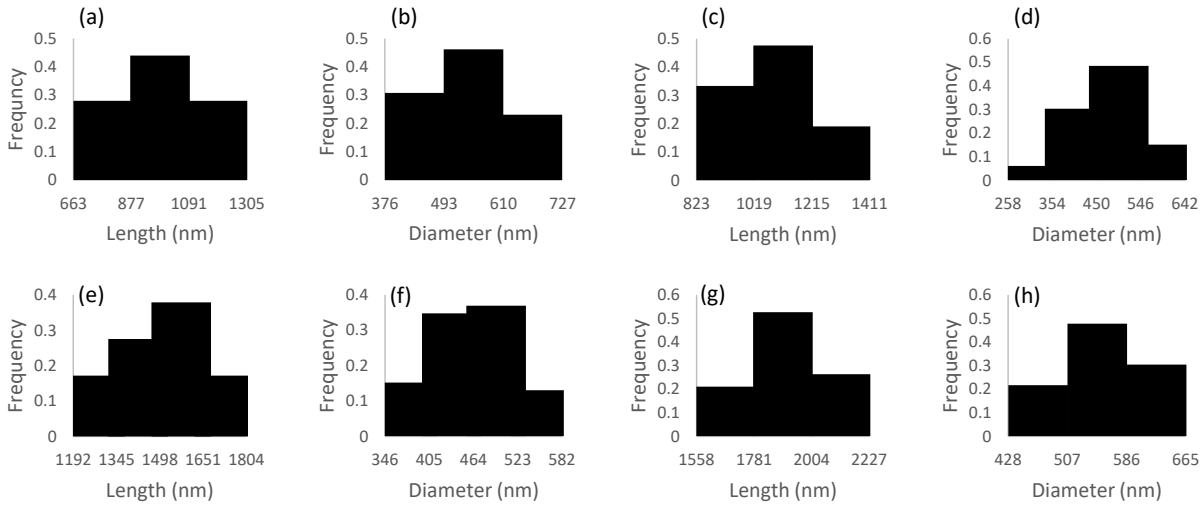

Figure 64: length and diameter distribution for NWs formed with fixed laser energy equals 215 mJ/cm^2 and frequency equals 10 Hz and time equals (a,b) 20 s, (c,d) 30 s, (e,f) 50 s, and (g,h) 60 s, respectively.

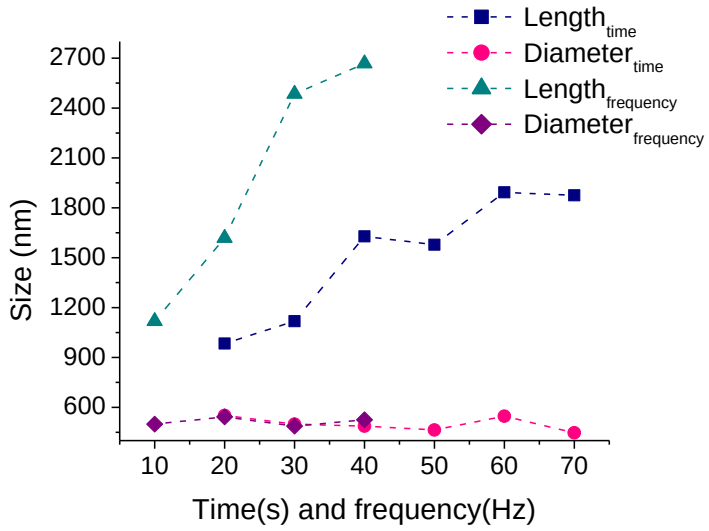

Figure 65: Average size for NWs formed with fixed energy density (215 mJ/cm^2). Green and purple lines are for different frequencies and fixed exposure time fixed to 40 s. Blue and pink lines are for different exposure time and fixed frequency equals 10 Hz.

Increasing the frequency had a significant effect on increasing the length of the NWs. lengths up to 2.7 µm is reached without forming any irregular shapes. This length is more than triple the thickness of the originally deposited a-Si film. Figure 66(a,b), Figure 66(c,d), and Figure 66(e,f) show the NWs fabricated with 20, 30 and 40 Hz, respectively. It could be seen that as the frequency increases, the length of the NW increases. Increasing the frequency had almost no effect on changing the diameter.

This could be seen in Figure 65 where the effects of increasing the frequency on the average length and diameter of the formed NWs are summarized after extracting these averages from the distribution calculations in Figure 67. At 40 Hz, the longer NWs reported in this work in obtained with 2.7 μm length and ~500 nm diameter.

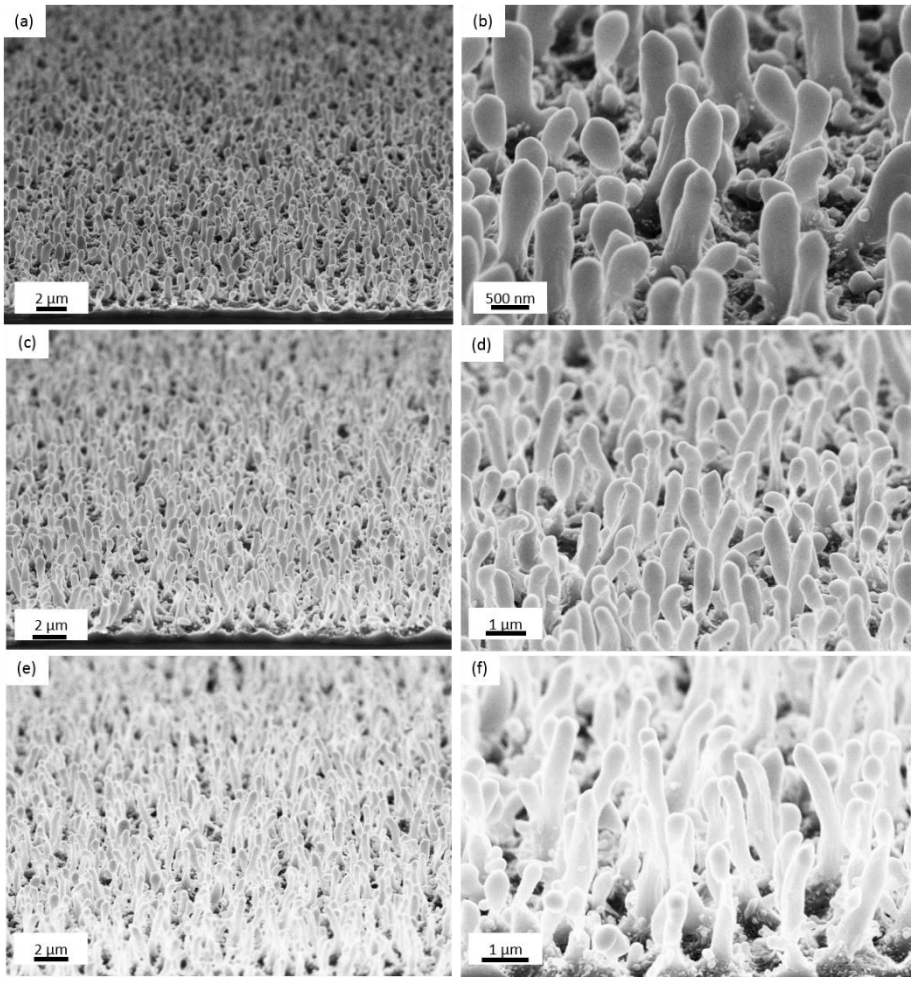

Figure 66: SEM of NWs fabricated with fixed laser energy equals 215 mJ/cm^2 and exposure time equals 30 seconds and frequency equals (a,b) 20 Hz, (c,d) 30 Hz, and (e,f) 40 Hz. All images are taken with 20^o tilt.

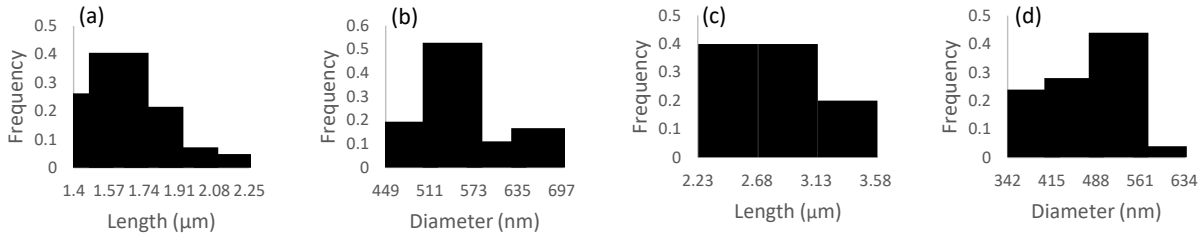

Figure 67: length and diameter distribution for NWs formed with fixed laser energy equals 215 mJ/cm^2 and exposure time equals 30 seconds and frequency equals (a,b) 20 Hz, and (c,d) 40 Hz, respectively.

Next, the optical properties of the fabricated NWs are analyzed. The effects of changing each laser parameter on the absorption of NWs are investigated. The absorption of the bare 820 nm a-Si layer is shown in Figure 68 (the black solid line). The peaks observed in the absorption is due to Fabry Perot resonances in the thin film. A significant part of the solar spectrum is lost due the mismatch between the refractive index of a-Si and air. In addition, at this small thickness, losses due to light transmission is observed especially in the long wavelength range. Forming the NWs caused a significant increase in absorption for all energy densities used. As the energy density increases, the absorption increases due to obtaining longer NWs which increases the light path length inside the a-Si. The increase in absorption is observed in the whole visible and near infrared wavelength range. The highest absorption is observed for E=260 mJ/cm^2 as shown in Figure 68.

.

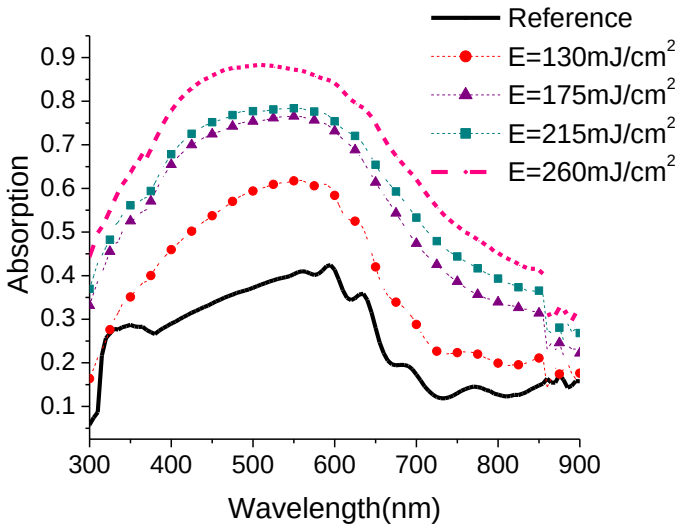

Figure 68: Absorption of NWs obtained with different energies, fixed frequency (10 Hz), and exposure time (40 s).

Changing the exposure time from 20 to 70 seconds had a small effect of increasing the absorption. Figure 69 shows the absorption for the NWs formed at different exposure times. Slight increase in absorption for each 10 seconds increase is observed due to obtaining longer NWs. almost no change is observed between exposure time equals 50, 60 and 70 seconds especially in the long wavelength range. Alternatively, increasing the frequency caused an enhancement in the absorption along the whole

wavelength range as shown in Figure 70. At 40 Hz, the absorption reached more than 90% between λ=400nm and λ=600nm compared to absorption less than 50% for bare a-Si film. As mentioned previously, the longest NWs reported here are obtained for the samples irradiated with 40 Hz frequency. This explains the higher absorption obtained for this condition. As the path length inside the Silicon increases, the overall absorption increases. Additionally, since the NW diameter almost does not change with increasing the frequency, the increased aspect ratio obtained due to the increased length results in better absorption in the short wavelength range[53].

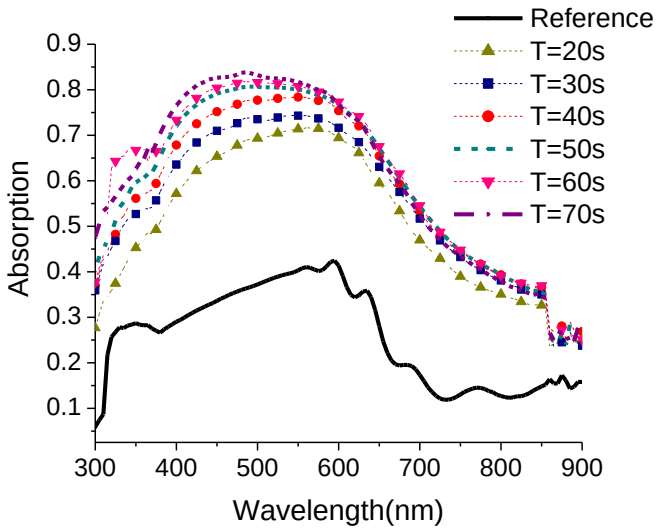

Figure 69: Absorption of NWs obtained with different times, fixed energy (215 mJ/cm^2), and frequency (10 Hz).

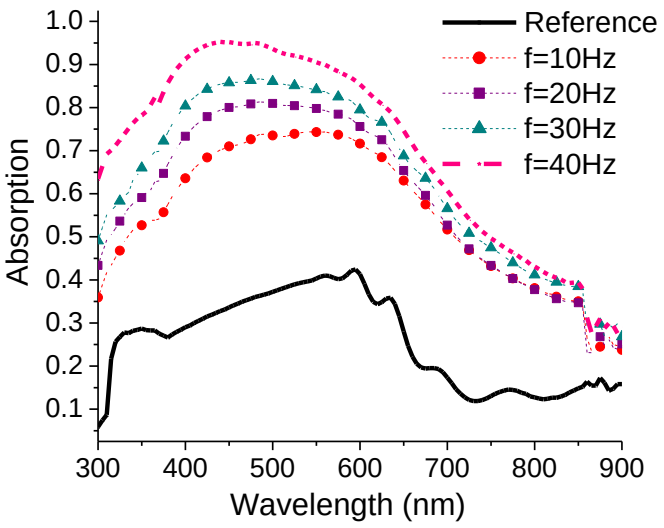

Figure 70: Absorption of NWs obtained with different frequencies, fixed energy (215 mJ/cm^2), and exposure time (30 s).

Obtaining Silicon NWs with lengths more than the deposited a-Si thickness caused an increase in the light path length inside the material. This increase in absorption is not expected to sacrifice the electrical properties due to the decoupling of the absorption direction and the charge collection direction in the NWs configuration. Thus, this increase in absorption is expected to be reflected in the power conversion efficiencies achieving enhanced overall efficiency. In addition, the enhanced matching between the refractive index in air and Silicon due to the graded change in refractive index had a huge effect on decreasing the reflection, and thus enhancing the absorption inside the Silicon. Figure 71(a) shows the reflection of bare deposited a-Si layer for different angle of incidences. The reflection is above 30% in most of the measured wavelength range and increases to more than 50% for larger angle of incidences. This means that a large portion of the incident solar spectrum is lost due to reflection. The dips in reflection observed in Figure 71(a) corresponds to the Fabry Perot resonance peaks found in absorption of bare a-Si layer in Figure 68. The reflection at different angle of incidences is measured for the highest absorbing NWs fabricated at f=40 Hz. Less than 3% reflection across the whole measured wavelength range is detected for angle of incidences up to 50°. For 60°, the reflection slightly increased at the long wavelength range only and was still less than 4%. This extremely low reflection is a major reason behind the enhanced absorption inside the Silicon.

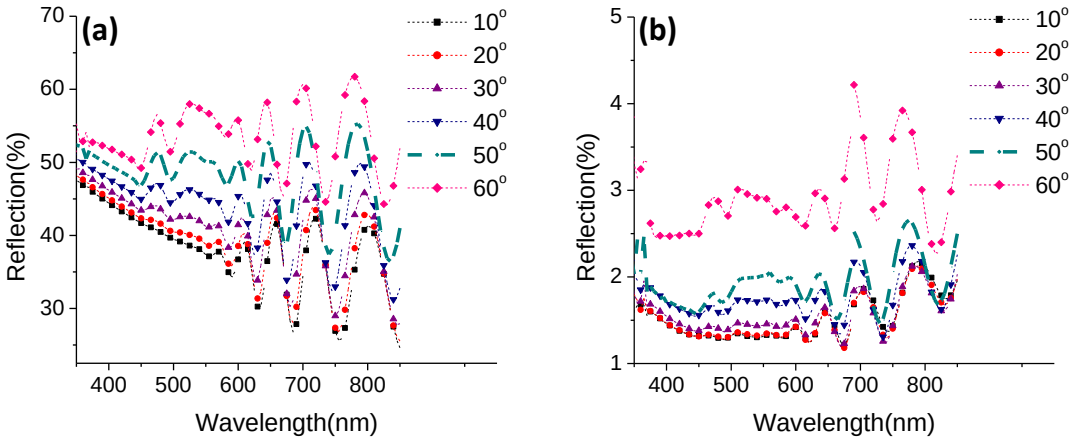

Figure 71: Reflection of (a) bare a-Si layer, and (b) fabricated NWs using the excimer laser with energy density=215 mJ/cm^2, f=40 Hz, and exposure time=30 s

Having this extremely suppressed reflection would result in almost unity absorption if no transmission is present. This indicates that a portion of the incident solar spectrum is lost in transmission. The samples made in this work is deposited on glass for demonstration purposes. However, having a metal back reflector or plasmonic gratings at the back of the solar cell will significantly increase the transmission and scatter back the remaining light. This will further increase the absorption inside the NWs achieving higher overall efficiency[169]. Another advantage of NWs fabricated using this method is that they are not agglomerated together similar to NWs fabricated using metal assisted chemical etching methods[162]. This will make them suitable for hybrid solar cells where a conformal layer of polymer could be coated on it giving a clear interface between the Silicon and the polymer which will enhance the optical and electrical properties[170,95,97].

4.3.Double light trapping configuration for amorphous Silicon solar cells

High efficient crystalline silicon (c-Si) solar cells efficiencies are getting close to the Shockley Queisser limit. The Shockley Queisser limit is the maximum theoretical efficiency that could be achieved using single junction solar cell. c-Si has the advantage of having high diffusion length of few tens of micrometer[39]. Solar cells of such thickness could absorb most of the incident photons. However, the high cost of fabrication of these highly purified c-Si and the high required energy to make them strict the large spreading of these devices to dominate the energy market. These limitations highly

motivate the research to shift to other types of silicon where the quality is not as pure as c-Si such as amorphous or nano-crystalline silicon. However, these less purified types of silicon suffer from low diffusion length due to the randomness of the crystal structure[39]. This small diffusion length restricts the thickness of the silicon layer to few tens of nanometre in order to be able to collect the photo-generated electrons before recombination. Thus, these devices suffer from low absorption efficiency. This is where light trapping techniques play a major role.

Photon management and light trapping in this film solar cells, such as a-Si, play an important role in increasing the overall efficiency in these devices[26,152,39,38,41,40]. Increasing the optical thickness of the device without increasing its physical thickness will enhance the absorption efficiency without sacrificing the electrical properties. Light trapping techniques in silicon solar cells take several shapes such as periodic gratings, back reflectors, plasmonic metallic nanostructures, periodic and random texturing, and anti-reflection coatings[20,26,44,47,152,46,39,38,41,40,171,60,42]. The usage of plasmonic nanostructures could be through the addition of metallic gratings to excite surface plasmon polaritons (SPP) or metal nanoparticles to excite localized surface plasmons (LSP). The addition of these plasmonic nanostructures proved to be an efficient way to enhance the coupling between the incident sunlight and the thin active layer[26,39,41,40]. However, the absorption enhancement achieved due to the addition of plasmonic nanostructure usually happens at a specific wavelength.[39,38] Furthermore, reflection losses from the surface of bare silicon is a major contributor in limiting the number of photons reaching the device[20]. Thus, it places additional limitation to the optical efficiency of the solar cell.

Here, we numerically propose a structure that achieves a broadband absorption enhancement in thin film a-Si solar cells. The structure is shown in Figure 73. Amorphous silicon layer is deposited on a 100 nm Au back electrode. Au gratings are added to the back electrode to localize light inside the a-Si layer by exciting surface plasmon polaritons (SPP) waves and increase the light path length. Many of the previous work associated with metallic gratings involve the addition of the gratings on top of the active layer[39,41,40]. This prevents a significant amount of the incident photons from reaching the active layer. It was reported previously that the addition of Au gratings on top of a-Si resulted in negative gain in absorption[39]. Here, placing the Au gratings underneath the a-Si achieved a positive gain in absorption.

In addition, surface texturing in the form of nanocones (NCs) are implemented on top of the a-Si layer to reduce the reflection and increase the scattering inside the underneath a-Si layer. This sandwiching of the a-Si layer between two light trapping configurations achieves a broadband absorption enhancement in the device.

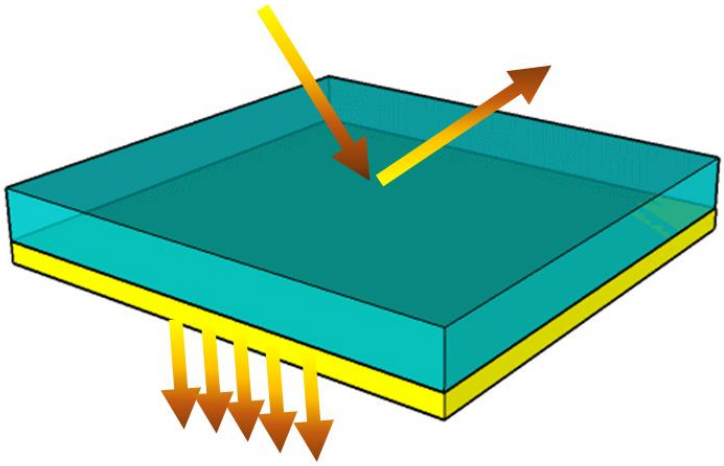

Figure 72: 3D schematic of a-Si film deposited on metal layer. The schematic shows the two major problem for a-Si thin film solar cell: the high reflection from flat surface due to variation in refractive index and transmission due to extremely thin layer.

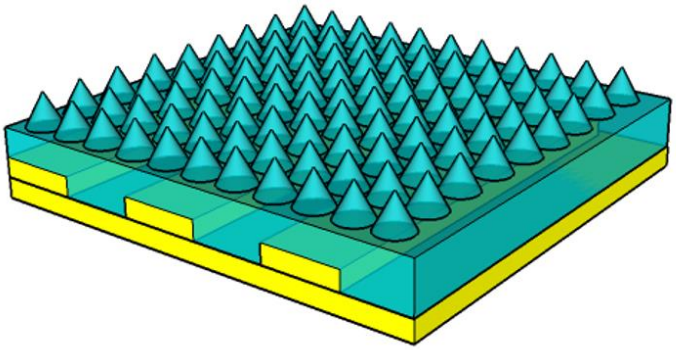

Figure 73: Schematic of the proposed structure showing texturing on top in the form of nanocones to reduce the reflection and metal gratings at the bottom to reduce the transmission

4.3.1. Optical simulations of amorphous silicon solar cells with periodic gratings

Simulation details

Three dimensional finite difference time domain (3D FDTD) simulations have been performed to analyse the proposed structure. Due to the periodicity of the device, only one period was simulated and the lateral boundaries were set to periodic boundaries while the vertical ones were set to perfectly

matched layers (PML). The reference device consists of the bare a-Si layer on top of a Au metallic film. A plane wave source is used to simulate the solar input. The whole simulation region of the reference device is shown in Figure 74. The thickness of the Au film is set to 100 nm in all simulations. The thickness of the a-Si film is varied in the optimization part.

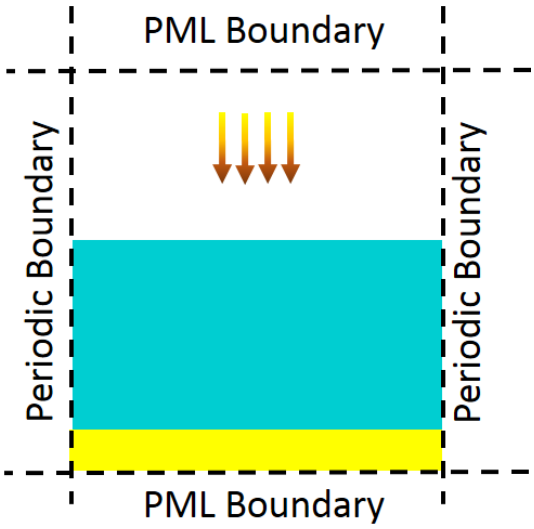

Figure 74: Schematic showing the simulation region for the reference solar cell: a bare a-Si thin film solar cell deposited on Au metal without any nanostructuring.

First, the Au nanogratings (NGs) only were added underneath the a-Si layer and optimized. The optimization accounted for all the geometric parameters involved in the design. More details about optimization is given in the subsequent sections. They were added to the device by adding a strip of Au in the middle of the simulation region in the x axis with a length taking the whole y as shown in Figure 75. The NGs are made Au and they are described by their width (W), height (H), and period (P). These parameters are shown in Figure 76.

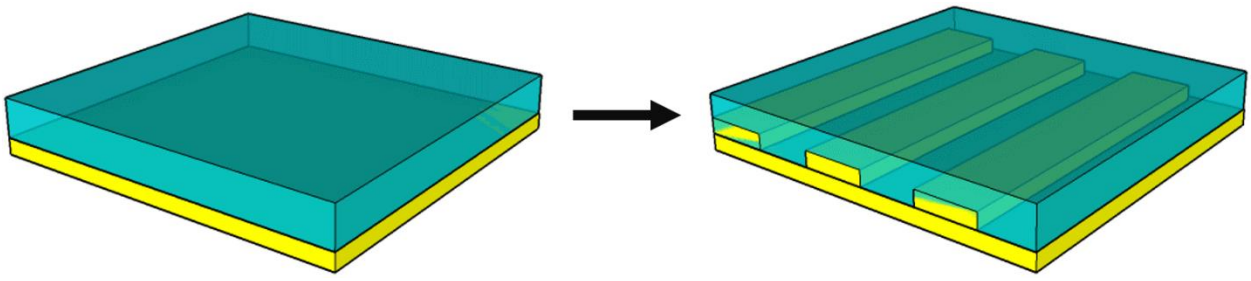

Figure 75: Schematic showing the addition of Au nanogratings only in the device.

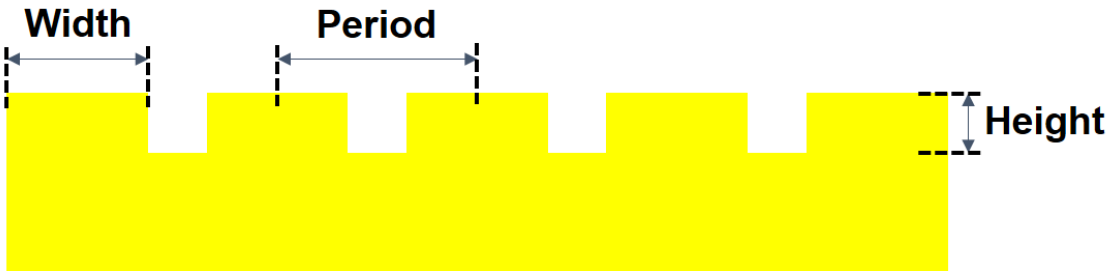

Figure 76: Schematic of the Au nanogratings showing all its parameters: width, period, and height of the gratings.

All other the parameters in the simulation region was unchanged (i.e. lateral boundary conditions, vertical boundary conditions, and light source location) as shown in Figure 77. Both TE and TM polarized light are simulated and averaged to account for the unpolarized nature of sunlight.

The absorption is measured with the same technique for all structures. This technique includes the addition of a power a monitor that surrounds the whole a-Si layer in addition to an index monitor overlapping with the power monitor. The index monitor is added to differentiate between the refractive index of a-Si and the refractive index of Au to differentiate between their absorptions using post scripting. Thus, all the absorption measured in this chapter is attributed to a-Si only excluding any absorption from Au gratings. Then, the absorbed power, short circuit current and the enhancement percentage in both are measured using the same equations stated in Chapter 2.

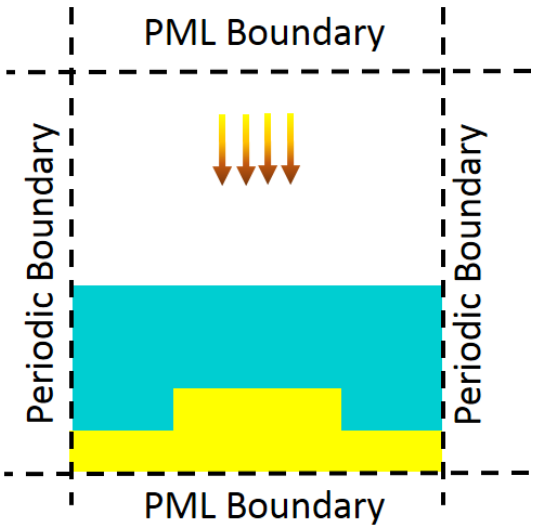

Figure 77: Schematic showing the simulation region for the solar cell with Au nanogratings only.

Optimization and results

To begin with, enhancement maps were calculated to obtain the optimum geometrical parameters for the NGs that achieve the highest absorbed power by tuning the light trapping properties in the visible range. These enhancement maps were calculated by measuring the enhancement factor in absorbed power for each simulated case. The enhancement factor in absorbed power is the ratio between the absorbed powers of the solar cell with the nanogratings to the one of a reference solar cell without the nanogratings. Initially, the a-Si thickness was fixed to 300 nm. The enhancement maps for the height of the NGs versus the period are calculated for several NG widths from 50 nm to 300 nm. These enhancement maps are calculated for TE and TM polarized light separately and the averaged to account for the unpolarised nature of light. Figure 78(a-f) show all these enhancement maps for widths= 50 nm, 100 nm, 150 nm, 200 nm, 250 nm, and 300 nm respectively. The First column on the left shows the enhancement maps for TE polarized light, the middle column shows the TM polarized light, and the right column shows the average between them. The highest enhancement factor is extracted from those enhancement maps and found at W = 300 nm, H = 50 nm, and P = 600 nm and marked with a white square in Figure 78(f).

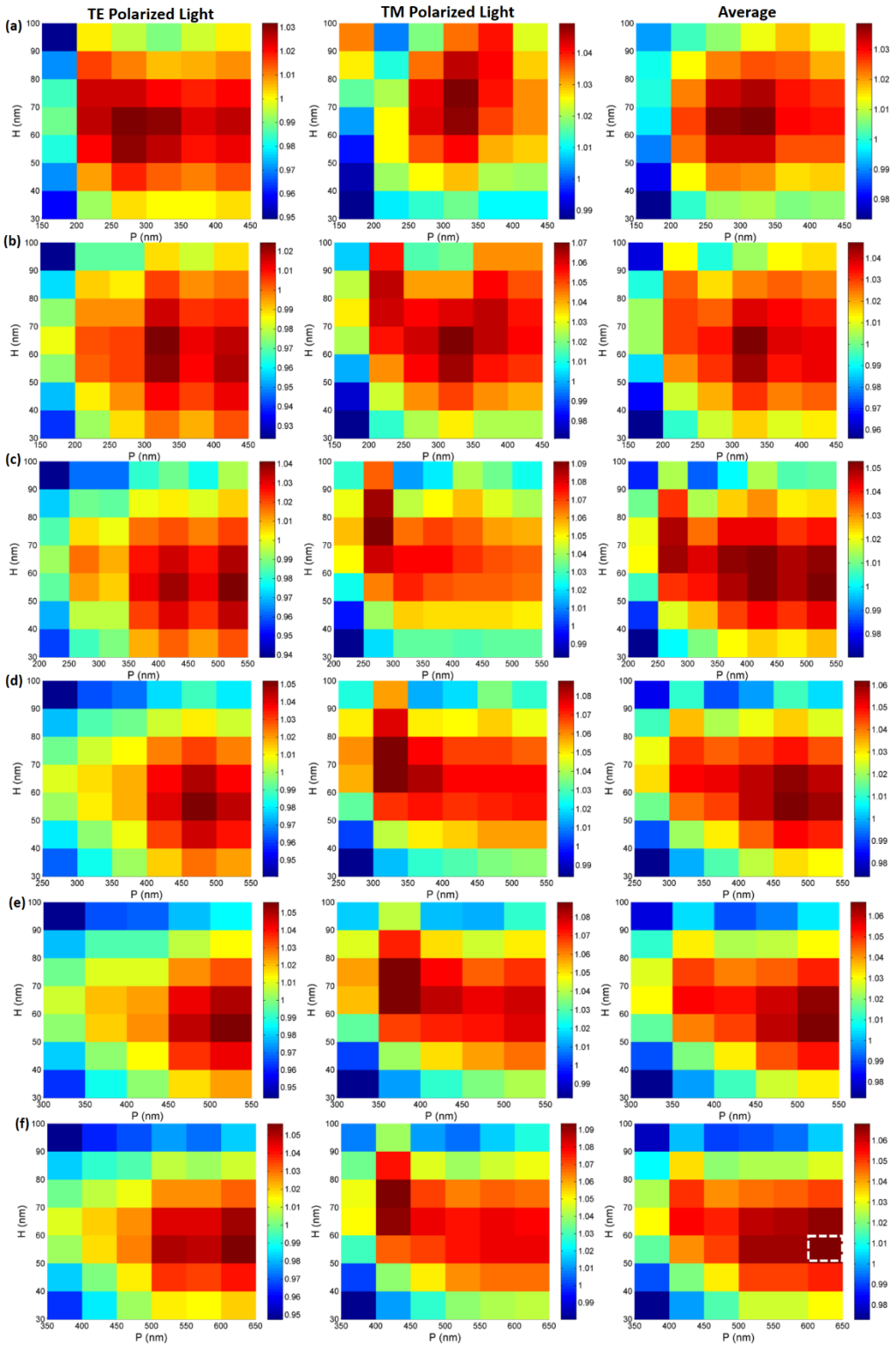

Figure 78: Enhancement map to optimize the NGs geometrical parameters. These enhancement maps are calculated for the height (H) versus the period (P) of the NGs for (a) W = 50 nm, (b) W = 100 nm, (c) W = 150 nm, (d) W = 200 nm, (e) W = 250 nm, and (f) E=300 nm. The First column on the left shows the enhancement maps for TE polarized light, the middle column shows the TM polarized light, and the right column shows the

average between them. The parameters showing the highest enhancement factor are marked with white circle light in (f).

The next step in the optimization is to know the optimum a-Si film thickness that achieves the optimum light trapping. Thus, a-Si thickness was varied from 60 nm to 300 nm and the enhancement factor was calculated for each case. Figure 79(a and b) shows the enhancement factor as a function of a-Si film thickness for absorbed power (AP) and short circuit current (J_{sc}), respectively. A modulation pattern could be observed and the enhancement factor increases at certain a-Si film thicknesses while it decreases at others. This is attributed to the cavity resonance in the a-Si thin film. The addition of the Au gratings changes the effective thickness of the layer. When the thickness and the incident wavelength satisfy the resonance condition, a high enhancement factor is obtained while at other thicknesses, a low enhancement factor is calculated. In addition, it was found that the modulation depth decreases with increases a-Si thickness and the enhancement factor is higher for thinner a-Si layers. This is because the reference absorption of the bare a-Si solar cell (i.e. without the NGs) is already large for larger thicknesses. Thus, the highest enhancement factor of ~1.25 was found for the 60 and 80 nm a-Si thick solar cell. To visualize this calculated enhancement, the absorption inside the a-Si is plotted.

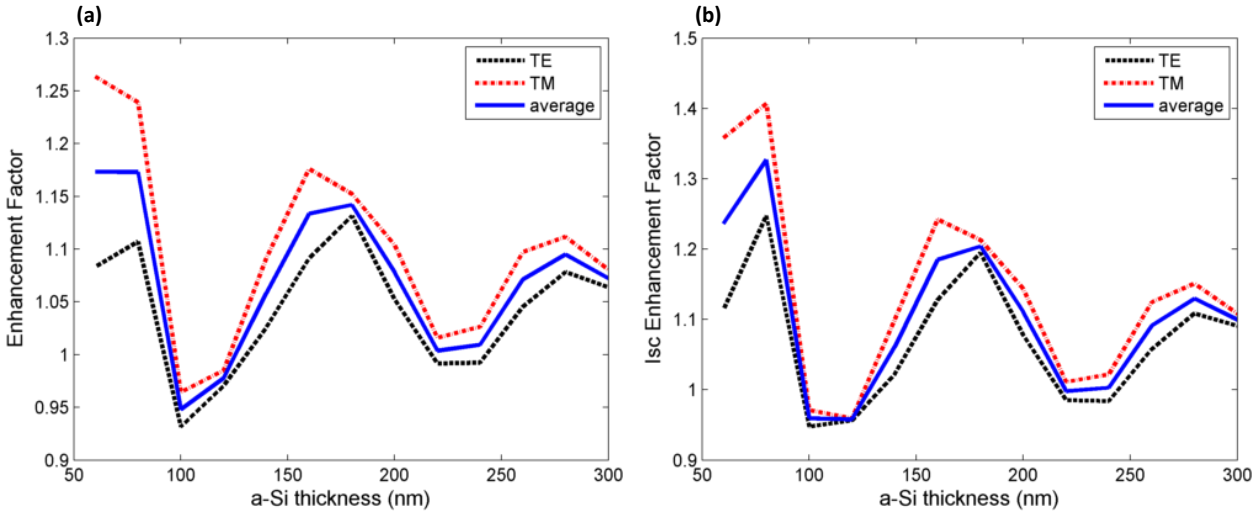

Figure 79: (a) Absorbed power enhancement factor and (b) short circuit current enhancement factor for different a-Si film thicknesses and the optimized grating parameters.

After the a-Si solar cell with the NGs was thoroughly optimized, the absorption inside the a-Si layer was then calculated for the solar cell with the optimized parameters. A thickness of 80 nm for a-Si thin

film as taken into consideration as it shows the highest enhancement for AP and J_{sc}. Figure 80(a) shows the absorption of the reference solar cell, the solar cell with NGs for TE and TM polarized light. It could be seen that the reference absorption has a major peak around λ=615 nm due to cavity resonance. It could be also noted the absorption for the reference solar cell in the long wavelength range (after λ=700 nm) is only ~10%. This is expected because the light losses at this small thickness at the long wavelength become severe. integrating the Au NGs at the back of the solar cell showed a large increase in absorption especially in the long wavelength range both for TE and TM polarized light.

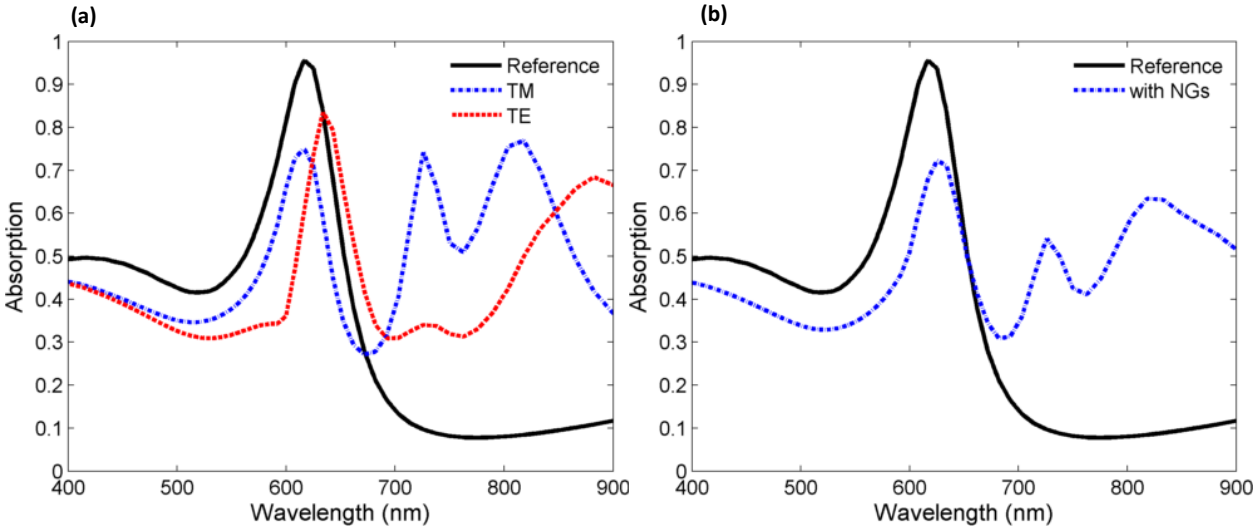

Figure 80: (a) absorption of the reference a-Si solar cell (black solid line), a-Si solar cell with NGs illuminated by TE polarized light (red dashed line) and TM polarized light (blue dashed line). (b) Absorption of the reference solar cell (black solid line) and the solar cell with NGs with unpolarised light (blue dashed line).

For TM polarized light, two well defined peaks at 725 nm and 820 nm could be observed. These peaks are due to the excitation of surface plasmon polariton (SPP) propagating waves that are only excited using TM polarized light. The average in absorption between TE and TM polarized light is shown in Figure 80 (b) while the enhancement in absorption at each wavelength is calculated and shown in Figure 81. It is clear that the absorption enhancement due to TM polarized light is higher reaching a factor up to 10 at 820 nm.

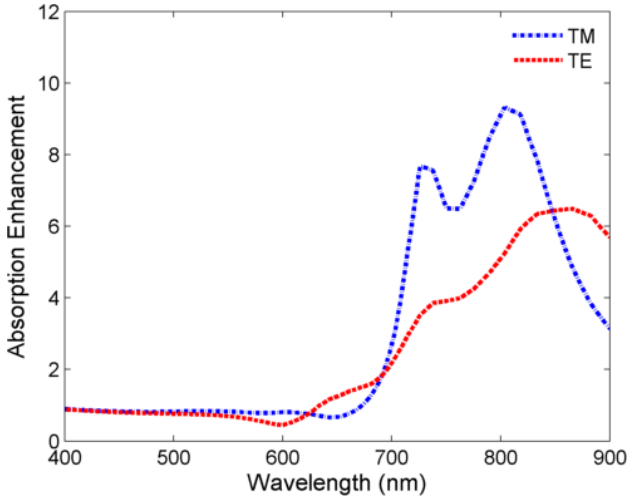

Figure 81: Absorption enhancement as a function of the wavelength.

To further understand this optical behaviour, a closer look at the absorption fields at specific wavelengths is performed. Figure 82 shows these absorption fields at the three major wavelength were a high absorption is calculated. At 615 nm, this is the on-resonance wavelength where the reference cell already shows a large absorption. This is clear in Figure 82(a) where the light is localized inside the whole a-Si film (marked with white dashed lines). Adding the NGs caused the light to be localized around the Au gratings as shown in Figure 82(b and c). At 725 nm and 820, it is an obviously off-resonance case for the reference a-Si thin film where light is extremely weak inside the layer. Adding the NGs showed a much intense light localization inside a-Si for both TE and TM polarized light. For TE polarized light, localized light around the NGs could be observed due to localized plasmons around the vertical walls of the Au gratings as shown in Figure 82(e and h). For TM polarized light, propagating SPP waves are present as shown in Figure 82(f and e) where light is also localized inside the a-Si thin film.

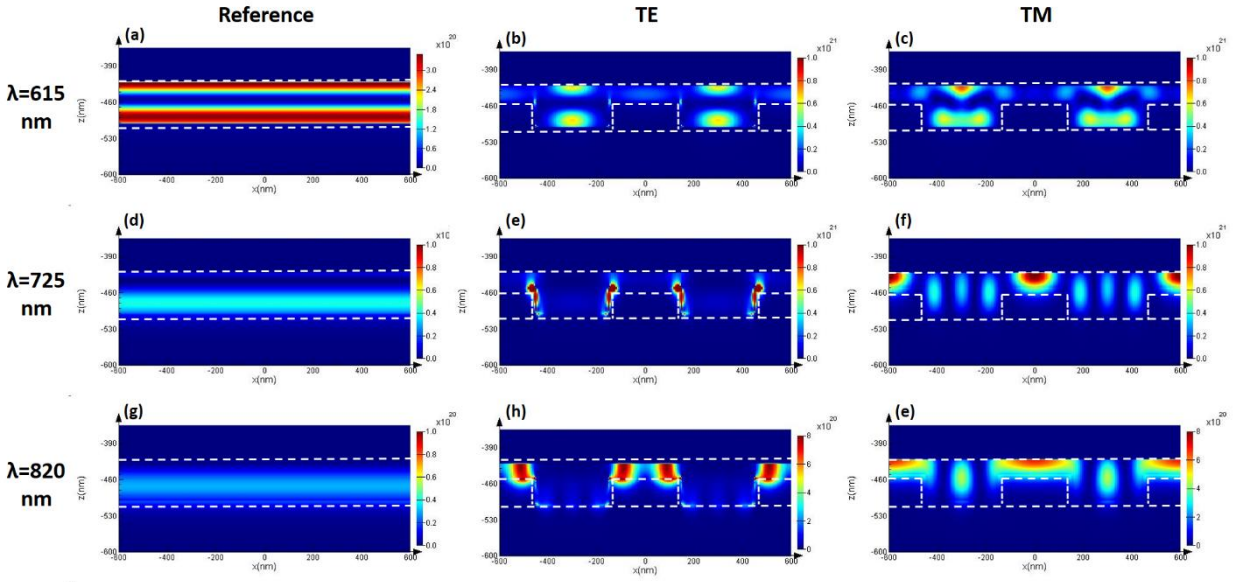

Figure 82: Absorption fields at (a,b,c) 615 nm, (c,d,f) 720 nm, and (g,h,e) 820 nm for the reference solar cell, solar cell with NG with TE polarized light, and with TM polarized light, respectively. Units of the bar code is W/m^3.

Thus, it could be concluded that adding the NGs caused the amount of unabsorbed light to get trapped inside the a-Si thin film instead of being lost. To summarize the above observations, the generation rate is calculated. The generation rate is the integration of the absorption at all wavelengths. A comparison between the generation rates of a-Si solar cell without Au NGs, with Au NGs for TE, and TM polarized light is shown in Figure 83(a, b and c) respectively. An obvious enhancement in the amount of light absorbed in the a-Si after the addition of Au NGs could be seen from the generation rate relative to the reference solar cell.

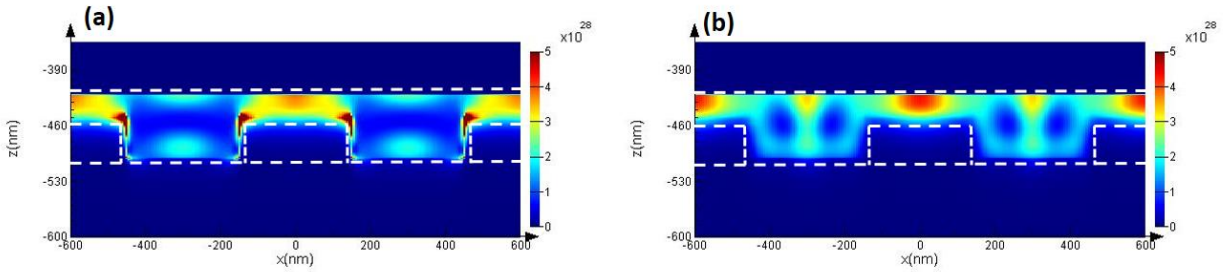

Figure 83: Generation rate for (a) solar cell with NGs for TE polarized light, and (b) solar cell with NGs for TM polarized light. Units of the bar code is number of absorbed photons/m^3 s.

Thus, in this section, it was proved that absorption inside extremely thin film a-Si could be enhanced by adding Au NGs. This is done by trapping the light inside the a-Si layer that would be otherwise lost

in transmission. The enhancement is found for both TE and TM polarized light with TM polarized light showing higher enhancement due to the excitation of SPP waves. However, the enhancement calculated for the above structure is only in the long wavelength range. Additionally, a huge amount of incident light is still lost in reflection on the top surface of a-Si due to the high difference in refractive index between air and a-Si. Thus, the next section is concerned with minimizing this problem.

4.3.2. Optical simulations of amorphous silicon solar cells with nanocones

Simulation details

Here, another nanostructure is examined to increase light trapping inside a-Si thin film solar cells. The configuration proposed here aims to reduce the reflection on top of the a-Si layer. The high difference in refractive index between the air and a-Si (4.3) cause a huge amount of light to be reflected from the surface and not even entering the a-Si film. Texturing the surface is one of the most efficient technique to reduce this reflection. This texture could take several forms. Nanocones are one of the most efficient texturing structure due to causing a graded change in refractive index between air and a-Si resulting in better refractive index matching and less reflection. The nanotexturing presented in this chapter consists of an array of periodic nanocones (NCs). They were added by replacing the top most part of the a-Si layer by the periodic nanotextruing as shown in Figure 84. The texture is described by a cone with a circular shaped base. The nanocones (NCs) were characterized by their height, period, and opening angle as shown in Figure 85. The base diameter was changed by changing the opening angle.

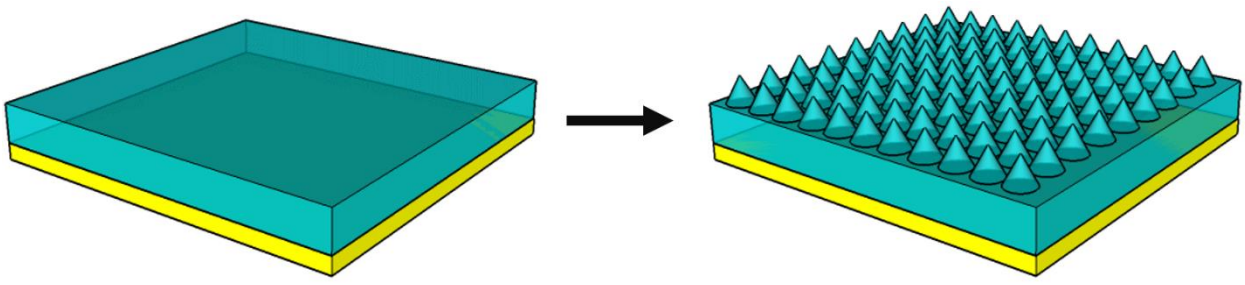

Figure 84: Schematic showing the addition of the array of periodic NCs only in the device.

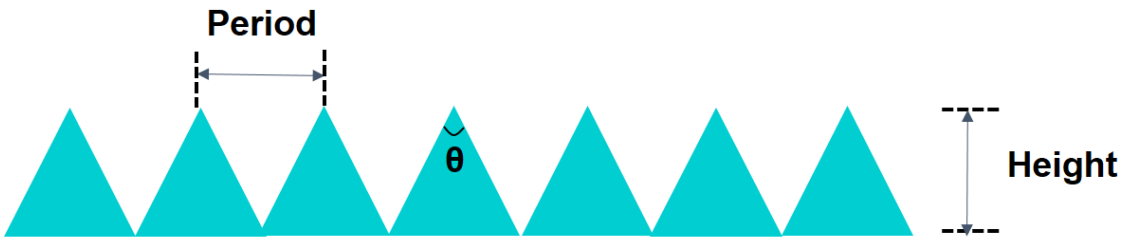

Figure 85: Schematic of the Silicon NCs showing all its parameters: opening angle, period, and height of the NCs.

All parameters in the simulation region is kept unchanged. The NGs at the back of the solar cell were removed the NCs were added on top keeping all boundaries the same. The simulation region for this structure is shown in Figure 86. The absorption, absorbed power, short circuit current, and the enhancement are all calculated with the same techniques used in the previous section.

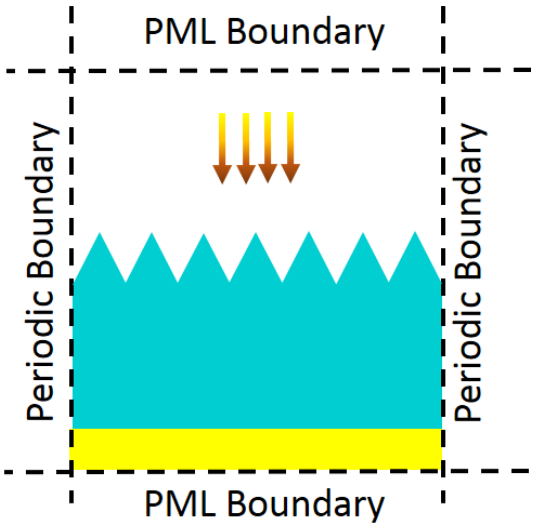

Figure 86: Schematic showing the simulation region for the solar cell with Silicon NCs only.

Optimization and results

To optimize the NCs, several parameters must be taken into consideration: the height, base diameter in terms of the opening angle, and the period of the NCs. As a starting point, several opening angles (Theta) has been tried for different NCs height and the enhancement factor for AP and J_{sc} was calculated. Remember that the enhancement factor is the ratio between the AP after adding the NC to the AP before adding the NC. The thickness of the underneath a-Si layer below the NC was kept at 200 nm for all NCs heights and the period was kept at 300 nm. Figure 87(a and b) show the enhancement

factor for AP and J_{sc}, respectively. It could be seen that for each height, the enhancement factor increases as the base diameter increases if all other parameters are kept unchanged. In addition, as the height increases, the enhancement factor increases where the highest enhancement factor is for H = 100 nm and Theta = 110°.

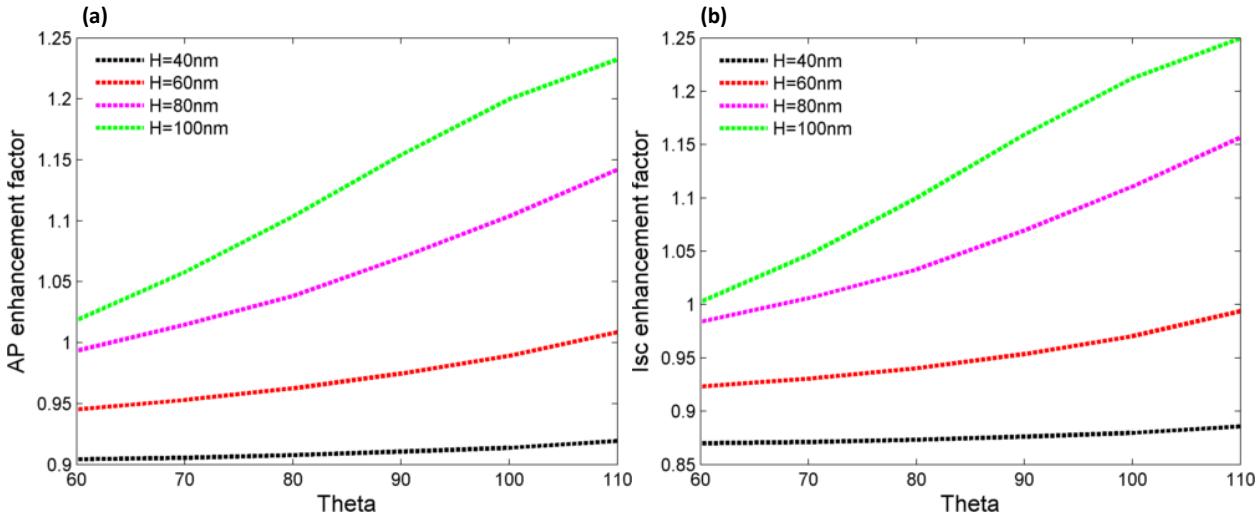

Figure 87: (a) AP and (b) J_{sc} enhancement factor versus the opening angle for the solar with NCs at different heights

After knowing that larger heights cause the larger enhancement. The height in the next step was set to 100 nm and the other parameters were optimized. An enhancement factor map was calculated for the period versus the opening angle Theta. The period was calculated as a function of the angle (P=n*Angle). The opening angle varied between 50 to 120 degrees and the period varied as a function of the angle for each simulated angle. Figure 88 shows these enhancement map. The optimized geometrical parameters of the NCs were extracted from the enhancement map. The NC height was fixed to 100 nm for all simulations, the period was found to be 120 nm with cone base diameter of 115 nm.

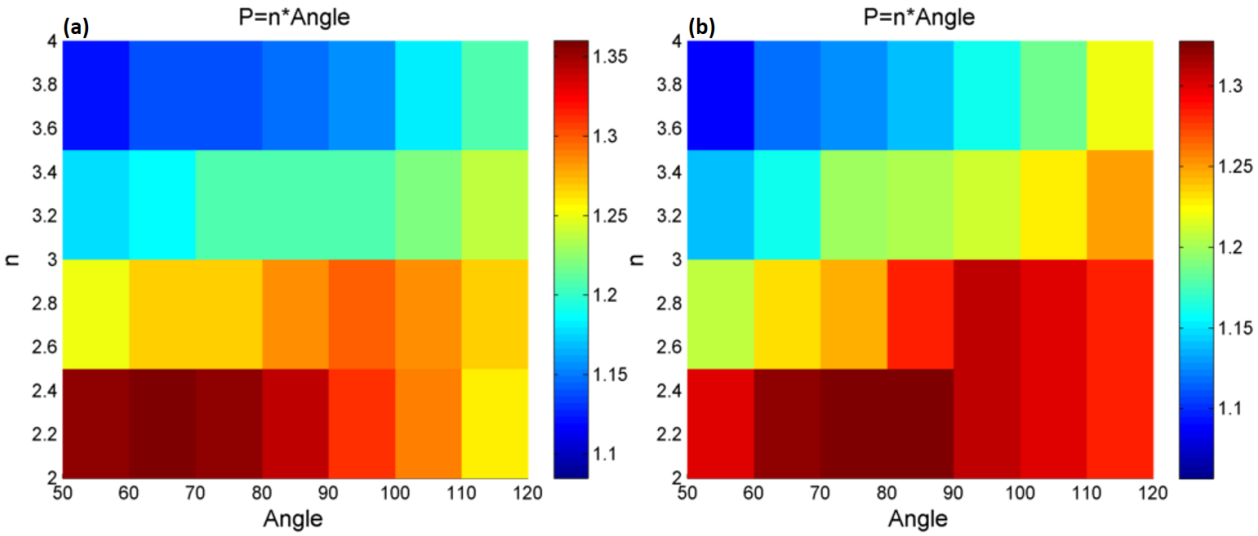

Figure 88: (a) AP and (b) J_{sc} enhancement map for the period versus the opening angle Theta

Next, the effect of changing the a-Si thickness was studied by applying these optimized NCs on solar cells with various a-Si thicknesses. Similar to Figure 79, the enhancement factor increased and decreased depending on the effective thickness of the film. The larger enhancement factor was calculated for the largest thickness of 300 nm. An enhancement of 36% was found due to adding the NCs on 300 nm a-Si thick solar cell. Since the NCs structures are symmetrical in the X and Y directions, they are polarization independent. Thus, no need for optimizing for both TE and TM polarized light because both give the same result.

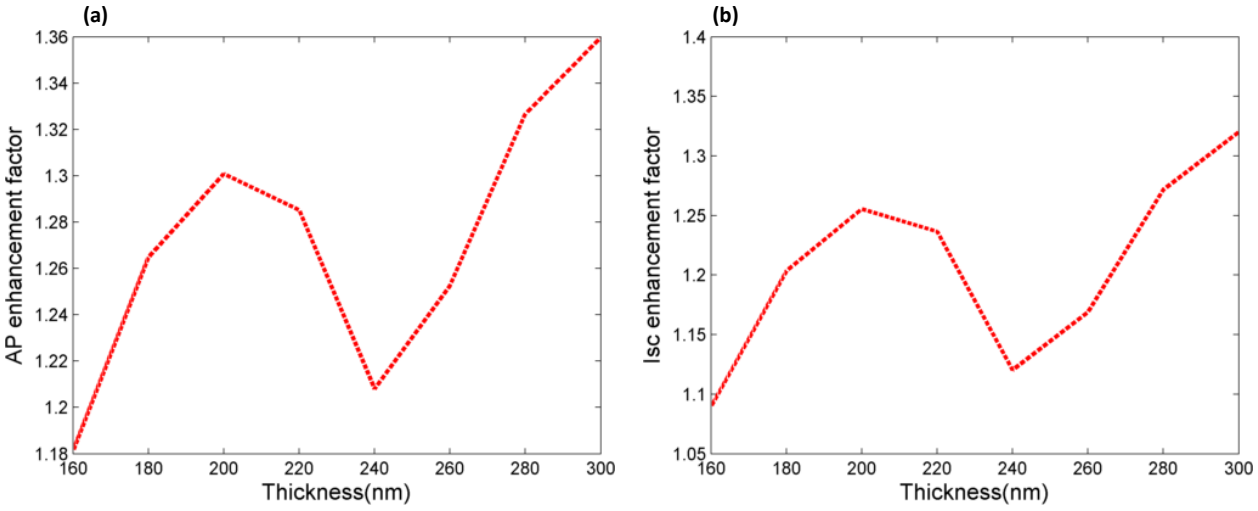

Figure 89: (a) AP and (b) J_{sc} enhancement factor for different a-Si film thicknesses with the optimized NCs parameters.

The absorption inside the 300 nm a-Si solar cell with the optimized NCs on top is then calculated. Figure 90 shows the absorption for the reference solar cell without the NCs and the absorption for the one with the NCs. It could be seen that the reference has two major peak at ~615 nm and ~750 nm due to the cavity resonance. Adding the NCs caused a large, broadband increase in the absorption at the short wavelength range due to the much reduced reflection. The improvement in the short wavelength specifically is expected, because the anti-reflection effects dominates light absorption in the short wavelength range [56].

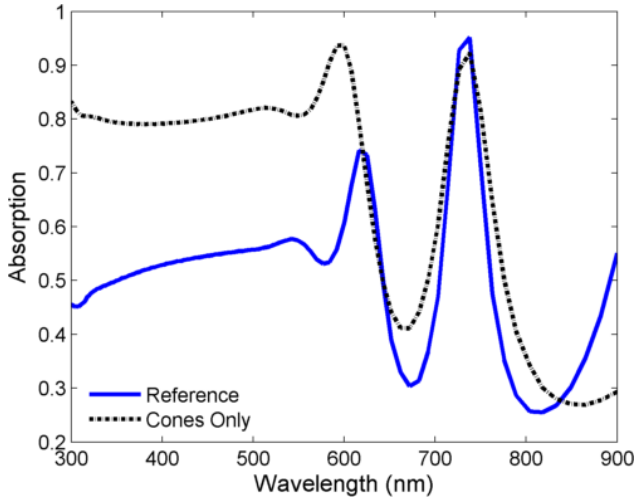

Figure 90: Absorption of 300 nm a-Si solar cells without NCs (blue solid line) and with NCs on top (black dashed line).

Finally, random roughness on top of a-Si thin film is also simulated to compare between random texture and periodic NCs texture. Figure 91(a) shows the absorption for TE and TM polarized light for this structure. It could be seen that this random structure also seem to be polarization insensitive with almost the same absorption achieved for both TE and TM polarized light.

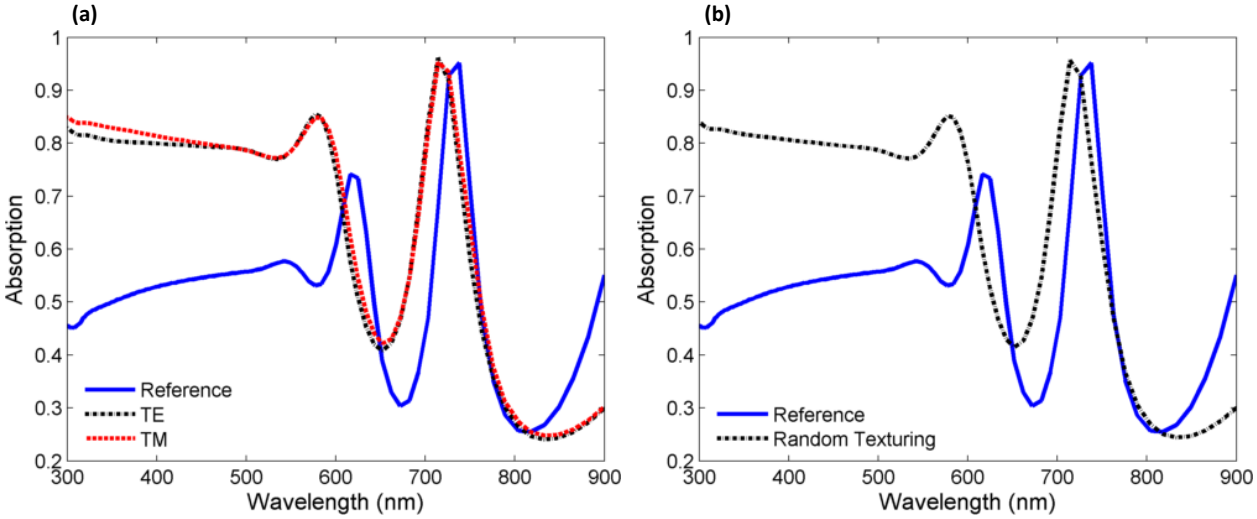

Figure 91: (a) Absorption of 300 nm a-Si solar cells with random roughness on top for TE and TM polarized light separately and (b) for the unpolarised light.

A comparison between the absorption of a-Si solar cells with periodic NCs and with random roughness is shown in Figure 92(a). Similar enhancement in absorption was achieved using the random roughness, however, the periodic NCs had higher absorption at some wavelengths leading to higher overall absorbed power. A part of the random roughness added in the simulation is showed in Figure 92(b).

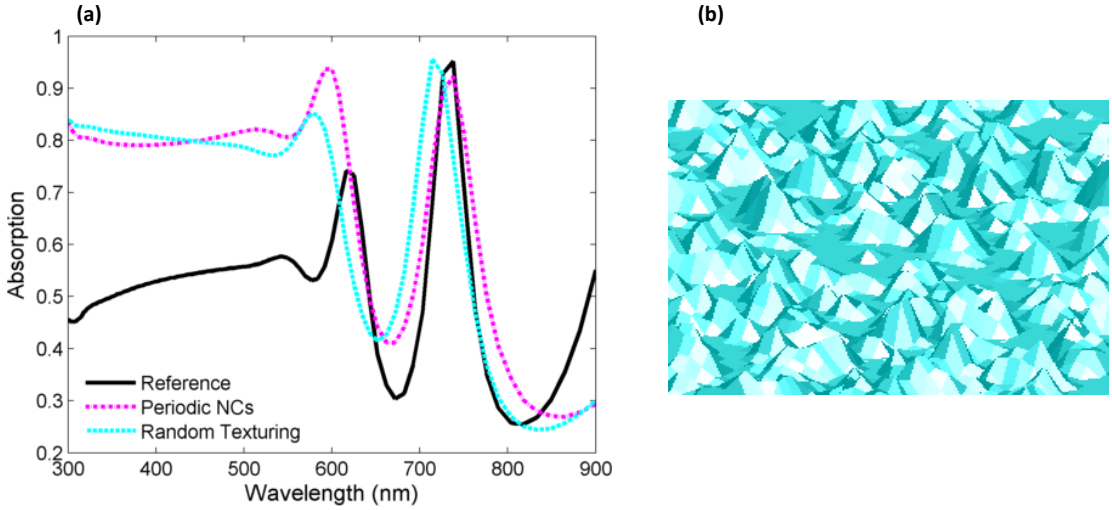

Figure 92: (a) Absorption of 300 nm a-Si solar cells with random roughness (cyan dashed line) compared to the absorption of a-Si solar cell with periodic NCs (pink dashed line). (b) Part of the random roughness structure used un the simulation.

Further analysis has been made to gain an insight on the absorption at each specific wavelength. The

absorption fields at three wavelengths have been visualized: 450 nm, 600 nm, and 850 nm and plotted in Figure 93. At 450 nm, a very minimal amount of light is absorbed by the reference solar cell. For the structure with a texture, either random or periodic, light is seen to be localized mainly in the area where the a-Si is textured and does not propagate well in the underneath a-Si film. Around the wavelength where the reference solar cell has a cavity resonance peak (i.e. 600 nm), light fields are seen in the reference cell. However, adding the texture significantly increased the intensity of light inside the texture and inside the underneath film. For the periodic NCs, light localization is well defined and has its maximum value inside the NCs and just below them unlike the random texture case where light localization is random throughout the structure. It could be seen here that adding the texture on top of a-Si films increased the scattering inside the underneath film causing the increased absorption.

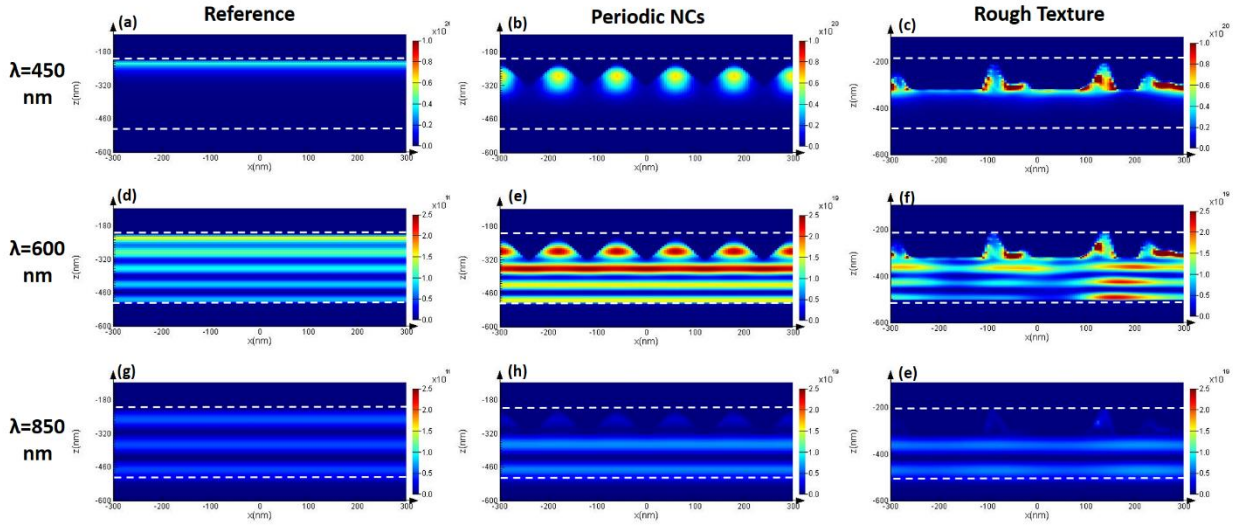

Figure 93: Absorption fields at (a,b,c) 450 nm, (c,d,f) 600 nm, and (g,h,e) 850 nm for the reference solar cell, solar cell with periodic NCs, and SC with random texture, respectively. All the figures are for TE polarized light. Units of the bar code is W/m^3.

At 850 nm, an off-resonance wavelength for both the reference solar cell and the textured ones, it could be seen that almost no light fields appear in the absorption fields. Thus, it could be concluded that these textures are important for decreasing the reflection and increasing the light scattering inside the a-Si films but this mainly happens in the short wavelength region. Light losses in the short wavelength range still exists. Driven by the fact that adding the NGs in the first section caused an increased absorption mainly in the long wavelength range, a double light trapping configuration is proposed that

aims to achieve a broadband absorption over the whole visible/near infra-red range by adding both a texture on top of a-Si films in addition to gratings at the back metal contact. The next section thoroughly describes this structure and its optimization.

4.3.3. Optical simulations of the double light trapping structure

Simulation details

In this section, both the NCs and NGs were added in the a-Si solar cell to achieve a high, broadband light absorption. The NCs are added to reduce the reflection and increase the absorption in the short wavelength range, and the NGs were added to reduce the transmission and increase the absorption in the long wavelength range. The already optimized NCs and NGs were used in this section. Thus, both the NCs and the NGs were added in the simulation region and all other parameters are kept unchanged. Figure 94(a) shows the simulation region for the proposed double light trapping structure.

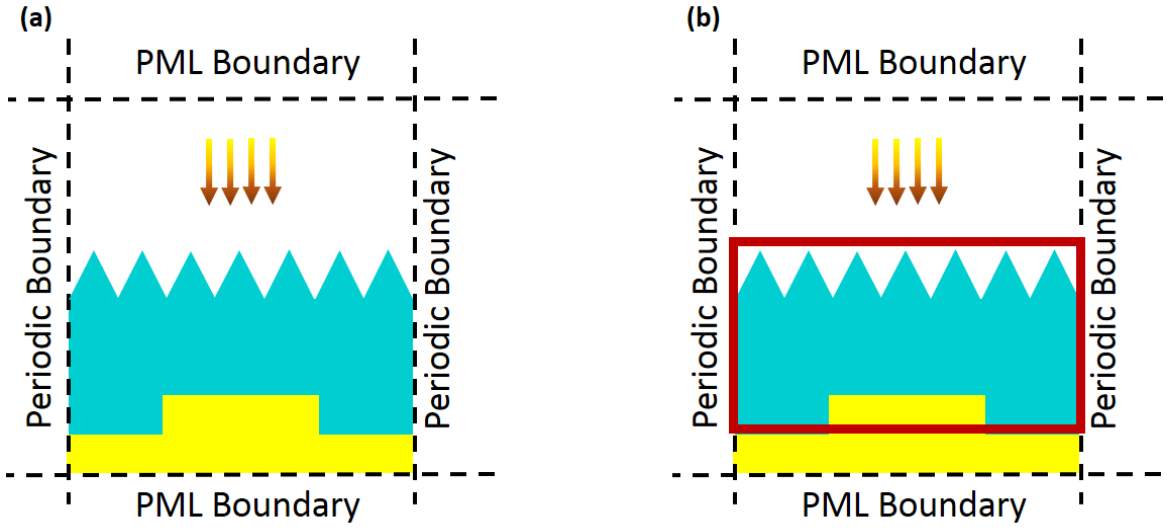

Figure 94: (a) Schematic showing the simulation region for the solar cell with NCs and NGs. (b) Schematic showing the simulation region with the addition of the field monitor that measures the absorption.

The absorption is measured with the same technique used in the previous sections. In summary, absorption field monitor is placed around the whole a-Si layer including the NCs and NGs as shown in Figure 94(b). An index monitor is also added overlapping the absorption field monitor to differentiate between the refractive index in Au and in a-Si to be able to calculate the absorption in a-Si separately. The absorbed power, short circuit current, and the enhancements are calculated using the same equations

explained and used previously.

Optimizations and Results

Since the geometrical parameters of NCs and NGs were previously optimized, both the NCs and the NGs were directly added on different a-Si thick solar cell. Figure 95 shows the enhancement factor for AP and J_{sc}. Since NGs were added again, a polarization sensitive structure, the absorption is measured for TE and TM polarized light separately and the average between them is calculated. The optimum a-Si thickness is found to be 280 nm with a 45% increase in absorbed power compared to the reference cell.

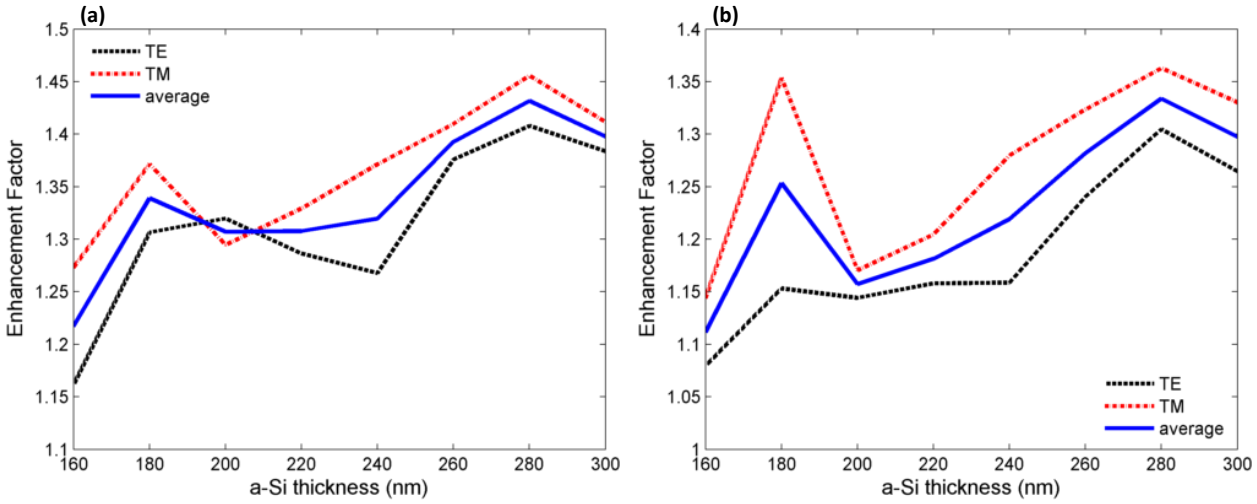

Figure 95: (a) AP and (b) J_{sc} enhancement factor at different a-Si film thicknesses with the optimized NCs and NGs parameters.

This huge enhancement could be visualized in Figure 96 where a large, broadband increase in the whole wavelength range could be observed. The enhancement in the short wavelength range is due to the replacement of the flat a-Si surface with the NCs structure as explained in the previous section. The absorption in the a-Si NCs was much higher than their flat counterparts due to the graded change in the refractive index leading to lower reflection. In addition, enhanced light coupling to the underneath a-Si layer was achieved contributing in this large increase in absorption.

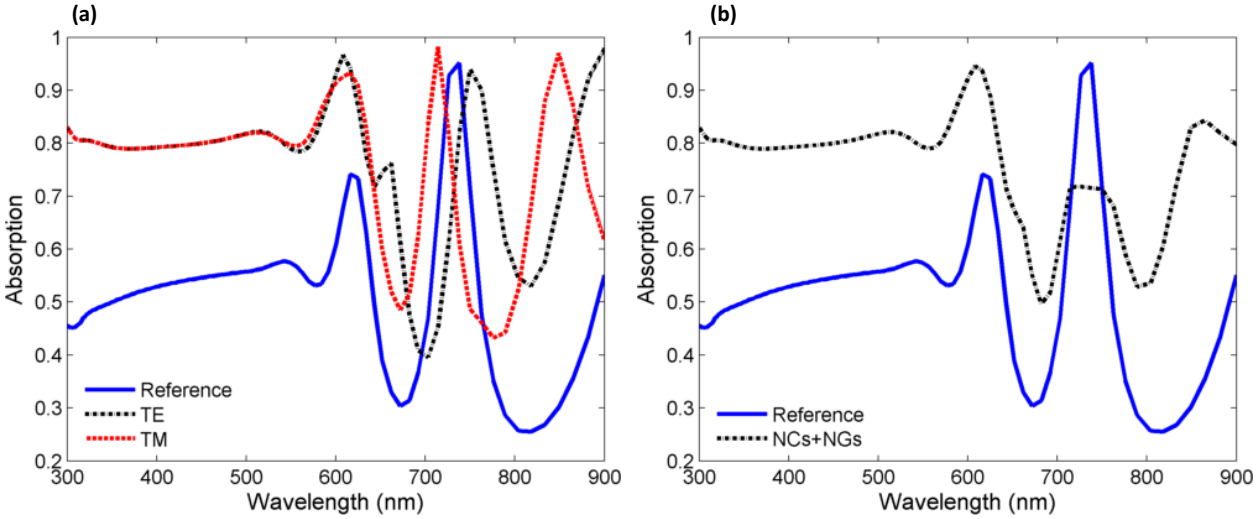

Figure 96: (a) Absorption of 280 nm a-Si solar cells with periodic NCs on top and NGs at the back for TE and TM polarized light separately and (b) for the unpolarised light.

The addition of the NGs extended this enhancement to include the red part of the spectrum as could be seen in Figure 97 where a comparison between the absorption for the structure with NCs only to the structure with NCs and NGs is plotted. This additional enhancement is due to the excitation of surface plasmon polaritons waves. The high near field enhancement around the NGs was the main contributor to the enhancement in this spectral range due to the ability to localizing the light inside the thin active layer. The absorption shown in Figure 96(b) is the average between the absorption for TE and TM polarized light. Figure 98 shows the same observation with random texturing instead of the periodic NCs.

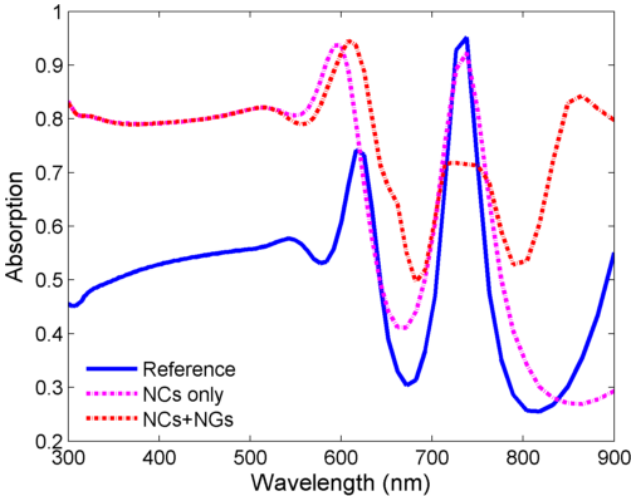

Figure 97: Absorption comparison between the structure with periodic NCs only (pink dashed line) and the structure with periodic NCs and NGs (red dashed line).

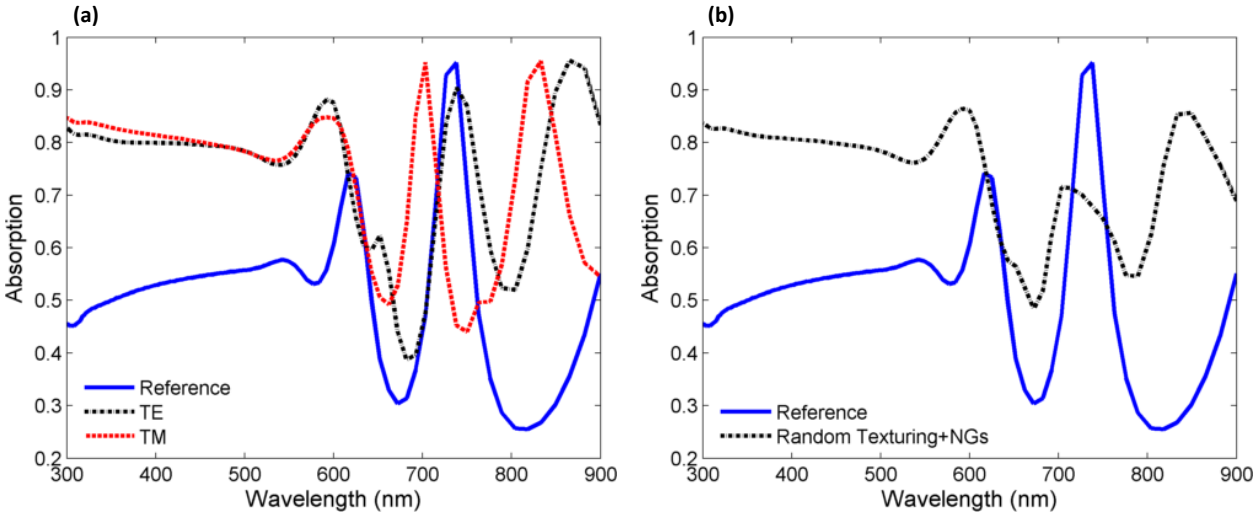

Figure 98: (a) Absorption of 300 nm a-Si solar cells with random roughness on top and NGs at the back for TE and TM polarized light separately and (b) for the unpolarised light.

Again, we looked at the absorption at specific wavelengths and plotted it in Figure 99. At 450 nm, the absorption mainly happens in the NCs or random texturing. Thus, the enhancement at this wavelength happens mainly due to the addition of the texture without any observed contribution from the NGs. At 600 nm, the absorption increased compared to the reference solar cell. Light coupling to the a-Si film is significantly better after the addition of the nanostructures. Both the NCs and the NGs contribute in the absorption enhancement as could be seen in Figure 99(e and f). This observed because light localization is observed around the NGs and inside the NCs. In addition, light is also scattered in

the while a-Si layer due to the better light coupling. At 850 nm, almost no light is absorbed by the reference cell and even the addition of NCs only did not help in increasing the light as observed previously in Figure 93 (h and e). However, after the addition of NGs an increased light coupling at this wavelength occurred mainly due to addition of NGs as shown in Figure 99(h and e) where the light localization is mainly around the NGs.

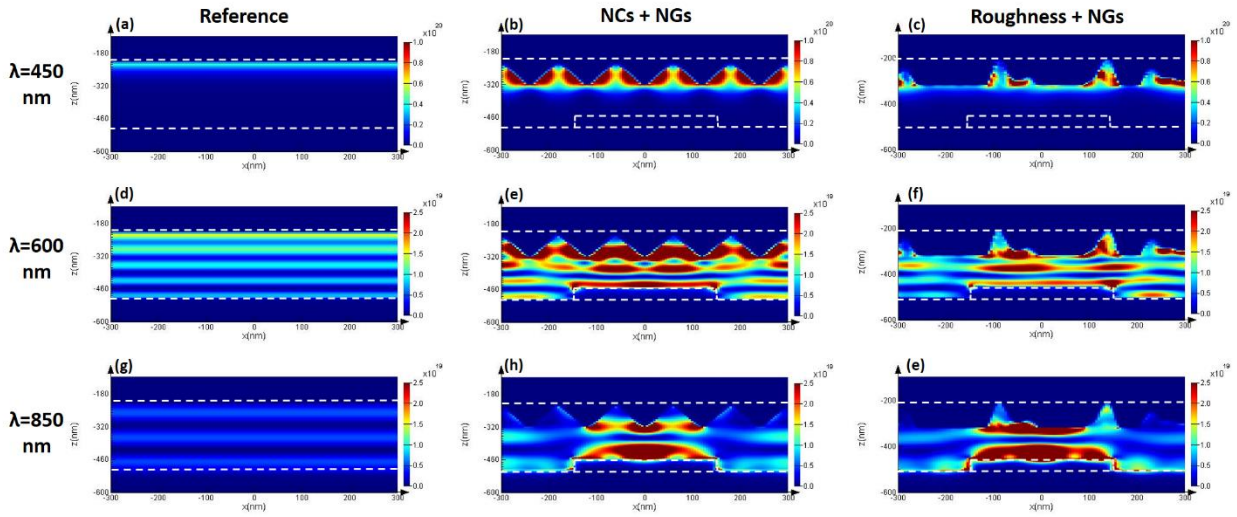

Figure 99: Absorption fields at (a,b,c) 450 nm, (c,d,f) 600 nm, and (g,h,e) 850 nm for the reference solar cell, solar cell with periodic NCs and NGs, and solar cell with random texture and NGs, respectively. All the figures are for TE polarized light. Units of the bar code is W/m^3.

Finally, the generation rate for the structure of bare a-Si film, with NCs only, and with and NGs for TE and TM polarized light are shown in Figure 100. It could be seen that replacing the top part of the a-Si films with the NCs increased the absorption mainly in the top area and increased the light coupling to the underneath layer [Figure 100(b)]. The addition of NGs increased the light localization inside the NCs even further in addition to localizing the light around the NGs. Moreover, the light coupling to the whole a-Si layer is further enhanced [Figure 100(c and d)].

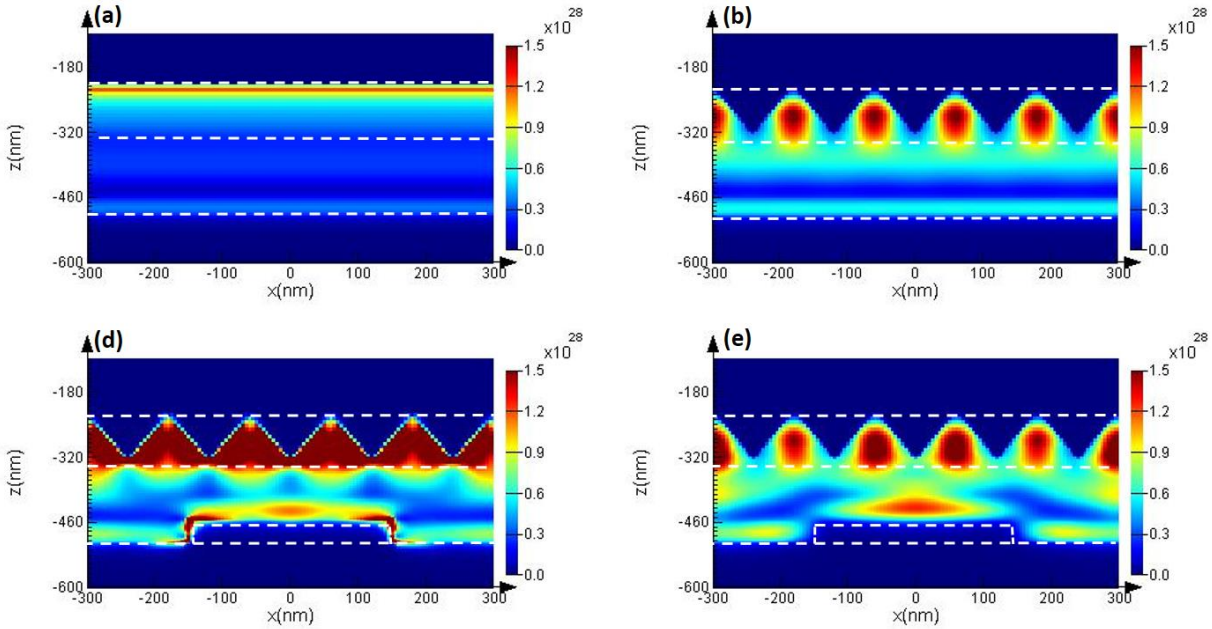

Figure 100: Generation rates for (a) Reference a-Si solar cell, (b) solar cell with NCs, (c) solar cell with NGs for TE polarized light, and (d) solar cell with NGs for TM polarized light. Units of the bar code is number of absorbed photons/m^3 s.

To sum up the differences between all structures presented in this chapter, comparison between a-Si solar cells structures with NGs only, NCs only, random texture only, and with both configurations have been made. This comparison is made by measuring the AP enhancement factor for each structure for different a-Si thicknesses. This comparison is shown in Figure 101. A 45% increase in absorbed power was found for the structure with both NGs and periodic NCs with 280 nm thick a-Si layer compared to only 32% for the structure with NCs only and 8% for the structure with NGs only with the same a-Si thickness.

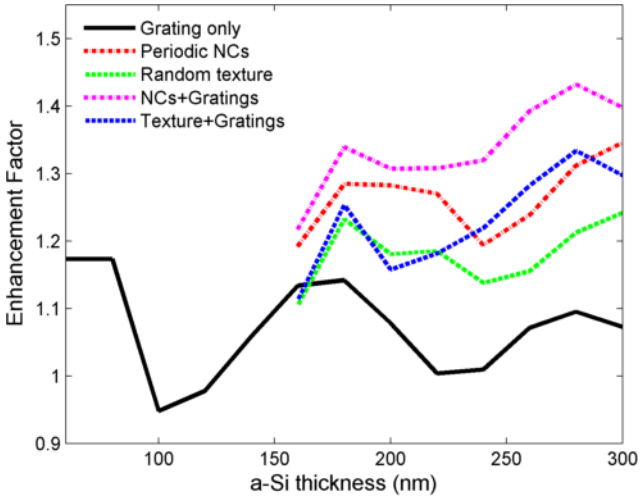

Figure 101: Comparison between the AP enhancement factor of a-Si solar cells structures with NGs only (black solid line), NCs only (red dashed line), random texture only (green dashed line), and with both configurations (pink dashed line for NCs + NGs and blue dashed line for random texture + NGs).

4.4.Conclusion

In summary, we report the fabrication of high, broadband, and wide angle absorption enhancement in Silicon nanocones on top of a thin film a-Si layer using excimer laser. The fabrication technique reported in this work is easily scalable, fast, and does not require any especial conditions or gases. The effect of changing the laser parameters such as energy density, time, and frequency on the morphology and the absorption are studied and a thorough comparison is made. In addition, we reported the fabrication of Silicon nanowires from amorphous Silicon thin film using the same method. Excimer laser is used to re-distribute the material within the sample forming nanowires with lengths equals triple the thickness of the deposited amorphous Silicon thin film. The effect of changing the laser energy density, exposure time, and frequency on the morphology and the size of the obtained nanowires are also studied. Changing the time and frequency had almost no effect on changing the diameter, however, they resulted in an increase in the length. The fabricated nanostructures showed broadband absorption enhancement in the whole visible and near infra-red wavelength range. The highest absorption was found for nanowires fabricated at f=40 Hz. In addition, less than 4% reflection is measured for angle of incidences up to 60°. These indispensable optical properties along with the easy fabrication and the low cost substrate used (i.e. amorphous Silicon) will help in increasing the overall efficiency of the

nanowires based solar cells making them more competitive in the photovoltaic market.

An enhancement of 45% in absorbed power was numerically achieved through 3D FDTD simulations in a-Si solar cell. This enhancement is due to the addition of periodic nanocones texture on top of the a-Si surface which reduced the reflection and increased light coupling in the a-Si layer. In addition, Au periodic nanogratings were added on the back electrode leading to increased light absorption in the long wavelength due to the excitations of SPP waves and trapping the light inside the a-Si layer.

4.5.Future directions

For further analysis of these structures, full p-n junction should be fabricated for the solar cell and electrical simulations should be done.

Chapter 5 : Hybrid Silicon/polymer solar cell

5.1.Introduction

Reducing the cost of Si solar cells is essential to make it competitive with conventional energy sources. Most of the Silicon modules' cost arise from the cost of the Silicon material and the fabrication of the p-n junction[73]. Thus, substantial improvement in light absorption in Si is needed to obtain highly absorbing cells with the least amount of Si used. Si nanowires (SiNWs) are believed to contribute in solving this problem as they have huge capabilities in light trapping and the advantage of decoupling the absorption direction and charge collection direction which maximizes the efficiency of the solar cell[159,97].

The shape and geometry of the Si NW has huge effect on its optical properties. For solar cells, vertical NWs on top of the Si substrate has proven to have superb antireflection and light trapping properties[19,93,74]. Furthermore, organic/inorganic hybrid structures have gained huge attention due to its ability to form a Schottky junction between the Si and a polymer that could replace the expensive fabrication processes for forming a p-n junction. This structures combines the advantages of both materials (i.e. stability of Si and the easy processing of polymers)[97,73,91]. Si films and SiNWs covered with the conductive polymer poly(3,4-ethylenedioxythiophene):poly(styrenesulfonate) (PEDOT:PSS) have been well studied in the literature[86,93,97,82]. In this structure, the absorption occur in the Si only making the efficiency of such devices similar to conventional Si p-n junction devices[73]. Thus, thick Si substrates are still needed to achieve decent absorption in the solar cell. poly(3-hexylthiophene):[6,6]-phenyl-C61-butyric acid methyl ester (P3HT:PCBM) has been also used on top of Si nanostructures to enhance the absorption in the device[85,75,81,172]. However, the maximum absorption of the polymer (i.e. P3HT) and Si are in the same range (400-700nm) resulting in a competition between the absorption of each material[79].

In this chapter, we report a wide broadband absorption spanning the whole visible and NIR range of the solar spectrum with only 5 Microns tapered Si NWs (TSiNWs) coated with the low band gap polymer poly[3,6-bis(40-dodecyl-[2,20]bithiophenyl-5-yl)-2,5-bis(2-ethylhexyl)-2,5-

dihydropyrrolo[3,4-]pyrrole-1,4-dione] (pBBTDPP2):PCBM.

5.2.Simulation method

Three dimensional (3D) finite difference time domain (FDTD) simulations are carried out to analyze the optical performance of the proposed structure. Comparisons between the optical behavior of bare SiNWs and TSiNWs are done with and without polymer coatings. The different structures simulated for SiNWs and TSiNWs are shown in Figure 102(a and b), respectively. While SiNWs have the normal cylindrical shape, a tipped cone in added for the TSiNWs in the simulations. In addition, different polymers with different band gaps are added to the structure and their absorptions are compared.

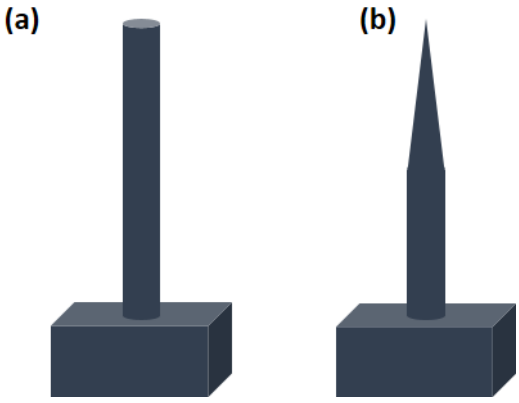

Figure 102: Schematic comparing between (a) conventional Silicon nanowires (SiNW) and (b) tapered Silicon nanowires (TSiNW)

A schematic showing the simulation region is shown in Figure 103. The whole structure consists of periodic SiNWs, thus, periodic boundary condition is applied on the sides of the NWs while perfectly matched layer (PML) boundaries are applied above and below the simulation region. The NWs are placed on top of a silicon substrate. Three monitors are added to measure the absorption and reflection. The absorption is determined by calculating the difference between the power transmitted from transmission monitor 1 and the power transmitted from transmission monitor 2 at each wavelength. Thus, only the absorption in the nanowires are measured without taking into consideration the absorption in the silicon substrate. Reflection monitor above the source is added to measure the reflection. Transmission from the NWs could be calculated by calculating the light transmitted from transmission monitor 2 only. The source is a plane wave light source placed on top the NWs. The

polymer coating is added by placing a NW with larger diameter around the SiNW resulting in having a polymer coating surrounding the SiNW with a variable thickness.

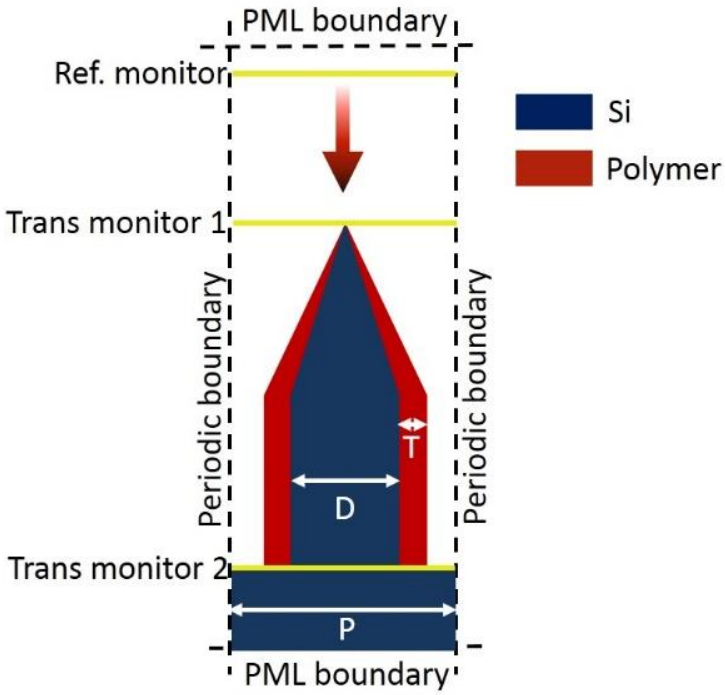

Figure 103: Simulation region for the proposed design of tapered nanowires coated with polymer.

As a start, the diameter (D) of the wires is fixed at 400 nm and the period (P) at 600 nm. The whole wire length is 5 microns. The polymer coating thickness (T) is varied from 10 nm to 100 nm. Before optimizing the polymer coating thickness, a comparison between the absorption in 5 microns of the conventional SiNWs and TSiNWs is made. Then, a comparison between the enhancement in absorption after adding P3HT:PCBM, the low bandgap polymer pBBTDPP2:PCBM and PDPP3T is carried out.

Next, a thorough optimization is done to find the optimum TSiNW diameter along with the optimum polymer thickness. This is done by varying the TSiNW base diameter from 200 nm to 500 nm and varying the polymer thickness from 10 nm to 100 nm for each case. The absorbed power in each case is measured.

5.3.Optical analysis of hybrid Silicon nanowire/polymer solar cells

5.3.1. Optical analysis

The tapering of the SiNWs can reduce the reflection at the Si surface due to the gradual change in

refractive index between the air and the Si substrate. In addition, this gradual change should improve the light scattering than the case of conventional NWs where an abrupt change is implemented[173]. This could be seen in Figure 104 where the 5 µm long TSiNWs show much higher absorption than the conventional NWs with the same length especially in the short wavelengths. the diameter and period were fixed to 400 nm and 600 nm, respectively, for both NWs. A complete light absorption until 600 nm is achieved with only 5 µm TSiNWs without the need of any substrate. A 30% increase in AP is calculated for the TSiNW structure over the conventional SiNWs.

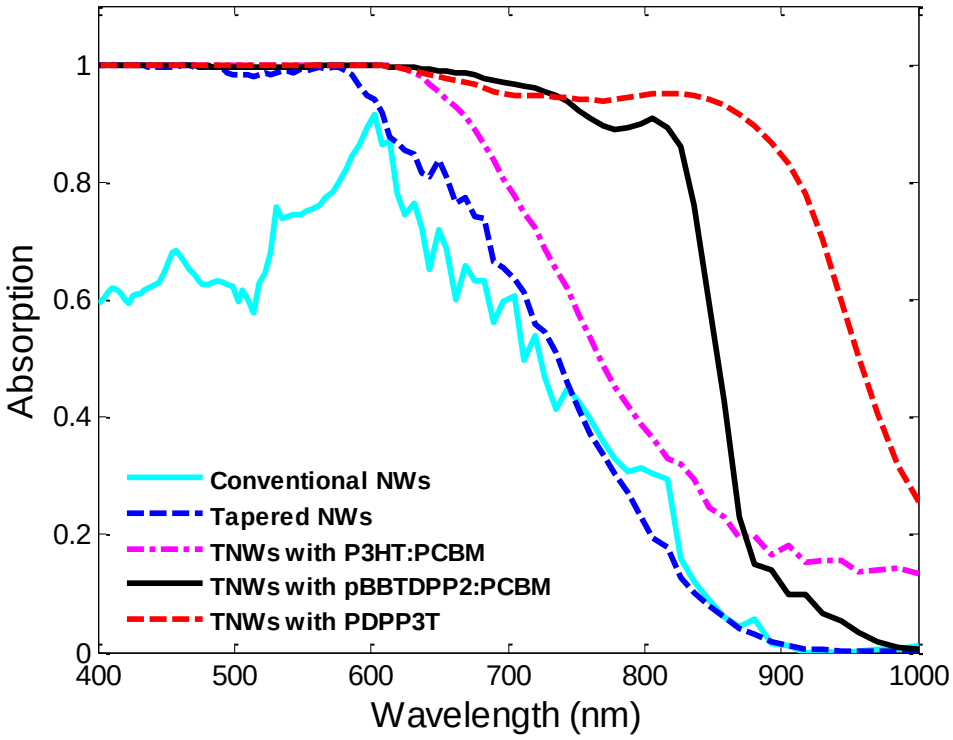

Figure 104: Absorption of conventional nanowires (cyan line), tapered nanowires (blue dashed line), TNWs coated with P3HT:PCBM (pink dashed line), TNWs coated with pBBTDPP2:PCBM (black line), and TNWs coated with PDPP3T (red dashed line).

Next, several polymers are added as a coating for the TSiNWs to form the p-n junction and extends the absorption of the NWs. The thickness for all polymers was fixed to 50 nm and the period was fixed to 500 nm. As mentioned previously, P3HT:PCBM has a bandgap of 1.9 eV and, hence, absorbs mainly in the same maximum absorption range of Si. Thus, a slight increase in absorption is observed only

after 650nm as shown in Figure 104. However, huge light losses are still observed for wavelengths larger than 700m. An 12% increase in absorbed power and 16% increase in J_{sc} was calculated after adding P3HT:PCBM over the bare tapered nanowire without polymer addition.

On the other hand, when a lower band gap polymer is added with 1.4 eV bandgap (i.e. pBBTDPP2:PCBM) is added, a large enhancement in absorption is found at longer wavelengths where an almost complete light absorption is achieved till 850 nm. 26% and 36% increase in AP and J_{sc}, respectively, were calculated for adding pBBTDPP2:PCBM over the bare TSiNWs. Moreover, when PDPP3T is added, a 1.3 eV bandgap polymer, absorption was further extended to absorb the whole visible and near infra-red range till ~1 μm achieving 40% enhancement in AP and 57% enhancement in J_{sc}. The enhancement percentage achieved after adding each polymer is summarized in Table 1. This structure provides an efficient way to trap high percentage of the incident photons with only few microns of Si covered with 50 nm of pBBTDPP2:PCBM. This could significantly reduce the device cost without the need of complex fabrication processes.

Table 1: Table comparing each polymer, their bandgaps, and the AP and J_{sc} enhancement percentage achieved for adding each polymer on TNWs.

Polymer	**Bandgap**	**AP enhancement**	**J_{sc} enhancement**
P3HT	1.9	12%	16.4%
pBBTDPP2	1.4	25.8%	34.6%
PDPP3T	1.3	40%	57%
PDPP3T (after optimization)	1.3	53%	76%

This significant enhancement could also be observed by looking at the reflection of each structure in Figure 105. Conventional NWs shows high reflection in the short wavelength range compared to TNWs. Less reflection in TNW is attributed to the better impedance matching between air and Silicon due to the graded change in refractive index. This impedance matching is further enhanced after adding the polymer due presence of a polymer with refractive index values between air and Silicon. Thus,

reflection is further reduced. Adding PDPP3T caused the reflection to be ~zero in the whole simulated wavelength range. Thus, reflection losses is almost eliminated by using only 5 µm long TSiNWs coated with a thin layer of PDPP3T.

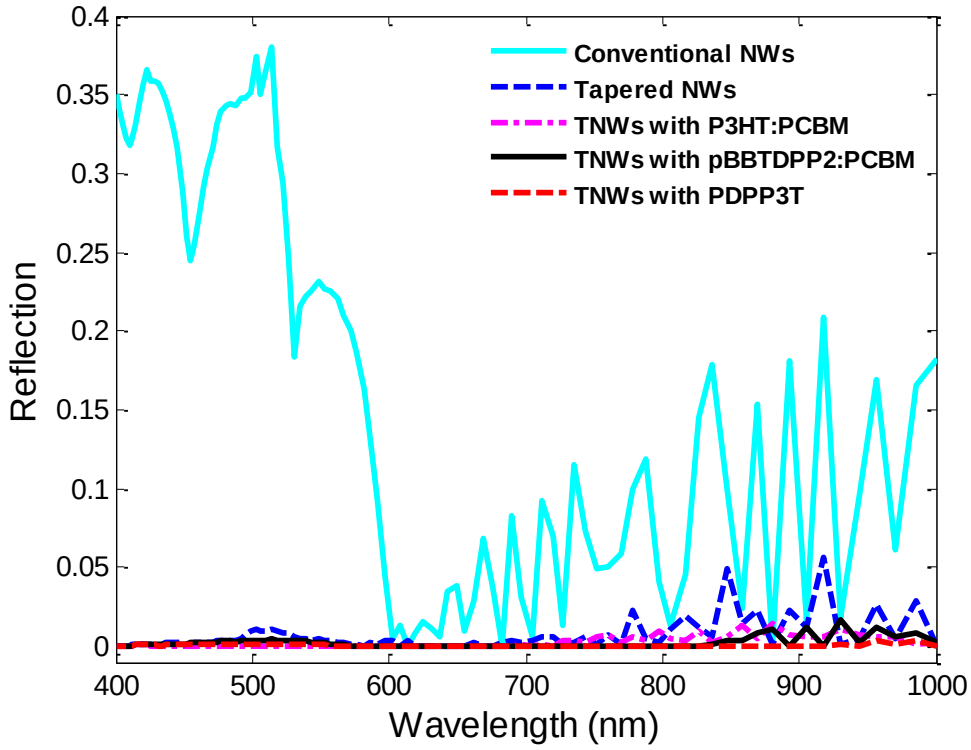

Figure 105: Reflection of conventional nanowires (cyan line), tapered nanowires (blue dashed line), TNWs coated with P3HT:PCBM (pink dashed line), TNWs coated with pBBTDPP2:PCBM (black line), and TNWs coated with PDPP3T (red dashed line).

To thoroughly compare between the conventional nanowires and tapered nanowires and between the effect of adding each polymer, absorption fields at specific wavelengths were visualized. First, comparison between conventional SiNWs and TSiNWs was done at different wavelengths. for conventional NWs, light is mostly concentrated on top on the nanowire at short wavelengths then it starts to spread along the length of the NW at longer wavelengths (i.e. from 700 nm) as shown in Figure 106. Figure 107 shows the absorption fields at the same wavelength for TNWs. Similarly, at short wavelengths (i.e. 400 nm), the light is mainly trapped on the top part of the NW for TNWs. However, it could be seen that light is much more intense in the case of TNWs with more than one order in

magnitude increase in light absorption. The sharp edge of the TNW creates a hot spot that is very efficient in light trapping and absorption. For longer wavelengths (i.e. 600 nm), light is still mainly localized in the top part for conventional NWs while it starts to spread along the wire for TNWs. At 700 nm, light starts to spread along the wire and get homogenously distributed along the NW in both cases while being more intense in the case of TNWs. At 900 nm, outside the absorption range of Si NWs, the light intensity inside both NWs starts to decrease. The light absorbed in the TNW is generally (at all wavelengths) higher than the case of conventional NWs due the better impedance matching, less reflection, and hot spot created at its sharp tip.

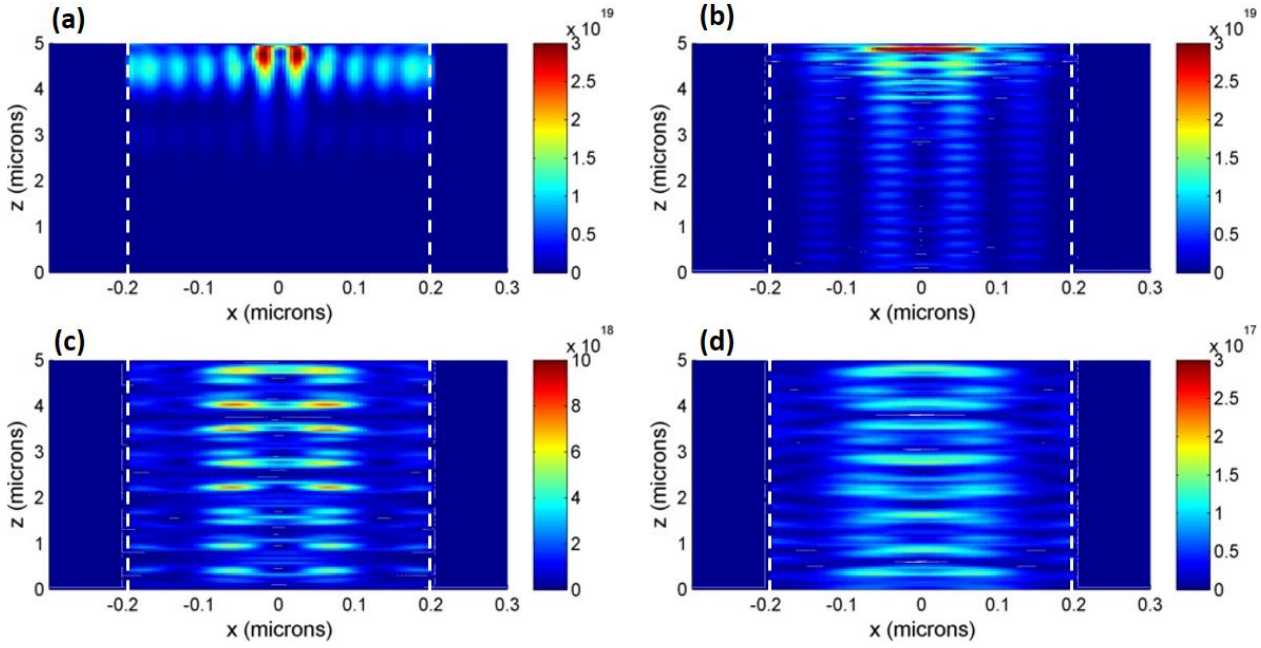

Figure 106: Absorption fields for conventional NWs at (a) 400 nm, (b) 600 nm, (c) 750 nm, and (d) 900 nm. Units of the bar code is W/m^3.

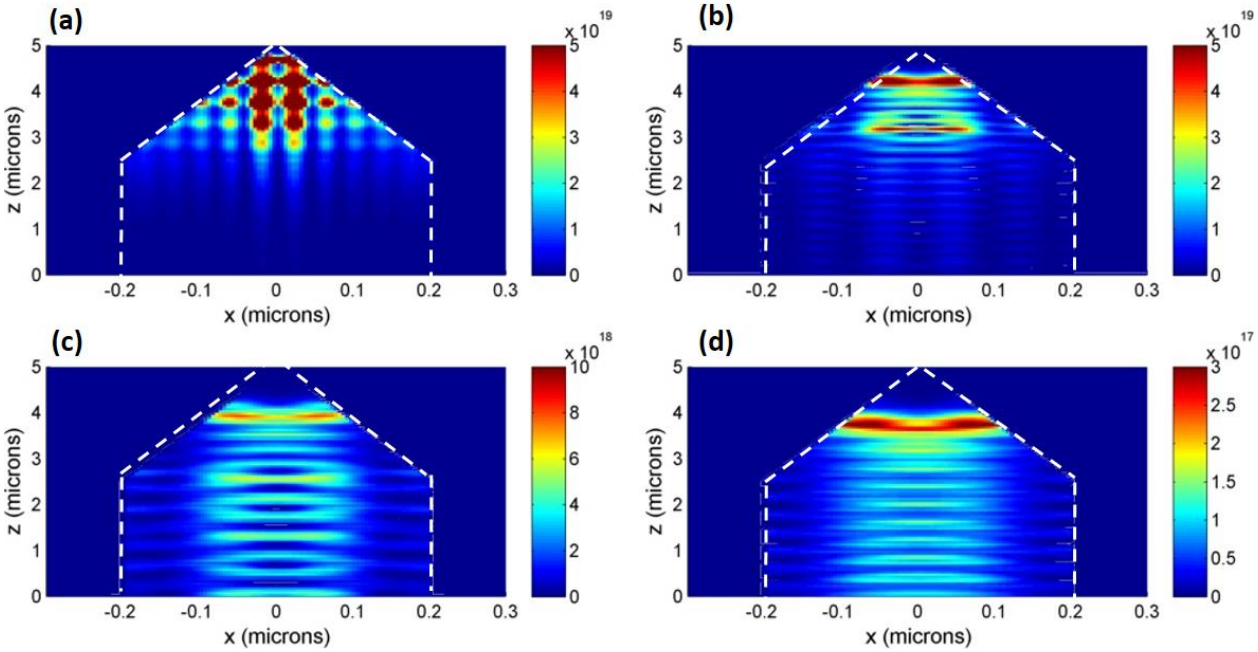

Figure 107: Absorption fields for tapered NWs at (a) 400 nm, (b) 600 nm, (c) 750 nm, and (d) 900 nm. Units of the bar code is W/m^3.

Next, comparisons between bare TNWs and TNWs with P3HT:PCBM (1.9 eV bandgap polymer) and with PDPP3T (1.3 eV bandgap polymer) are made at each wavelength. At 400 nm, no difference could be observed between the bare TNW [Figure 107(a)] and the TNW with both polymers (Figure 108) because this is not the absorption range of any of the polymers. At 600 nm, Figure 109(a) shows that light localized inside the TNW starts to decrease after the addition of P3HT:PCBM while being concentrated mainly in the polymer due the start of increase of the imaginary part of the refractive index of P3HT:PCBM. Thus, the light is not spread along the TNW as in the case of bare TNW. For PDPP3T, light intensity inside the NW did not decrease, however, additional absorption inside the polymer is observed.

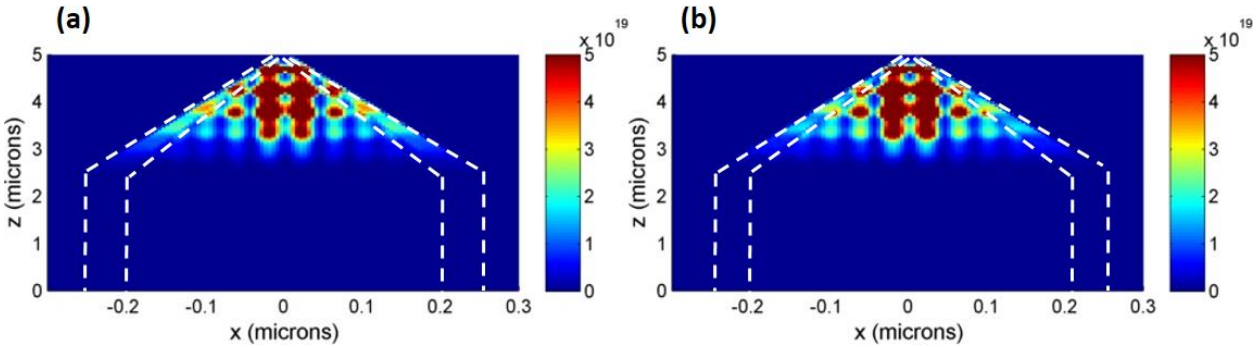

Figure 108: Absorption at 400 nm for TNW coated with (a) P3HT:PCBM and (b) PDPP3T

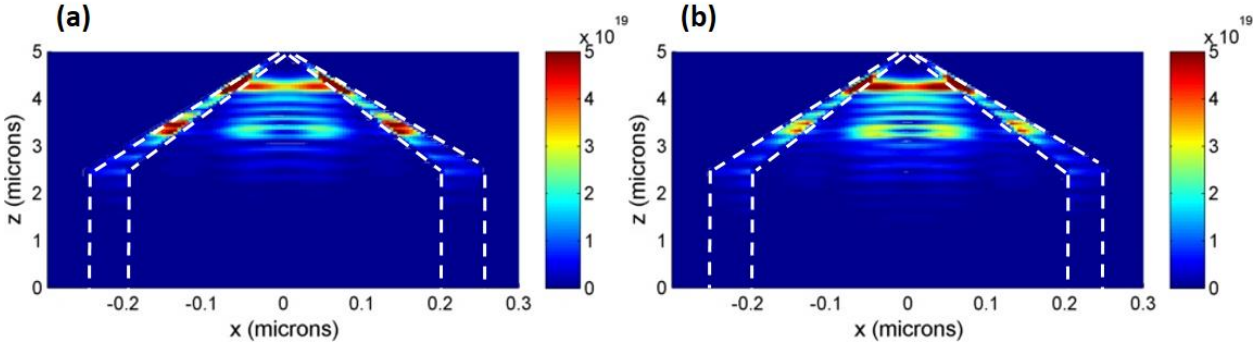

Figure 109: Absorption at 600 nm for TNW coated with (a) P3HT:PCBM and (b) PDPP3T. Units of the bar code is W/m^3.

After the maximum of the imaginary part of the refractive index of P3HT:PCBM (i.e. 750 nm), extremely small part of the light is absorbed inside the P3HT:PCBM polymer. In addition, this wavelength range is longer than that of Silicon. Thus, very low absorption could be observed inside the Silicon as shown in Figure 110. For PDPP3T, light trapping inside the polymer could be seen as shown in Figure 110. Again, after the cut-off of the absorption range of P3HT:PCBM, almost no difference is observed in the absorption between bare TSiNWs and TSiNWs coated with P3HT:PCBM. Since P3HT:PCBM is almost transparent for the light at this wavelength, light penetrated to the SiNW and was homogenously spread along the wire as in the case for bare TNW. However, as mentioned previously, the light intensity at this wavelength is reduced as it is outside the absorption range for both: the SiNW and P3HT:PCBM. On the other hand, for PDPP3T, Figure 111(b), light intensity is still strong as this the range where the imaginary part of the refractive index of PDPP3T is maximum.

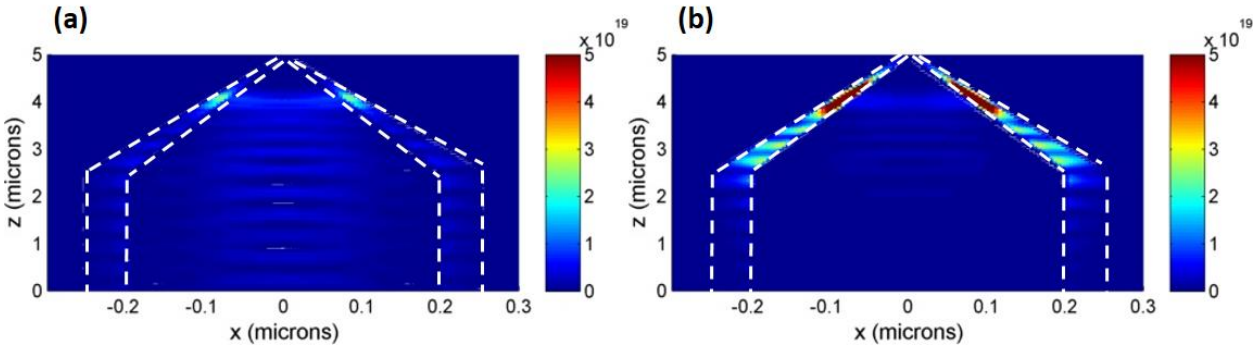

Figure 110: Absorption at 750 nm for TNW coated with (a) P3HT:PCBM and (b) PDPP3T

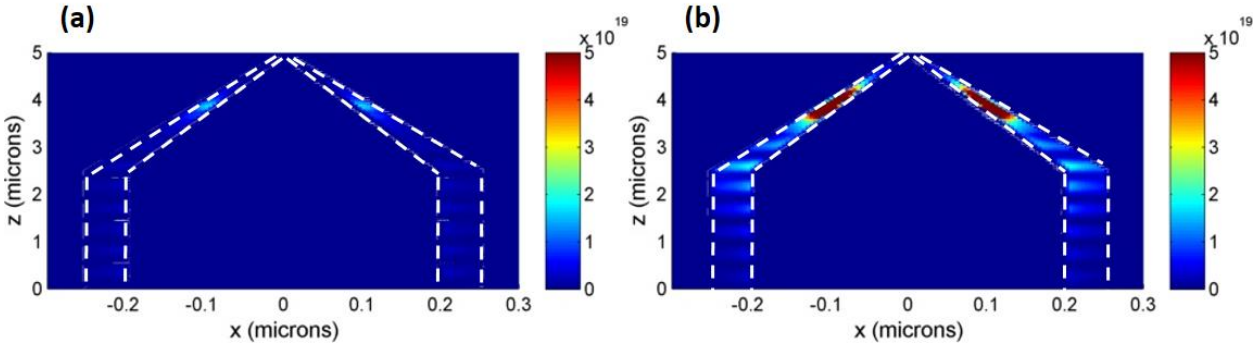

Figure 111: Absorption at 900 nm for TNW coated with (a) P3HT:PCBM and (b) PDPP3T. Units of the bar code is W/m^3.

To summarize all the above observations, the generation rate for each structure is calculated. The generation rate is the integration of the absorption over all simulated wavelengths. The enhancement observed could be seen also in the generation rate of each structure. Figure 112 (a, b, c, and d) shows the different generation rates for the conventional NWs, TNWs, TNWs coated with P3HT:PCBM, and TNWs coated with pBBTDPP2:PCBM, respectively. As expected, most of the generation rate occur at the top the nanowire, especially in the TNWs where the generation rate is much more intense compared the conventional NWs. While adding the P3HT:PCBM reduced the generation rate inside the SiNW, the addition of pBBTDPP2:PCBM did not affect the generation rate inside the NW. However, additional absorption occurred in the polymer boosting the overall absorption and generation rate of the device. The generation rate for TSiNWs coated with PDPP3T is shown in Figure 113. Adding PDPP3T caused the higher generation rate because it has the lowest bandgap. As mentioned previously, the absorption

range of P3HT:PCBM is similar to Silicon, causing the polymer to reduce the absorption inside the Silicon. Adding lower bandgap polymer such as pBBTDPP2:PCBM or PDPP3T did not cause this problem because their absorption ranges are at longer wavelengths compared to Silicon due to their small bandgap.

In addition, The tapering of the NWs will leave more space for the penetration of the polymer between the wires to form the core/shell structure[97,73]. Placing the polymer as a shell on top of the TSiNWs will overcome the problem of short diffusion length of the polymers while achieving high absorption in the polymer due to orthogonalizing the absorption and charge separation directions. Moreover, the conformal polymer coating provides a full coverage of the polymer on the nanowires resulting in large junction area and making the charge separation more efficient.

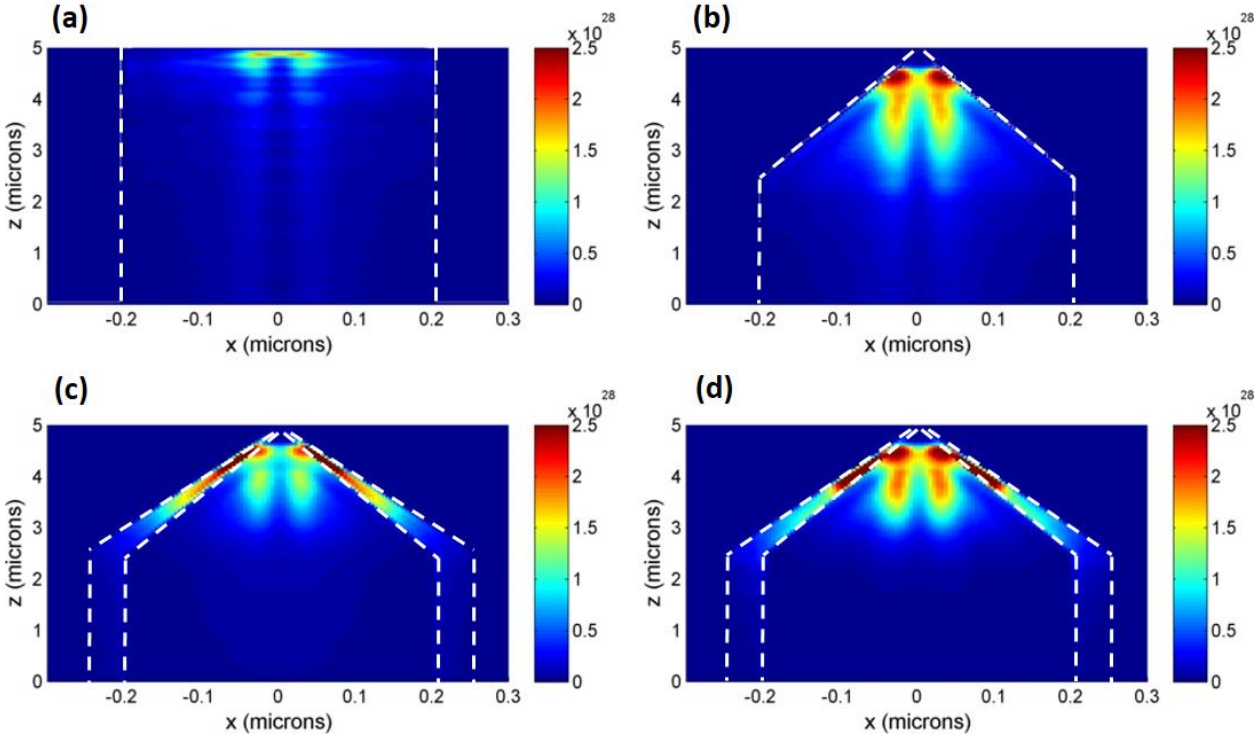

Figure 112: (a), (b), (c), and (d) Generation rate inside conventional nanowires, tapered nanowires, tapered nanowires coated with P3HT:PCBM and tapered nanowires coated with pBBTDPP2:PCBM, respectively. Units of the bar code is number of absorbed photons/m^3 s.

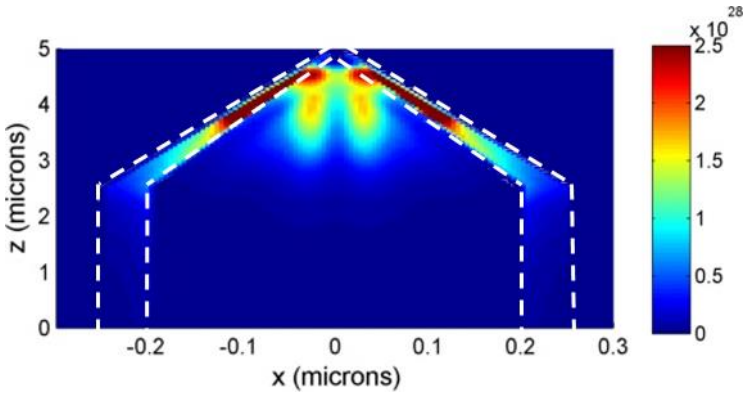

Figure 113: Generation rate inside tapered nanowires coated with PDPP3T. Units of the bar code is number of absorbed photons/m^3 s.

The device was thoroughly optimized to achieve the highest absorption in the visible range. This is done by changing the base diameter of the TNWs from 200 to 400 nm and examine the effect of changing the coated polymer thickness (T) on the overall absorption for each diameter. The thickness (T) is varied between 10 nm and 100 nm and the absorbed power is calculated in each case. The thickness of the polymer coating is measured from the base NW as shown in Figure 114(a). The period is fixed to be 200 nm more than the diameter of the NW for each simulated diameter. Thus, a 100 nm space is left on each side of the NW for the polymer coating. When T= 100nm, the spaces between the wires are fully filled and the full area around the NWs are covered with the polymer as shown in the inset in Figure 114(b).

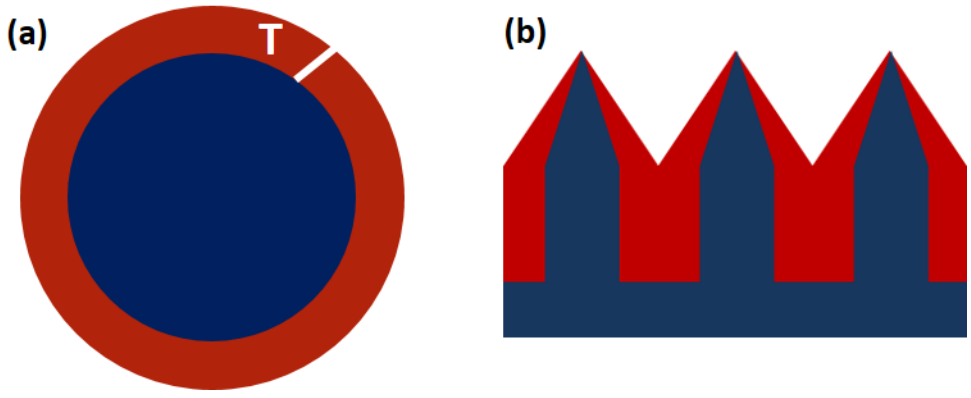

Figure 114: (a) Schematic for the top view of the nanowire showing the thickness (T) of the polymer coating. (b) Schematic of an array of the TNW coated with polymer with maximum thickness where the full area around the nanowires are covered.

It could be seen from Figure 115 that the absorption increases with increasing the polymer thickness (T) for all TNW diameters. A steep increase in AP and J_{sc} is found for smaller polymer

thicknesses (i.e. from 10 nm to 50 nm) then this increase starts to saturates. Even when the polymer fully covers the bottom area of the nanowires as in the case of T=100 nm, the AP and J_{sc} are maximum. Thus, as long as the tapering is preserved, increasing the polymer thickness increases the overall absorption.

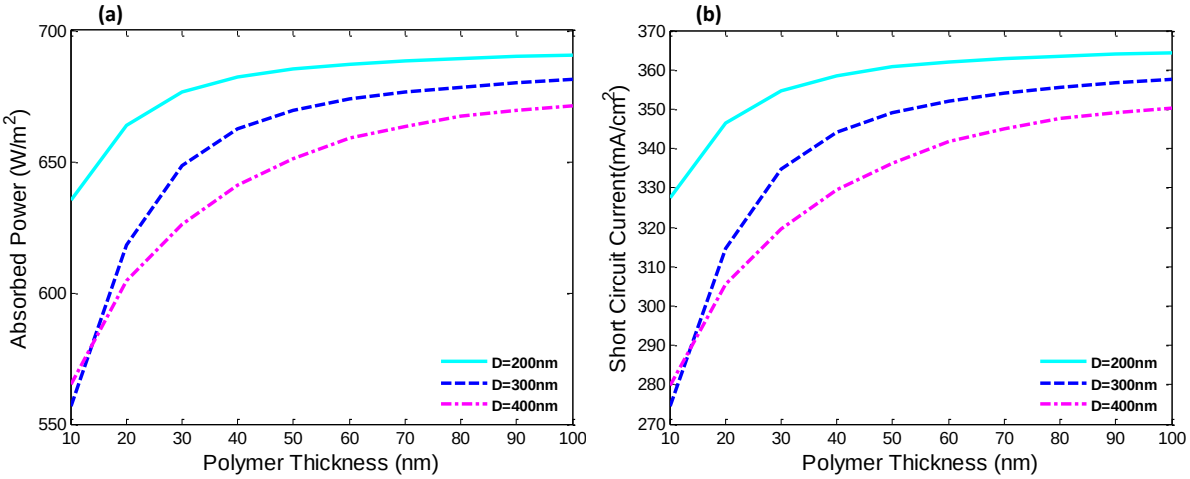

Figure 115: (a) Absorbed power and (b) short circuit current versus polymer coating thickness for several TNW diameters.

The optimized structure was then simulated to calculate its absorption and reflection. Thus, a TNW with D=200 nm is simulated with and without 100 nm thick PDPP3T coating. Figure 116 shows the absorption of the 200 nm TNW with and without polymer coating. The significant increase in absorption and extension of the absorption to the near infra-red after adding PDPP3T is obvious. A unity absorption is achieved up to ~970 nm with only 5 µm long TSiNW coated with 100 nm PDPP3T. 53% enhancement in AP and 76% enhancement in J_{sc} are calculated for the TNW coated with PDPP3T relative to the bare TNW of the same length and diameter. This significant enhancement in absorption is believed to be reflected on the overall power conversion efficiency if the structure boosting the efficiency of NWs based Silicon solar cells. Figure 117 shows the reflection of the bare TNW and TNW coated with PDPP3T. Zero reflection is calculated for the TNW coated with PDPP3T compared to multiple reflections appearing in the bare TNWs.

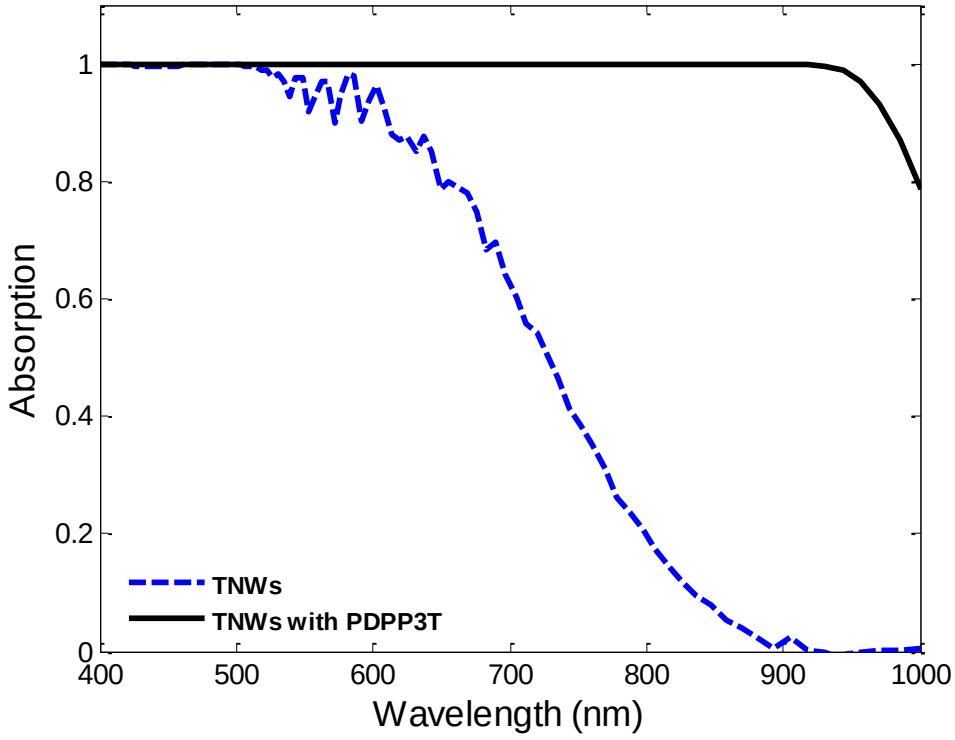

Figure 116: Absorption of the optimized TNW with 100 nm thick PDPP3T coating (black solid line) and of bare 200 nm TNW (blue dashed line)

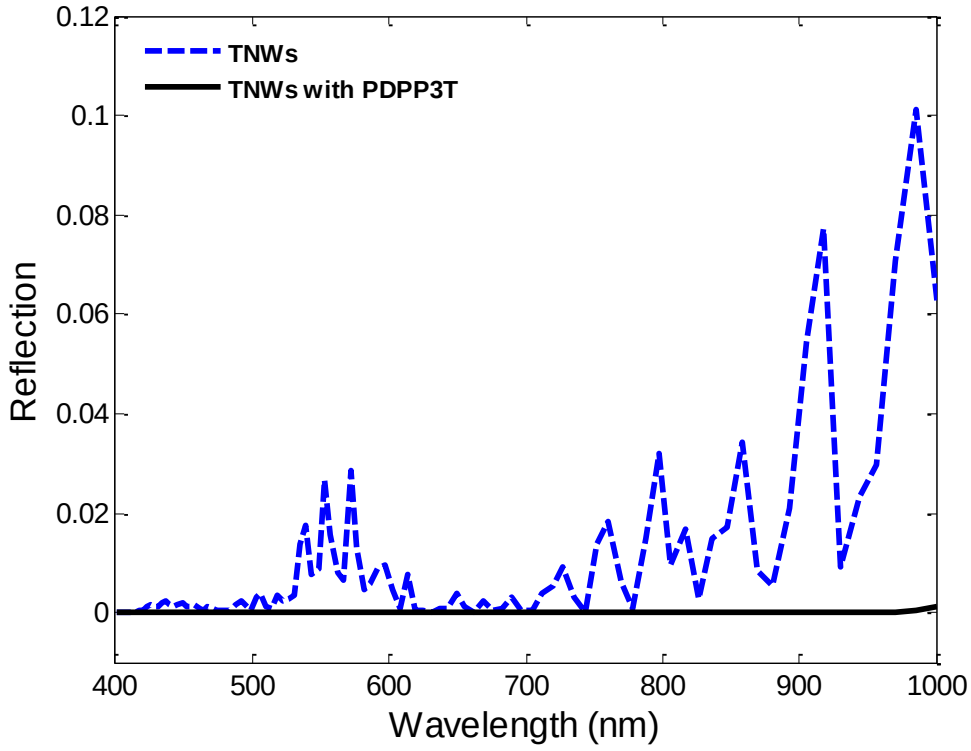

Figure 117: Reflection of the optimized TNW with 100 nm thick PDPP3T coating (black solid line) and of bare 200 nm TNW (blue dashed line)

Finally, the importance of the used TSiNW/polymer configuration should be highlighted. When spin coating the polymer on the TSiNWs, the polymer could fill gaps with different configurations. The air gaps around the TNWs could be filled without coating each NW as shown in Figure 118 (b, c and d). The absorption for these configurations are calculated and shown in Figure 118(a). If the polymer is half filled, slightly lower absorption is calculated compared to the one where the polymer is coating each NW. If more polymer is spin coated filling more of the air gap, the absorption significantly decreases especially in the long wavelength. When the polymer reaches the top of the NW, the absorption further decreases in the whole wavelength range due to covering the tipped part of the TNW. Thus, losing the graded change in Silicon refractive index significantly affect the performance of the proposed structure. In addition, the hot spot in the sharp edge of the TNW is also lost which reduces the light trapping capabilities of the structure. Thus, it could be observed that the optimum configuration is to coat each NW when the polymer to achieve the highest absorption. The reflections for these structures

are also calculated and shown in Figure 119.

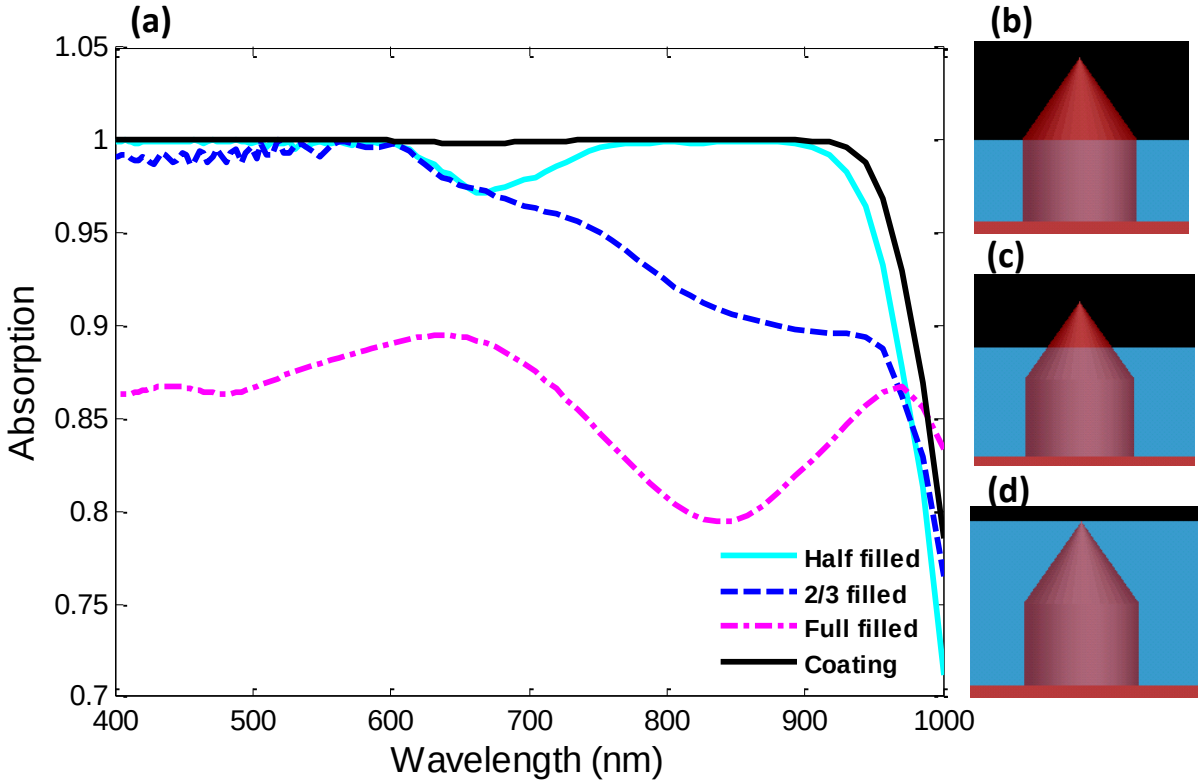

Figure 118: (a) Absorption of the optimized TNW with different polymer configurations. Schematic showing when the polymer is (b) half filled, (c) 2/3 filled, and (d) full filled.

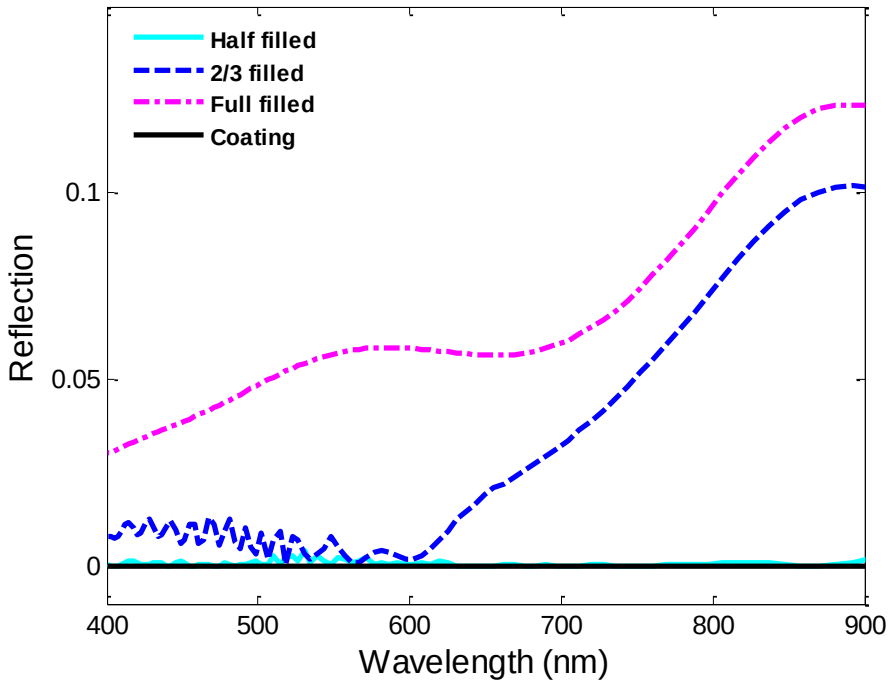

Figure 119: Reflection of the optimized TNW with different polymer configurations

5.3.2. Modal analysis

In this section, a 2D modal analysis for the TNWs with and without polymer coating is analysed in different cross sections along the wire. Here, the diameter of the NW is 250 nm and polymer used for coating is pBBTDPP2:PCBM. The first location used to study the modes is shown in Figure 120 (c). In this location, the wire is not tapered yet and the modes are identical to the ones of a conventional NW. For all wavelengths, the fundamental mode in this location did not change. The field distribution is confined inside the NW and does not penetrate to the surroundings as shown in Figure 120 (a). Even after the polymer is added, Figure 120 (b), the field was still tightly confined inside the NW. This indicates that the coupling of the fundamental mode with the incident light is poor. Thus, this mode does not significantly contribute in the absorption.

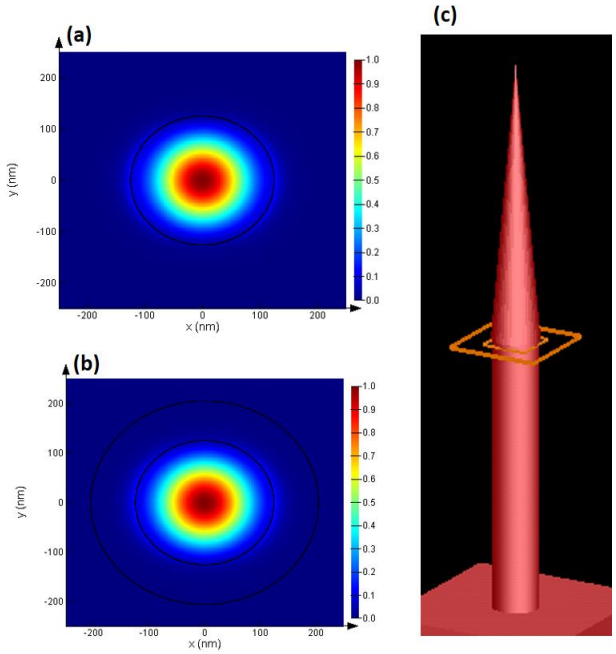

Figure 120: Fundamental mode inside TNW (a) without polymer coating and (b) with polymer coating. (c) The first location were the modes are calculated.

On the other hand, the key mode shown in Figure 121 is concentrated in the NW and in the air between the NWs. Thus, it couples better to the incident light. It could be seen that adding the polymer caused this mode to be confined in both the NW and the polymer. At 600 nm, the light is more confined

in the NW after the adding the polymer in addition to being confined in the polymer as shown in Figure 121 (d). This indicates that this mode contributes strongly to the absorption. Thus, for this location in the NW, only the key mode is studied. The key mode is shown for the same location at 700 and 900 nm in Figure 122.

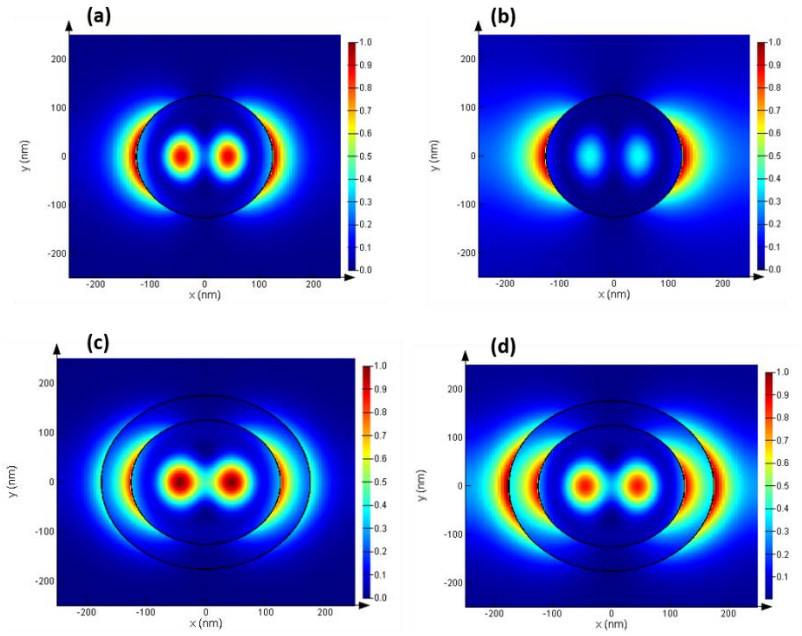

Figure 121: Key mode in the first location along the TNW at (a,c) 570 nm and (b,d) 600 nm with and without polymer coating, respectively.

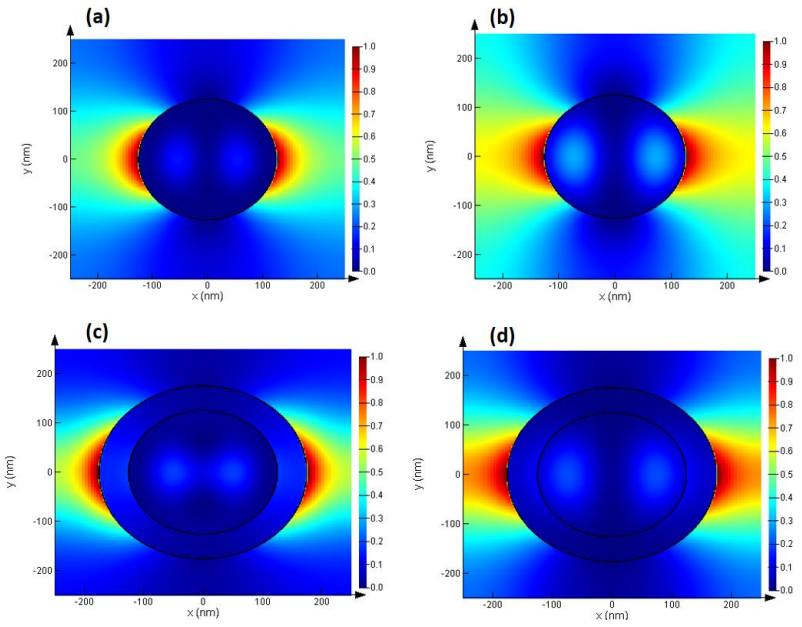

Figure 122: Key mode in the first location along the TNW at (a,c) 700 nm and (b,d) 900 nm with and without polymer coating, respectively.

In the tapered part of the NW, the field distribution starts to change. This is the second location where the modes are analyzed, shown in Figure 123 (e). At 600 nm, the fundamental mode is still confined inside the NW. However, the key mode is mainly concentrated in the area between the NWs. The mode confinement does not change after adding the polymer. These observations are shown in Figure 123. The mode confinements at 700 nm shows a very similar behavior to the ones at 600 nm as shown in Figure 124. At 900 nm, the fundamental mode starts to spread and become more confined in the polymer as shown in Figure 125.

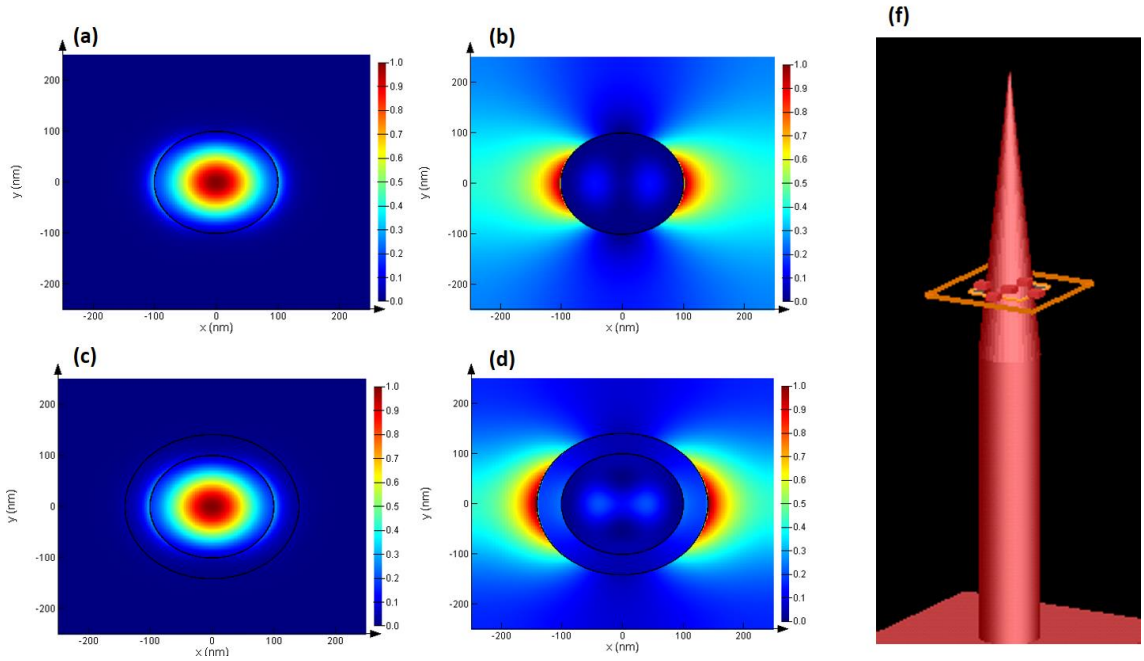

Figure 123: (a,c) The fundamental mode and (b,d) the key mode in the second location along the TNW at 600 nm with and without polymer coating, respectively.(f) The second location were the modes are calculated.

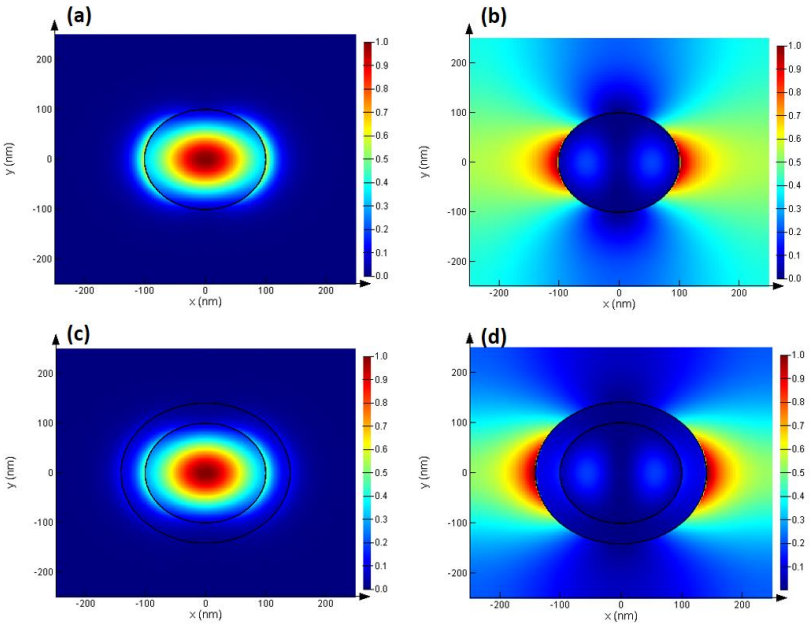

Figure 124: (a,c) The fundamental mode and (b,d) the key mode in the second location along the TNW at 700 nm with and without polymer coating, respectively.

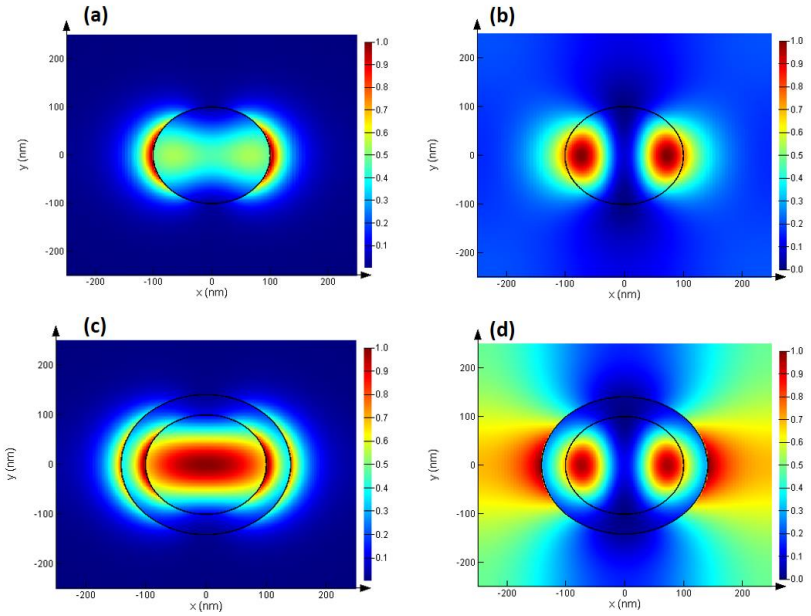

Figure 125: (a,c) The fundamental mode and (b,d) the key mode in the second location along the TNW at 900 nm with and without polymer coating, respectively.

5.4.Conclusion

The structure reported in this chapter provides efficient absorption properties by spanning the whole solar spectrum with the minimum amount of materials which could significantly reduce the

cost of the cell. Using the tapered silicon nanowires structure significantly enhanced the absorption at short wavelengths. The addition of the low band gap polymer pBBTDPP2:PCBM achieved substantial increase in absorption at long wavelengths. Thus, broadband absorption is attained without the need of thick Si substrates. In addition, the TSiNWs fully covered with polymer is believed to have unique electrical properties with efficient charge separation.

Chapter 6 : Conclusions

Thin film solar cells enable the use of low-cost materials with easy fabrication techniques. Thus, the objective of fabricating affordable solar cells that could compete with current conventional energy sources could be reached using this configuration, However, in order to achieve this objective, the efficiency of this type of solar cells should be increased to enable their penetration in the photovoltaic industry. To increase the efficiency of thin film solar cells, their primary challenge should be overcome. Their primary challenge is their low absorption due to their small thickness. Thus, light trapping techniques are essential for these types of solar cells to boost their efficiencies.

In this thesis, several types of thin film solar cells are studied such as organic solar cells and amorphous silicon solar cells. Different light trapping techniques are studied for each type. In addition, the combination between silicon and polymer in a hybrid configuration is studied.

Regarding organic solar cells, chapter 3 showed a thorough analyses of novel type of organic plasmonic solar cells using refractory plasmonics. Absorption enhancement is obtained using TiN and ZrN nanopatterned back electrode in the proposed organic solar cells. In addition, the addition of ZrN nanostructures inside the polymer active layer showed significant absorption enhancement with more than 30% increase in absorption due to the incorporation of ZrN cubical nanoshells in the active layer.

Additionally, a novel technique for fabrication silicon nanocones and nanowires from amorphous silicon is presented in chapter 4. Using excimer laser, a one-step fabrication process of nanocones and nanowires is shown. Analysis and comparisons between the different excimer laser parameters and their effect on the morphology and optical properties of the fabricated nanocones and nanowires are studied, significant increase in absorption is reported for these structures with less than 5% reflection for wide angles. Moreover, a double light trapping structure is numerically proposed in the same structure that confine the light in a thin film amorphous silicon layer by sandwiching it between Au gratings and surface texturing.

Finally, a combination between silicon nanowires and low band gap polymers to form a solar cell device is presented in chapter 5. This structure combines the excellent light trapping capabilities of tapered nanowires with a low band gap polymer to extend the absorption range of the structure. With only 5 microns length of silicon tapered nanowires and 100 nm polymer coating, full absorption of the solar spectrum in the visible and near infra-red range in achieved.

To sum it up, this thesis presents several light trapping techniques of several types of thin film solar cells. The techniques presented here showed significant enhancement in absorption in addition to using low-cost materials with easy fabrication techniques. These presented structures aim to achieve the goal of fabricating highly efficient solar cells that are affordable.

List of Publications

[1] S. Magdi and M. A. Swillam, "Investigating several ZrN plasmonic nanostructures and their effect on the absorption of organic solar cells," *J. Phys. D. Appl. Phys.*, 2017.

[2] S. Magdi, D. Ji, Q. Gan, and M. A. Swillam, "Broadband absorption enhancement in organic solar cells using refractory plasmonic ceramics," *J. Nanophotonics*, vol. 11, no. 1, p. 16001, 2017.

[3] S. Magdi, Q. Gan, and M. A. Swillam, "Analysis of various ZrN plasmonic nanostructures and their effect on the absorption of organic solar cells," in *Frontiers of Optics*, 2016.

[4] S. Magdi and M. A. Swillam, "Broadband absorption enhancement in amorphous Si solar cells using metal gratings and surface texturing Sara," in *Proc. of SPIE*, 2017, vol. 10099.

[5] S. Magdi and M. A. Swillam, "Optical analysis of Si-tapered nanowires/low band gap polymer hybrid solar cells," in *Proc. of SPIE*, 2017, vol. 10099.

[6] S. M. Al Menabawy, Q. Gan, and M. A. Swillam, "Multifunctional TiN nanowires for wide band absorption in organic solar cells," in *Proc. of SPIE*, 2017, vol. 10099.

[7] S. Magdi, Q. Gan, and M. A. Swillam, "Organic solar cells with various plasmonic nanostructures using titanium nitride," in *Proc. of SPIE*, 2016, vol. 9743.

References

(1) Atwater, H. A.; Polman, A. *Nat. Mater.* **2010**, *9* (3), 205–213.

(2) Becquerel, A. *Comptes Rendus* **1839**, *9*, 1839.

(3) Chapin, D.; Fuller, C.; Pearson, G. *J. Appl. Phys.* **1954**, *25*, 676–677.

(4) Green, M. A. *Prog. Photovoltaics Res. Appl.* **2009**, *17*, 183–189.

(5) Eperon, G. E.; Burlakov, V. M.; Docampo, P.; Goriely, A.; Snaith, H. J. *Adv. Funct. Mater.* **2014**, *24*, 151–157.

(6) Kim, H.-S.; Lee, C.-R.; Im, J.-H.; Lee, K.-B.; Moehl, T.; Marchioro, A.; Moon, S.-J.; Humphry-Baker, R.; Yum, J.-H.; Moser, J. E.; Grätzel, M.; Park, N.-G. *Sci. Rep.* **2012**, *2*, 591.

(7) Shirakawa, H.; Louis, E. J.; Macdiarmid, A. G.; Chiang, C. K.; Heeger, A. J. *J. Chem. Soc. Chem. communcations* **1977**, 579.

(8) Green, M. A.; Hishikawa, Y.; Warta, W.; Dunlop, E. D.; Levi, D. H.; Hohl-Ebinger, J.; Ho-Baillie, A. W. H. *Prog. Photovoltaics Res. Appl.* **2017**, *25* (7), 668–676.

(9) Gan, Q.; Bartoli, F. J.; Kafafi, Z. H. *Adv. Mater.* **2013**, *25* (17), 2385–2396.

(10) Kan, B.; Zhang, Q.; Li, M.; Wan, X.; Ni, W.; Long, G.; Wang, Y.; Yang, X.; Feng, H.; Chen, Y. *J. Am. Chem. Soc.* **2014**, *136* (44), 15529–15532.

(11) Liao, S.-H.; Jhuo, H.-J.; Yeh, P.-N.; Cheng, Y.-S.; Li, Y.-L.; Lee, Y.-H.; Sharma, S.; Chen, S.-A. *Sci. Rep.* **2014**, *4*, 6813.

(12) Liu, X.; Chen, H.; Tan, S. *Renew. Sustain. Energy Rev.* **2015**, *52*, 1527–1538.

(13) Liu, Y.; Chen, C.-C.; Hong, Z.; Gao, J.; Yang, Y. M.; Zhou, H.; Dou, L.; Li, G.; Yang, Y. *Sci. Rep.* **2013**, *3*, 3356.

(14) Zhang, Q.; Kan, B.; Liu, F.; Long, G.; Wan, X.; Chen, X.; Zuo, Y.; Ni, W.; Zhang, H.; Li, M.; Hu, Z.; Huang, F.; Cao, Y.; Liang, Z.; Zhang, M.; Russell, T. P.; Chen, Y. *Nat. Photonics* **2014**, *9* (1), 35–41.

(15) Chen, J.-D.; Cui, C.; Li, Y.-Q.; Zhou, L.; Ou, Q.-D.; Li, C.; Li, Y.; Tang, J.-X. *Adv. Mater.* **2015**, *27* (6), 1035–1041.

(16) Aneesh, P. M.; Kumar, C. R.; Reshmi Varma, P. C.; Vivek, K.; Namboothiry, M. a. G. *Org. Photonics Photovoltaics* **2015**, *3* (1), 64–70.

(17) Bai, W. *J. Photonics Energy* **2011**, *1* (1), 11121.

(18) Xie, F.-X.; Choy, W. C. H.; Wang, C. C. D.; Sha, W. E. I.; Fung, D. D. S. *Appl. Phys. Lett.* **2011**, *99* (15), 153304.

(19) Razek, S. A.; Swillam, M. A.; Allam, N. K. *J. Appl. Phys.* **2014**, *115* (19).

(20) Gouda, A. M.; Elsayed, M. Y.; Khalifa, A. E.; Ismail, Y.; Swillam, M. A. *Opt. Lett.* **2016**, *41* (15), 3575.

(21) Abdullah, M. F.; Alghoul, M. A.; Naser, H.; Asim, N.; Ahmadi, S.; Yatim, B.; Sopian, K. *Renew. Sustain. Energy Rev.* **2016**, *66*, 380–398.

(22) Peer, A.; Biswas, R. In *Proc. of SPIE*; 2015; Vol. 9567, p 95670H.

(23) Yang, X.; Chueh, C. C.; Li, C. Z.; Yip, H. L.; Yin, P.; Chen, H.; Chen, W. C.; Jen, A. K. Y. *Adv. Energy Mater.* **2013**, *3* (5), 666–673.

(24) Raja, W.; Bozzola, A.; Zilio, P.; Miele, E.; Panaro, S.; Wang, H.; Toma, A.; Alabastri, A.; De Angelis, F.; Zaccaria, R. P. *Sci. Rep.* **2016**, *6* (24539).

(25) Nagamani, S.; Kumarasamy, G.; Song, M.; Kim, C. S.; Kim, D.-H.; Ryu, S. Y.; Kang, J.-W.; Jin, S.-H. *Synth. Met.* **2016**, *217*, 117–122.

(26) Wang, W.; Wu, S.; Reinhardt, K.; Lu, Y.; Chen, S. *Nano Lett.* **2010**, *10* (6), 2012–2018.

(27) Wu, S. *J. Nanophotonics* **2010**, *4* (1), 43515.

(28) Liu, Z.; Liu, X.; Huang, S.; Pan, P.; Chen, J.; Liu, G.; Gu, G. *ACS Appl. Mater. Interfaces* **2015**, *7* (8), 4962–4968.

(29) Staude, I.; Schilling, J. *Nat. Photonics* **2017**, *11* (5), 274–284.

(30) Chen, H.; Taylor, A. J.; Yu, N.; Liu, G.; Nie, Y.; Fu, G.; Liu, X.; Liu, Y.; Tang, L. *165202*.

(31) Boriskina, S. V; Green, M. A.; Catchpole, K.; Yablonovitch, E.; Beard, M. C.; Okada, Y.; Lany, S.; Gershon, T.; Zakutayev, A.; Tahersima, M. H.; Sorger, V. J.; Naughton, M. J.; Kempa, K.; Dagenais, M.; Yao, Y.; Xu, L.; Sheng, X.; Bronstein, N. D.; Rogers, J. A.; Alivisatos, A. P.; Nuzzo, R. G.; Gordon, J. M.; Wu, D. M.; Wisser, M. D.; Salleo, A.; Dionne, J.; Bermel, P.;

Greffet, J.-J.; Celanovic, I.; Soljacic, M.; Manor, A.; Rotschild, C.; Raman, A.; Zhu, L.; Fan, S.; Chen, G. *J. Opt.* **2016**, *18* (7), 73004.

(32) Gan, Q.; Bartoli, F. J.; Kafafi, Z. H. *Adv. Mater.* **2013**, *25* (17), 2385–2396.

(33) Shen, W.; Tang, J.; Wang, Y.; Liu, J.; Huang, L.; Chen, W.; Yang, L.; Wang, W.; Wang, Y.; Yang, R.; Yun, J.; Belfiore, L. A. *ACS Appl. Mater. Interfaces* **2017**, *9*, 5358–5365.

(34) Stelling, C.; Singh, C. R.; Karg, M.; König, T. A. F.; Thelakkat, M.; Retsch, M. *Sci. Rep.* **2017**, No. February, 1–13.

(35) Kochergin, V.; Neely, L.; Jao, C. Y.; Robinson, H. D. *Appl. Phys. Lett.* **2011**, *98* (13), 133305.

(36) Szeremeta, J.; Nyk, M.; Chyla, A.; Strek, W.; Samoc, M. *Opt. Mater. (Amst).* **2011**, *33* (9), 1372–1376.

(37) Bai, W.; Gan, Q.; Song, G.; Chen, L.; Kafafi, Z.; Bartoli, F. *Opt. Express* **2010**, *18* (November), 620–630.

(38) Ferry, V. E.; Verschuuren, M. A.; Li, H. B. T.; Schropp, R. E. I.; Atwater, H. A.; Polman, A. *Appl. Phys. Lett.* **2009**, *95* (18), 1–4.

(39) Rockstuhl, C.; Fahr, S.; Lederer, F. *J. Appl. Phys.* **2008**, *104* (12).

(40) Munday, J. N.; Atwater, H. A. *Nano Lett.* **2011**, 2195–2201.

(41) Pala, R. A.; White, J.; Barnard, E.; Liu, J.; Brongersma, M. L. *Adv. Mater.* **2009**, *21* (34), 3504–3509.

(42) Spinelli, P.; Ferry, V. E.; van de Groep, J.; van Lare, M.; Verschuuren, M. a; Schropp, R. E. I.; Atwater, H. a; Polman, a. *J. Opt.* **2012**, *14* (2), 24002.

(43) Abdullah, M. F.; Alghoul, M. A.; Naser, H.; Asim, N.; Ahmadi, S.; Yatim, B.; Sopian, K. *Renew. Sustain. Energy Rev.* **2016**, *66*, 380–398.

(44) Battaglia, C.; Hsu, C.; Söderström, K.; Escarré, J.; Haug, F.; Charrière, M.; Boccard, M.; Despeisse, M.; Alexander, D.; Cantoni, M.; Cui, Y.; Ballif, C. *ACS Nano* **2012**, *6* (3), 2790–2797.

(45) Centredoc, E. V.; Hoetzel, J.; Electron, T.; Suisse, B. C.; Empa, J. S.; Laboratories, S. F. In *24th EU PVSEC*; 2009; pp 21–25.

(46) Palanchoke, U.; Jovanov, V.; Kurz, H.; Dewan, R.; Magnus, P.; Stiebig, H.; Knipp, D. *Appl. Phys. Lett.* **2013**, *102* (8).

(47) Jovanov, V.; Palanchoke, U.; Magnus, P.; Stiebig, H.; Hüpkes, J.; Sichanugrist, P.; Konagai, M.; Wiesendanger, S.; Rockstuhl, C.; Knipp, D. *Opt. Express* **2013**, *21* (S4), A595-606.

(48) Muller, J.; Rech, B.; Springer, J.; Vanecek, M. *Sol. Energy* **2004**, *77* (6), 917–930.

(49) Tamang, A.; Hongsingthong, A.; Sichanugrist, P.; Jovanov, V.; Konagai, M.; Knipp, D.; Substrates, S. T.; Tamang, A.; Hongsingthong, A.; Sichanugrist, P.; Jovanov, V. *IEEE J. Photovoltaics* **2014**, *4* (1), 16–21.

(50) Fukuda, M.; Lee, K.-T.; Lee, J. Y.; Guo, L. J. *IEEE J. Photovoltaics* **2014**, *4* (6), 1337–1342.

(51) Sharma, M.; Chaudhary, D.; Sudhakar, N. D. S.; Kumar, S. *Silicon* **2017**, *9*, 59–68.

(52) Iftiquar, S. M.; Jung, J.; Park, H.; Cho, J.; Shin, C.; Park, J.; Jung, J.; Bong, S.; Kim, S.; Yi, J. *Thin Solid Films* **2015**, *587*, 117–125.

(53) Lin, Q.; Leung, S. F.; Lu, L.; Chen, X.; Chen, Z.; Tang, H.; Su, W.; Li, D.; Fan, Z. *ACS Nano* **2014**, *8* (6), 6484–6490.

(54) Iftiquar, S. M.; Jung, J.; Shin, C.; Park, H.; Park, J.; Jung, J.; Yi, J. *Sol. Energy Mater. Sol. Cells* **2015**, *132*, 348–355.

(55) Yang, J. H.; Myong, S. Y.; Lim, K. S. *Sol. Energy Mater. Sol. Cells* **2015**, *132*, 372–386.

(56) Lin, Y.; Xu, Z.; Yu, D.; Lu, L.; Yin, M.; Tavakoli, M. M.; Chen, X.; Hao, Y.; Fan, Z.; Cui, Y.; Li, D. *ACS Appl. Mater. Interfaces* **2016**, *8* (17), 10929–10936.

(57) Yu, D.; Yin, M.; Lu, L.; Zhang, H.; Chen, X.; Zhu, X.; Che, J.; Li, D. *Adv. Mater.* **2015**, *27* (42), 6747–6752.

(58) Li, Y.; Li, M.; Fu, P.; Li, R.; Song, D.; Shen, C.; Zhao, Y. *Sci. Rep.* **2015**, *5* (April), 11532.

(59) Misra, S.; Yu, L.; Foldyna, M.; Roca I Cabarrocas, P. *Sol. Energy Mater. Sol. Cells* **2013**, *118*, 90–95.

(60) Leung, S. F.; Zhang, Q.; Xiu, F.; Yu, D.; Ho, J. C.; Li, D.; Fan, Z. *J. Phys. Chem. Lett.* **2014**, *5* (8), 1479–1495.

(61) Yu, L.; Misra, S.; Wang, J.; Qian, S.; Foldyna, M.; Xu, J.; Shi, Y.; Johnson, E.; Roca I Cabarrocas,

P. *Sci Rep* **2014**, *4*, 1–7.

(62) Yang, Z.; Cao, G.; Shang, A.; Lei, D. Y.; Zhang, C.; Gao, P.; Ye, J. *Nanoscale Res. Lett.* **2016**, *11* (233).

(63) Thiyagu, S.; Pei, Z.; Jhong, M. S. *Nanoscale Res. Lett.* **2012**, *7* (172).

(64) Pei, Z.; Thiyagu, S.; Jhong, M. S.; Hsieh, W. S.; Cheng, S. J.; Ho, M. W.; Chen, Y. H.; Liu, J. C.; Yeh, C. M. *Sol. Energy Mater. Sol. Cells* **2011**, *95* (8), 2431–2436.

(65) Zhu, J.; Yu, Z.; Burkhard, G. F.; Hsu, C.-M.; Connor, S. T.; Xu, Y.; Wang, Q.; McGehee, M.; Fan, S.; Cui, Y. *Nano Lett.* **2009**, *9* (1), 279–282.

(66) Dhindsa, N.; Walia, J.; Saini, S. S. *Nanotechnology* **2016**, *27* (49), 495203.

(67) Dhindsa, N.; Walia, J.; Pathirane, M.; Khodadad, I.; Wong, W. S.; Saini, S. S. *Nanotechnology* **2016**, *27* (14), 145703.

(68) Wright, M.; Uddin, A. *Sol. Energy Mater. Sol. Cells* **2012**, *107*, 87–111.

(69) Liu, R. *Materials (Basel).* **2014**, *7*, 2747–2771.

(70) Zhou, Y.; Eck, M.; Kruger, M. *Energy Environ. Sci.* **2010**, *3*, 1851–1864.

(71) Wang, Y.; Liu, K.; Mukherjee, P.; Hines, D. A.; Santra, P.; Shen, H. Y.; Kamat, P.; Waldeck, D. H. *Phys. Chem. Chem. Phys.* **2014**, *16*, 5066–5070.

(72) Saunders, B. R.; Turner, M. L. *Adv. Colloid Interface Sci.* **2008**, *138*, 1–23.

(73) Jeong, S.; Garnett, E. C.; Wang, S.; Yu, Z.; Fan, S.; Brongersma, M. L.; Mcgehee, M. D.; Cui, Y. *Nano Lett.* **2012**.

(74) Peters, C. H.; Guichard, A. R.; Hryciw, A. C.; Brongersma, M. L.; McGehee, M. D. In *Journal of Applied Physics*; 2009; Vol. 105, pp 1–6.

(75) Gowrishankar, V.; Scully, S. R.; Chan, A. T.; McGehee, M. D.; Wang, Q.; Branz, H. M. *J. Appl. Phys.* **2008**, *103* (6), 1–8.

(76) Gowrishankar, V.; Scully, S. R.; Mcgehee, M. D.; Wang, Q.; Branz, H. M. *Appl. Phys. Lett.* **2006**, *89*, 252102.

(77) Abrusci, A.; Ding, I.; Al-hashimi, M.; Segal-peretz, T.; Mcgehee, M. D.; Heeney, M.; Frey, L.; Snaith, H. J. *Energy Environ. Sci.* **2011**, *4*, 3051–3058.

(78) Davenas, J.; Boiteux, G.; Cornu, D.; Rybak, A. *Synth. Met.* **2012**, *161*, 2623–2627.

(79) Nemes, C. T.; Vijapurapu, D. K.; Petoukhoff, C. E.; Cheung, G. Z.; O'Carroll, D. M. *J. Nanoparticle Res.* **2013**, *15* (8), 1801.

(80) Jeong, H.; Song, H.; Pak, Y.; Kwon, I. K.; Jo, K.; Lee, H.; Jung, G. Y. *Adv. Mater.* **2014**, *26*, 3445–3450.

(81) Kuo, C. Y.; Gau, C. *Appl. Phys. Lett.* **2009**, *95* (5), 1–4.

(82) Yu, P.; Tsai, C. Y.; Chang, J. K.; Lai, C. C.; Chen, P. H.; Lai, Y. C.; Tsai, P. T.; Li, M. C.; Pan, H. Te; Huang, Y. Y.; Wu, C. I.; Chueh, Y. L.; Chen, S. W.; Du, C. H.; Horng, S. F.; Meng, H. F. *ACS Nano* **2013**, *7* (12), 10780–10787.

(83) Liu, Z.; Xu, L.; Zhang, W.; Ge, Z.; Xu, J.; Su, W.; Yu, Y.; Ma, Z.; Chen, K. *Appl. Surf. Sci.* **2015**, *334*, 110–114.

(84) Liu, K.; Bi, Y.; Qu, S.; Tan, F.; Chi, D.; Lu, S.; Li, Y.; Kou, Y.; Wang, Z. *Nanoscale* **2014**, *6*, 6180–6186.

(85) Liu, K.; Qu, S.; Zhang, X.; Tan, F.; Wang, Z. *Nanoscale Res. Lett.* **2013**, *8* (88).

(86) Sharma, M.; Pudasaini, P. R.; Ruiz-zepeda, F.; Elam, D.; Ayon, A. A. *ACS Appl. Mater. Interfaces* **2014**, *6*, 4356–4363.

(87) Ren, S.; Chang, L.; Lim, S.; Zhao, J.; Smith, M.; Zhao, N. *Nano Lett.* **2011**, *11*, 3998–4002.

(88) Xu, Q.; Song, T.; Cui, W.; Liu, Y.; Xu, W.; Lee, S.; Sun, B. *ACS Appl. Mater. Interfaces* **2015**, *7*, 3272–3279.

(89) Thiyagu, S.; Hsueh, C.; Liu, C.; Syu, H.; Lin, T.; Lin, C. *Nanoscale* **2014**, *6*, 3361–3366.

(90) Chen, J.; Con, C.; Yu, M.; Cui, B.; Sun, K. W. *ACS Appl. Mater. Interfaces* **2013**, *5*, 7552–7558.

(91) Chi, D.; Qi, B.; Wang, J.; Qu, S.; Wang, Z. *Appl. Phys. Lett.* **2014**, *193903*, 1–5.

(92) Kim, J.; Hong, Z.; Li, G.; Song, T.; Chey, J.; Lee, Y. S.; You, J.; Chen, C.; Sadana, D. K.; Yang, Y. *Nat. Commun.* **2015**, *6* (6391).

(93) Syu, H.-J.; Shiu, S.; Hung, Y.; Hsueh, C.; Lin, T.; Thiyagu, S.; Lee, S.; Lin, C. *Prog. Photovoltaics Res. Appl.* **2013**, *21*, 1400–1410.

(94) Ussein, M. O. H.; Ameed, M. O. F. A. O. H.; Reed, N. I. F. F. A.; Ahia, A. S. Y.; Bayya, S. S. A.

O. *Opt. Express* **2016**, *41* (5), 1010–1013.

(95) Jiang, Y.; Gong, X.; Qin, R.; Liu, H.; Xia, C.; Ma, H. *Nanoscale Res. Lett.* **2016**, *11* (1), 267.

(96) Jiang, Y.; Qin, R.; Li, M.; Wang, G. *Mater. Sci. Semicond. Process.* **2014**, *17*, 81–86.

(97) Gong, X.; Jiang, Y.; Li, M.; Liu, H.; Ma, H. *RSC Adv.* **2015**, *5* (14), 10310–10317.

(98) Dawood, M. K.; Liew, T. H.; Lianto, P.; Hong, M. H.; Tripathy, S.; Thong, J. T. L.; Choi, W. K. *Nanotechnology* **2010**, *21*, 205305.

(99) Guler, U.; Shalaev, V. M.; Boltasseva, A. *Mater. Today* **2014**, *18* (4), 227–237.

(100) Catchpole, K. R.; Polman, A. *Opt. Express* **2008**, *16* (26), 21793–21800.

(101) Gan, Q.; Bartoli, F. J.; Kafafi, Z. H. *IEEE Photonics J.* **2012**, *4* (2), 620–624.

(102) Aneesh, P. M.; Kumar, C. R.; Varma, P. C. R.; Vivek, K.; Namboothiry, M. A. G. *Org. Photonics Photovoltaics* **2015**, *3*, 64–70.

(103) Liao, S.-H.; Jhuo, H.-J.; Cheng, Y.-S.; Chen, S.-A. *Adv. Mater.* **2013**, *25* (34), 4766–4771.

(104) Xie, F.-X.; Choy, W. C. H.; Wang, C. C. D.; Sha, W. E. I.; Fung, D. D. S. *Appl. Phys. Lett.* **2011**, *99* (2011), 153304.

(105) Zeng, B.; Gan, Q.; Kafafi, Z. H.; Bartoli, F. J. *J. Appl. Phys.* **2013**, *113* (6), 63109.

(106) Bai, W.; Gan, Q.; Song, G.; Chen, L.; Kafafi, Z.; Bartoli, F. *Opt. Express* **2010**, *18* (S4), 720–721.

(107) Rumbak, M.; Visoly-Fisher, I.; Shikler, R. *J. Appl. Phys.* **2013**, *114* (1), 13102.

(108) Guler, U.; Kildishev, A.; Boltasseva, A.; Shalaev, V. *Farady Discuss.* **2015**, *178*, 71–86.

(109) Naik, G. V.; Shalaev, V. M.; Boltasseva, A. *Adv. Mater.* **2013**, *25* (24), 3264–3294.

(110) Naik, G. V.; Schroeder, J. L.; Ni, X.; Kildishev, A. V.; Sands, T. D.; Boltasseva, A. *Opt. Mater. Express* **2012**, *2* (4), 478–489.

(111) Guler, U.; Suslov, S.; Kildishev, A. V.; Boltasseva, A.; Shalaev, V. M. *Nanophotonics* **2015**, *4* (1).

(112) Khalifa, A. E.; Swillam, M. A. *J. Nanophotonics* **2014**, *8* (1), 84098.

(113) Kim, S.; Lee, J.-L. *J. Photonics Energy* **2012**, *2* (1), 21215.

(114) Ji, Y.; Ran, F.; Xu, H.; Shen, W.; Zhang, J. *Org. Electron.* **2014**, *15* (11), 3137–3143.

(115) Iwase, M.; Suzuki, A.; Akiyama, T.; Oku, T. *Mater. Sci. Appl.* **2014**, *5*, 278–284.

(116) Mihailetchi, V. D.; Koster, L. J. A.; Blom, P. W. M. *Appl. Phys. Lett.* **2004**, *85* (6), 970–972.

(117) Yokota, K.; Nakamura, K.; Kasuya, T.; Mukai, K.; Ohnishi, M. *J. Phys. D. Appl. Phys.* **2004**, *37* (7), 1095–1101.

(118) Norouzian, S.; Larijani, M. M.; Afzalzadeh, R. *Bull. Mater. Sci.* **2012**, *35* (5), 885–887.

(119) Guo, X.; Liu, X.; Lin, F.; Li, H.; Fan, Y.; Zhang, N. *Sci. Rep.* **2015**, *5* (April), 10569.

(120) Kim, Y. H.; Sachse, C.; MacHala, M. L.; May, C.; Müller-Meskamp, L.; Leo, K. *Adv. Funct. Mater.* **2011**, *21* (6), 1076–1081.

(121) Dennler, G.; Forberich, K.; Ameri, T.; Waldauf, C.; Denk, P.; Brabec, C. J.; Hingerl, K.; Heeger, A. J. *J. Appl. Phys.* **2007**, *102* (12), 1–7.

(122) Hoppe, H.; Sariciftci, N. S.; Meissner, D. *Sol. Cells* **2002**, *385*, 233–240.

(123) Min, J.; Zhang, H.; Stubhan, T.; Luponosov, Y. N.; Kraft, M.; Ponomarenko, S. A.; Ameri, T.; Scherf, U.; Brabec, C. J. *J. Mater. Chem. A* **2013**, *1* (37), 11306.

(124) Kong, J.; Lee, J.; Kim, G.; Kang, H.; Choi, Y.; Lee, K. *Phys. Chem. Chem. Phys.* **2012**, *14* (30), 10547.

(125) Guler, U.; Naik, G. V.; Boltasseva, A.; Shalaev, V. M.; Kildishev, A. V. *Appl. Phys. B* **2012**, *107* (2), 285–291.

(126) Kumar, M.; Umezawa, N.; Ishii, S.; Nagao, T. *ACS Photonics* **2016**, *3*, 43–50.

(127) Jiang, P.; McFarland, M. J. *J. Am. Chem. Soc.* **2005**, *127* (11), 3710–3711.

(128) Li, E.-P.; Chu, H.-S. 2014; p 182.

(129) Moon, P.; Dubin, V.; Johnston, S.; Leu, J.; Raol, K.; Wu, C. *IEEE Int. Electron Devices Meet. 2003* **2003**, No. C, 841–844.

(130) Chau, R.; Datta, S.; Doczy, M.; Doyle, B.; Kavalieros, J.; Metz, M. *IEEE Electron Device Lett.* **2004**, *25* (6), 408–410.

(131) Dutta, A.; Kinsey, N.; Saha, S.; Guler, U.; Shalaev, V. M.; Boltasseva, A. In *Conference on Lasers and Electro-Optics*; 2016.

(132) Gui, L.; Bagheri, S.; Strohfeldt, N.; Hentschel, M.; Zgrabik, C. M.; Metzger, B.; Linnenbank,

H.; Hu, E. L.; Giessen, H. *Nano Lett.* **2016**, *16* (9), 5708–5713.

(133) Magdi, S.; Gan, Q.; Swillam, M. A. In *Proc. of SPIE*; 2016; Vol. 9743, p 97431H1.

(134) Magdi, S.; Ji, D.; Gan, Q.; Swillam, M. A. *J. Nanophotonics* **2017**, *11* (1), 16001.

(135) Zhang, W.; Saliba, M.; Stranks, S. D.; Sun, Y.; Shi, X.; Wiesner, U.; Snaith, H. J. *Nano Lett.* **2013**, 130815103150002.

(136) Brown, M. D.; Suteewong, T.; Kumar, R. S. S.; D'Innocenzo, V.; Petrozza, A.; Lee, M. M.; Wiesner, U.; Snaith, H. J. *Nano Lett.* **2011**, *11* (2), 438–445.

(137) Cheng, P. H.; Zhao, H. X.; Bao, J. L.; Wu, L. G.; Li, D. S.; Yang, D. R. *J. Opt. Soc. Am. B-Optical Phys.* **2013**, *30* (2), 405–409.

(138) Cheng, P.; Wu, L.; Li, X.; Li, T.; Zhao, H.; Bao, J. *Opt. Commun.* **2015**, *335*, 279–283.

(139) Guilatt, O.; Apter, B.; Efron, U. *Opt. Lett.* **2011**, *36* (7), 1239.

(140) Al Menabawy, S. M.; Gan, Q.; Swillam, M. A. In *Proc. of SPIE*; 2017; Vol. 10099, p 1009918.

(141) Thimmappa, R.; Paswan, B.; Gaikwad, P.; Devendrachari, M. C.; Makri Nimbegondi Kotresh, H.; Rani Mohan, R.; Pattayil Alias, J.; Thotiyl, M. O. *J. Phys. Chem. C* **2015**, *119* (25), 14010–14016.

(142) Hooshmand, N.; O'Neil, D.; Asiri, A. M.; El-Sayed, M. *J. Phys. Chem. A* **2014**, *118* (37), 8338–8344.

(143) Hooshmand, N.; Bordley, J. A.; El-Sayed, M. A. *J. Phys. Chem. C* **2015**, 150629150159005.

(144) Bordley, J. A.; Hooshmand, N.; El-Sayed, M. A. *Nano Lett.* **2015**, *15* (5), 3391–3397.

(145) Yang, X.; Li, C.; Yang, L.; Yan, Y.; Qian, Y. *J. Am. Ceram. Soc.* **2003**, *86* (1), 206–208.

(146) Li, J.; Gao, L.; Sun, J.; Zhang, Q.; Guo, J.; Yan, D. *J. Am. Ceram. Soc.* **2001**, *84* (12), 3045–3047.

(147) Reinholdt, A.; Pecenka, R.; Pinchuk, A.; Runte, S.; Stepanov, A. L.; Weirich, T. E.; Kreibig, U. *Eur. Phys. J. D* **2004**, *31* (1), 69–76.

(148) Stöber, W.; Fink, A.; Bohn, E. *J. Colloid Interface Sci.* **1968**, *26* (1), 62–69.

(149) Higgins, D. C.; Choi, J.-Y.; Wu, J.; Lopez, A.; Chen, Z. *J. Mater. Chem.* **2012**, *22* (9), 3727.

(150) Guler, U.; Ndukaife, J. C.; Naik, G. V.; Nnanna, A. G. A.; Kildishev, A.; Shalaev, V. M.;

Boltasseva, A. *Cleo 2013* **2013**, QTu1A.2.

(151) Chowdhury, A.; Kang, D.-W.; Sichanugrist, P.; Konagai, M. *Thin Solid Films* **2016**, *616*, 461–465.

(152) Zhang, Y.; Gu, M. *Front. Optoelectron.* **2016**, *9* (2), 277–282.

(153) Winans, J. D.; Hungerford, C.; Shome, K.; Rothberg, L. J.; Fauchet, P. M. *Opt. Express* **2015**, *23* (3), A92.

(154) Huang, H.; Lu, L.; Wang, J.; Yang, J.; Leung, S.-F.; Wang, Y.; Chen, D.; Chen, X.; Shen, G.; Li, D.; Fan, Z. *Energy Environ. Sci.* **2013**, *6* (10), 2965.

(155) Liu, L.; Barber, G. D.; Shuba, M. V.; Yuwen, Y.; Lakhtakia, A.; Mallouk, T. E.; Mayer, T. S. *ACS Photonics* **2016**, *3* (4), 604–610.

(156) Yu, P.; Wu, J.; Liu, S.; Xiong, J.; Jagadish, C.; Wang, Z. M. *Nano Today* **2016**, *11* (6), 704–737.

(157) Sandhu, S.; Fan, S. *ACS Photonics* **2015**, *2* (12), 1698–1704.

(158) Van Dam, D.; Van Hoof, N. J. J.; Cui, Y.; Van Veldhoven, P. J.; Bakkers, E. P. A. M.; G??mez Rivas, J.; Haverkort, J. E. M. *ACS Nano* **2016**, *10* (12), 11414–11419.

(159) Garnett, E.; Yang, P. *Nano Lett.* **2010**, *10* (3), 1082–1087.

(160) Sturmberg, B. C. P.; Dossou, K. B.; Botten, L. C.; Asatryan, A. A.; Poulton, C. G.; de Sterke, C. M.; McPhedran, R. C. *Opt. Express* **2011**, *19* (S5), A1067.

(161) Ko, M.-D.; Rim, T.; Kim, K.; Meyyappan, M.; Baek, C.-K. *Sci. Rep.* **2015**, *5*, 11646.

(162) Razek, S. A.; Swillam, M. A.; Allam, N. K. *J. Appl. Phys.* **2014**, *115* (19).

(163) Tchakarov, S.; Das, D.; Saadane, O.; Kharchenko, A. V.; Suendo, V.; Kail, F.; Roca i Cabarrocas, P. *J. Non. Cryst. Solids* **2004**, *338–340* (1 SPEC. ISS.), 668–672.

(164) Roszairi, H.; Rahman, S. a. *ICONIP '02. Proc. 9th Int. Conf. Neural Inf. Process. Comput. Intell. E-Age (IEEE Cat. No.02EX575)* **2002**, 300–303.

(165) Kumar, P.; Krishna, M. G.; Bhattacharya, A. *J. Nanosci. Nanotechnol.* **2009**, *9* (5), 3224–3232.

(166) Kumar, P. *Appl. Phys. A Mater. Sci. Process.* **2010**, *99* (1), 245–250.

(167) Porte, H. P.; Turchinovich, D.; Persheyev, S.; Fan, Y.; Rose, M. J.; Jepsen, P. U. *IEEE Trans. Terahertz Sci. Technol.* **2013**, *3* (3), 331–341.

(168) Hong, L.; Wang, X. C.; Zheng, H. Y.; He, L.; Wang, H.; Yu, H. Y. *J. Phys. D. Appl. Phys.* **2013**, *46* (19), 195109.

(169) Magdi, S.; Swillam, M. A. In *Proc. of SPIE*; 2017; Vol. 10099, p 1009912.

(170) Magdi, S.; Swillam, M. A. In *Proc. of SPIE*; 2017; Vol. 10099, p 100991D.

(171) Zhou, S.; Yang, Z.; Gao, P.; Li, X.; Yang, X.; Wang, D.; He, J.; Ying, Z.; Ye, J. *Nanoscale Res. Lett.* **2016**, *11* (1), 194.

(172) Wang, W.; Li, X.; Wen, L.; Liu, G.; Shi, T.; Duan, H.; Zhou, B.; Li, N.; Zhao, Y.; Zeng, X.; Wang, Y. *Appl. Phys. Lett.* **2014**, *105* (23), 1–6.

(173) Chutinan, A.; Kherani, N. P.; Zukotynski, S. *Opt. Express* **2009**, *17* (11), 8871.